

**Rafael Martinho Vieira**

**Exploring magnetocaloric materials by ab-initio methods**





## Rafael Vieira

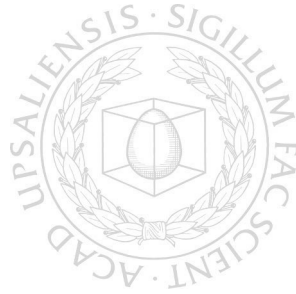
Born 1992, in Faro, Portugal

### Previous studies and degrees

Licenciate, Uppsala University, 2020

Master, University of Lisbon, 2017

Bachelor, University of Lisbon, 2015



# Exploring magnetocaloric materials by ab-initio methods

Rafael Martinho Vieira

Physics  
Faculty of Science and Engineering  
Åbo Akademi University  
Åbo, Finland, 2024

Materials Theory  
Department of Physics and Astronomy  
Uppsala University  
Uppsala, Sweden, 2024

Dissertation presented at Uppsala University to be publicly examined in Högssalen, Lägerhyddsvägen 1, 752 37 Uppsala, Uppsala, Friday, 26 April 2024 at 09:00 for the degree of Doctor of Philosophy. The examination will be conducted in English. Faculty examiner: Markus Gruner (Universität Duisburg-Essen).

### Abstract

Martinho Vieira, R. 2024. Exploring magnetocaloric materials by ab-initio methods. *Digital Comprehensive Summaries of Uppsala Dissertations from the Faculty of Science and Technology* 2384. Åbo, Finland: Åbo Akademi University. ISBN 978-952-12-4376-9. ISBN 978-952-12-4377-6.

This thesis explores the characterization of magnetocaloric materials from first-principles calculations, emphasizing entropy variation associated with the magnetocaloric effect. The study happens in the context of the search for new magnetocaloric materials to be applied in domestic magnetic refrigerators, as environmentally friendly and energy-efficient alternatives to conventional vapor-compression devices.

The study involves benchmarking entropy calculations in systems like FeRh, which exhibits a first-order metamagnetic transition, and Gd, with a second-order ferromagnetic-paramagnetic transition. Different levels of approximations are examined and compared against experimental data, highlighting the need to distinguish between first-order and second-order transitions in the approach taken. The tests underscore the necessity of calculating vibrational and elastic properties for both phases to accurately calculate the entropy variation. This insight is applied in the study of  $\text{Mn}_{0.5}\text{Fe}_{0.5}\text{NiSi}_{0.9}\text{Al}_{0.05}$ , with results consistent with experimental data.

Furthermore, the relationship between structural changes and magnetic properties is investigated, in particular for pressure-induced polymorphs in Gd and the phase transition in  $\text{Mn}_{0.5}\text{Fe}_{0.5}\text{NiSi}_{0.95}\text{Al}_{0.05}$ . In the case of Gd, it was shown that variations in magnetic ordering temperature under pressure could be explained through a model based on the formation and accumulation of stacking faults. For the  $\text{Mn}_{0.5}\text{Fe}_{0.5}\text{NiSi}_{0.95}\text{Al}_{0.05}$  system, the adoption of a magnetic composite model, in conjunction with experimental data, allowed to determine that the magnetostructural transition in these compounds is predominantly driven by the lattice subsystem.

The results positively confirm the feasibility of using first-principles entropy estimates as an effective screening tool in high-throughput studies for magnetocaloric materials. A promising workflow is proposed, demonstrating potential in its initial results. Through comparison with experimental data, the derived routes offer valuable insights for the further refinement of the workflow. This approach aims to enhance accuracy and systematically manage complex systems, highlighting a path forward for future advancements.

Lastly, the introduction of a novel scaling scheme in Monte Carlo simulations enhancing accuracy across various temperatures, represents a potential advancement in the field of magnetic simulations.

*Keywords:* magnetocaloric, magnetism, ab-initio

*Rafael Martinho Vieira, Department of Physics and Astronomy, Materials Theory, Box 516, Uppsala University, SE-751 20 Uppsala, Sweden.*

© Rafael Martinho Vieira 2024

ISSN 1651-6214

ISBN 978-952-12-4376-9 ISBN 978-952-12-4377-6

URN urn:nbn:se:uu:diva-525219 (<http://urn.kb.se/resolve?urn=urn:nbn:se:uu:diva-525219>)

## Supervisors

Dr. Heike C. Herper	Dr. Torbjörn Björkman	Professor Olle Eriksson
Uppsala University	Åbo Akademi University	Uppsala University
Uppsala, Sweden	Åbo, Finland	Uppsala, Sweden

## Pre-examiners

Dr. Corina Etz	Professor Kalevi Kokko
Luleå University of Technology	University of Turku
Luleå, Sweden	Åbo, Finland

## Opponent

Dr. Markus Gruner  
University of Duisburg-Essen  
Duisburg, Germany

ISBN 978-952-12-4376-9 (printed)  
ISBN 978-952-12-4377-6 (digital)  
Painosalama, Åbo, Finland 2024

*To all who marvel at the intricate wonders of ferromagnetic phenomena  
and adventure in its exploration with enthusiasm and curiosity.*

# List of included publications

This thesis is based on the following papers, which are referred to in the text by their Roman numerals.

- I **High-throughput compatible approach for entropy estimation in magnetocaloric materials: FeRh as a test case**  
Rafael Martinho Vieira, Olle Eriksson, Anders Bergman, Heike C. Herper  
*J. Alloys Compd.* 857, 157811 (2021)
- II **Realistic first-principles calculations of the magnetocaloric effect: applications to hcp Gd**  
Rafael Martinho Vieira, Olle Eriksson, Torbjörn Björkman, Anders Bergman, Heike C. Herper  
*Mater. Res. Lett.* 10, 156–162 (2022)
- III **Giant magnetocaloric effect in the (Mn,Fe)NiSi-system**  
Sagar Ghorai, Rafael Martinho Vieira, Vitalii Shtender, Erna K. Delczeg-Czirjak, Heike C. Herper, Torbjörn Björkman, Sergei I. Simak, Olle Eriksson, Martin Sahlberg, and Peter Svedlindh  
*arXiv.2307.00128 (2023)*, Submitted to *Acta Materialia*
- IV **The role of pressure-induced stacking faults on the magnetic properties of gadolinium**  
Rafael Martinho Vieira, Olle Eriksson, Torbjörn Björkman, Ondřej Šipr, Heike C. Herper  
*arXiv.2309.01285 (2023)*, Submitted to *Phys. Rev. B*

Reprints were made with permission from the publishers.

# Author's contribution to publications

- I. The author planned the work together with the co-authors, performed the numerical simulations and respective analysis of the results and wrote the draft of the manuscript. The author finalized the paper together with the co-authors.
- II. The author planned the work together with the co-authors, wrote the code for the proposed Monte Carlo method, performed the numerical simulations and respective analysis of the results and wrote the draft of the manuscript. The author finalized the paper together with the co-authors.
- III. The author planned the work together with the co-authors, performed the numerical simulations and respective analysis of the results and wrote the draft of the manuscript. The author finalized the paper together with the co-authors.
- IV. The author planned the work together with the co-authors and wrote the draft of the manuscript with S. Ghorai. The author performed numerical calculations and respective analysis of results with E.K. Delczeg-Czirjak for varying concentrations of Fe-Mn. The calculations on the disordered supercells (prepared by S.I. Simak) were performed by the author, as well as the Monte Carlo simulations for the magnetic composite and respective analysis. The author finalized the paper together with the co-authors.



# Contents

1	Introduction .....	9
1.1	Magnetocaloric Effect .....	10
1.2	Magnetic Refrigeration .....	11
1.3	Magnetocaloric Materials .....	14
1.4	Scope of the Thesis .....	16
2	Elements of Thermodynamics and Physical Statistics .....	17
2.1	Thermodynamics of MCE .....	17
2.2	Entropy .....	22
2.2.1	Electronic Entropy .....	24
2.2.2	Lattice Entropy .....	25
2.2.3	Magnetic Entropy .....	28
3	First-principles Calculations .....	32
3.1	Basics of Density Functional Theory .....	32
3.2	Linear-Muffin-Tin-Orbitals (LMTO) method .....	35
3.3	Korringa-Kohn-Rostoker (KKR) method .....	36
3.4	Projected-Augmented-Wave (PAW) method .....	38
3.5	Simulating Disorder .....	39
3.6	DFT+U .....	40
3.7	Applications .....	41
3.7.1	Phonon Calculations .....	41
3.7.2	Elastic Properties .....	43
3.7.3	Exchange Parameters ( $J_{ij}$ ) .....	44
4	Magnetic Monte Carlo Simulations .....	46
4.1	Metropolis Monte Carlo .....	46
4.2	Quantum Rescaled Monte Carlo .....	47
4.3	Mixed Rescaling .....	50
4.4	Remarks and Outlook .....	54
5	Benchmarking Entropy Calculations .....	55
5.1	FeRh .....	55
5.2	Gadolinium .....	58
5.3	Remarks .....	61
6	Magnetism and Lattice Coupling .....	63
6.1	FeRh .....	63
6.2	Gadolinium .....	65
6.3	$\text{Mn}_{0.5}\text{Fe}_{0.5}\text{NiSi}_{0.95}\text{Al}_{0.05}$ .....	72
6.4	Remarks .....	81
7	High-throughput Calculations .....	82
7.1	Workflow .....	83

7.2	Screening parameters .....	85
7.3	Preliminary results .....	86
7.4	Remarks and Outlook .....	89
8	Conclusions .....	90
	Popular Science Summary .....	93
	Populärvetenskaplig sammanfattning .....	95
	Acknowledgments .....	97
	Bibliography .....	100

# 1. Introduction

*'Cause we are living in a material world  
And I am a material boy  
You know that we are living in a material world  
And I am a material boy*

---

paraphrasing Madonna's "Material Girl"

Since the dawn of civilization, mankind has explored the properties of the different materials found in nature in the interest of survivability and comfort. For instance, natural resources such as wood, stone, and wool have distinct physical properties, which makes them more or less suitable for different applications. We did not limit ourselves to existing natural materials. We proceeded to modify their properties and even create new materials. The development of pottery, the invention of bronze, and later steel are fine examples of milestones in materials manufacture. Over the ages, discovering and mastering materials and their properties have played a critical role in shaping societies and driving technological advancements - we live in a materials world.

Nowadays, this pursuit for better materials continues. Perhaps even more intensively than ever, as we direct our efforts on developing new technologies and improving the current ones, with a focus on energy efficiency, such as cooling/refrigeration devices. Cooling devices encompass familiar appliances in our daily lives, such as freezers, fridges for cold processing and refrigeration, and air conditioning units (AC) for space cooling. These devices hold a significant percentage of domestic energy consumption, with refrigeration representing around 4% of the total usage (4.2% Germany [1], 3.7% USA [2], 5% Hong Kong [3]), while space cooling can reach a higher portion of the energy consumption 5.9 [4] (0.2% Germany [1], 9.1% USA [2], 26% Hong Kong [3]). With the improvement of infrastructure and standard of living, especially in hotter regions of the world, the adoption of AC is rising. This rise is augmented by the increasing frequency of extreme heat events and record-high temperatures worldwide due to global climate change. As a result, the demand for space cooling solutions is reaching unprecedented levels, translating to a substantial increase in energy requirements.

Innovating and developing energy-efficient cooling technologies is crucial to address the escalating energy demand. Today, one of the most promising alternatives is the application of caloric materials in cooling technology. Caloric materials are a class of materials that show a large and reversible thermal response under an externally applied field. In simpler terms, these materials can switch back and forth between two temperatures when an external force is applied and then removed. Depending on the nature of the applied field, caloric materials can be classified into several subclasses:

- Electrocaloric: responds to an electric field.
- Barocaloric: responds to pressure application.
- Elastocaloric: responds to mechanical stress.
- Magnetocaloric: responds to a magnetic field.

It is important to note that caloric materials do not necessarily belong exclusively to a single subclass. They can simultaneously exhibit multiple responses. Among caloric materials, magnetocalorics materials were the focus of research and shown to be a solid alternative for building cooling devices, capable of reaching an improvement of energy efficiency near to 30% compared to conventional vapour-compression devices [5, 6]. In addition, the adoption of this technology allows to avoid greenhouse gases, making the devices more environmentally friendly and cooling more sustainable.

While this technology offers numerous advantages, it has not yet become an integral part of our daily lives. The primary obstacles to its widespread adoption lie in the cost and operative limitations of magnetic cooling devices. This challenge has attracted research efforts aimed at enhancing affordability and accessibility to domestic use. One crucial avenue of investigation in this field, followed in this work, revolves around the discovery of novel magnetocaloric materials.

## 1.1 Magnetocaloric Effect

The thermal response of a magnetic material in an applied magnetic field is known as the magnetocaloric effect (MCE). This effect was reported first<sup>1</sup> by P. Weiss and A. Piccard in 1917 [8], who measured the temperature variation induced by changing the magnetic field applied in nickel samples close to their Curie temperature. The reversible temperature change ( $\Delta T_{ad}$ ) produced upon a magnetic field variation, as observed in the experiment, fully characterizes the MCE in an adiabatic process [9].

On the other hand, in the context of an isothermal process, the MCE is characterized by an entropy change ( $\Delta S_{iso}$ ) [9]. Since entropy can be seen (roughly) as a quantifier of the disorder, we can also associate the MCE to a change in the 'magnetic disorder' as a response to an applied magnetic field. While  $\Delta T_{ad}$  provides a more intuitive metric that can be directly measured, the indirect measurement of  $\Delta S_{iso}$  is often preferred in the literature for comparing the MCE in different materials. This preference can be attributed, in part, to the challenge of maintaining adiabatic conditions necessary for reliable  $\Delta T_{ad}$  measurements [10], making  $\Delta S_{iso}$  the preferable option within the magnetocaloric community. Nevertheless, both quantities are important when quantifying the performance of the MCE [11].

Though the MCE is present in all magnetic materials, generally, it is too small to be used in practical applications. Yet, the effect can be enhanced when

---

<sup>1</sup>Curiously in the last 20-year period [7], the discovery has been misattributed to Warburg in 1881.

the system is near a phase transition. Materials exhibiting amplified MCE hold a particular interest and relevance for technological applications. Those materials are classified as magnetocaloric. Note that magnetocaloric materials to be functional through the MCE, need to be operated close to their phase transitions, defining a (very) limited temperature range where the MCE can be explored. Thus, the magnetocaloric material must be chosen according to the cooling range of the application.

In light of these material properties, magnetocaloric materials have attracted attention for their potential applications in magnetic hyperthermia therapy, waste heat conversion, and magnetic refrigeration [12]. For instance, magnetic hyperthermia therapy is a medical technique which makes use of magnetic nanoparticles to deliver drugs within the body or to target tumour cells. These nanoparticles generate heat under alternating magnetic fields, enabling controlled drug release or targeted destruction of cancer cells through controlled overheating [13]. Given the localized nature of magnetic fields, this technique offers a noninvasive and precise method for heat delivery. The enhanced thermal response of magnetocalorics makes them an appealing choice for the composition of the nanoparticles [14].

Additionally, magnetocalorics can be integrated into thermomagnetic (pyromagnetic) devices to harvest the heat generated as a waste byproduct of e.g. industrial processes and convert it into electrical energy, either directly or indirectly via mechanical energy [15]. This approach is still in its early stages but holds significant potential for sustainable energy recovery.

While magnetocaloric materials have found other applications, magnetic refrigeration always has been a primary focus and a driving force behind their study. Magnetic refrigeration, with its potential for efficient and environmentally friendly cooling, has not only motivated rigorous investigation into these materials, which significantly contributed to our understanding of their unique properties. Within magnetic refrigeration, a special focus has been given to the development of room-temperature technologies to bring the benefits of this technology to daily use.

## 1.2 Magnetic Refrigeration

In magnetic cooling devices, the MCE is explored using combinations of thermodynamic processes such as adiabatic, isothermal and isofield magnetizations. The optimal magnetic refrigeration system, following the principles of the Carnot cycle, operates using two adiabatic and two isothermal processes, as depicted in Figure 1.1:

- **Adiabatic (partially) magnetization (A - B):** the process begins with the application of a magnetic field, which can be adiabatically increased (or if  $H_0 \neq 0$ , intensified). This aligns the magnetic moments parallel to the field, causing the temperature of the magnetocaloric material to rise (point B).

- **Isothermal heat release (B - C):** Subsequently, the heat is allowed to flow (lifting the adiabatic conditions), and the magnetocaloric material is brought into contact with a hot sink (isothermal conditions). As the magnetic field continues to increase, the magnetic moments align further with the field, resulting in a reduction of entropy (point C) as the magnetic moments become more 'ordered'.
- **Adiabatic (partially) desmagnetization (C - D):** Once the maximum magnetic field ( $H_1$ ) is reached, the contact with the hot sink is removed. The magnetic field is then reduced adiabatically, causing the magnetocaloric material's temperature to decrease. This reduction in temperature occurs as the orientation of the magnetic moments starts to deviate from their aligned configuration (point D).
- **Isothermal heat absorption (D - A):** In the final process isothermal conditions are re-established, this time with a cold reservoir (the system to be refrigerated). The magnetic field is gradually decreased, causing the magnetic moments to become less ordered and leading to an increase in entropy (point A).

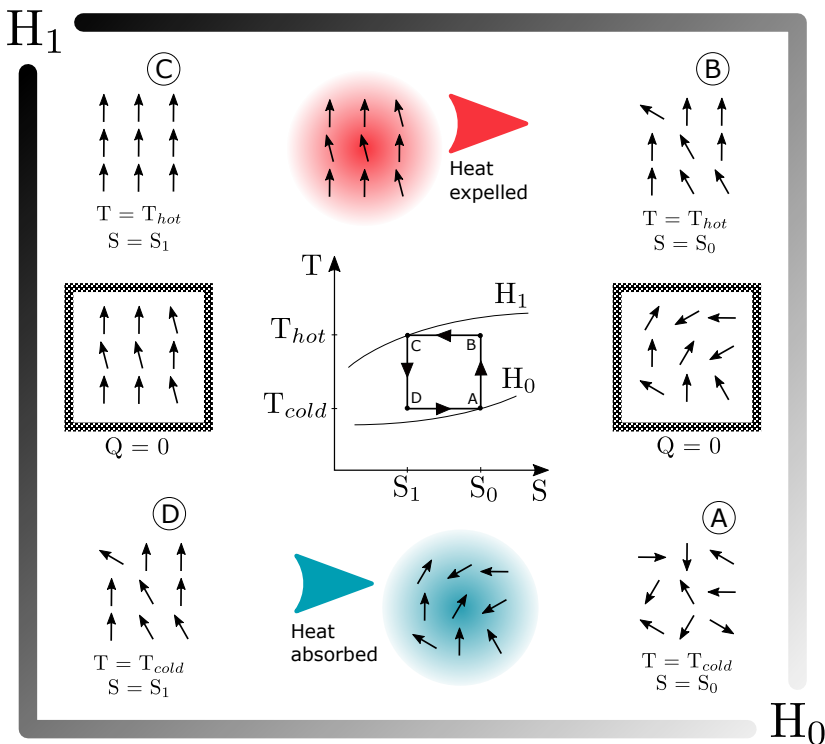


Figure 1.1. Representation of the Carnot cycle for magnetic refrigeration in a conventional ferromagnetic material.

In ideal conditions in the Carnot cycle the heat ( $Q$ ) exchanged between the cold and hot sink is given by  $Q = \Delta T_{ad} \Delta S_{iso}$ . While, in theory, this thermodynamic cycle is the most efficient one possible, in practice its application in room temperature devices is limited and inefficient [16], since it needs to be operated in a temperature range equal to  $\Delta T_{ad}$ . In the context of room-temperature refrigeration, other simplified thermodynamics cycles are discussed instead [17, 16, 18] as the Ericsson cycle which operates within two isofield and two isothermal processes, and the Brayton cycle that consists of two adiabatic processes and two isofield processes. Using these as bases, more complex and efficient cycles have been proposed, such as the magnetic cascade cycle [16] and the active magnetic regenerator cycle [16, 18].

Taking into account the operation of magnetic thermodynamics cycles, we can in general list four elements essential for a magnetic refrigerator [10, 16]:

- magnetocaloric material (the refrigerant)
- a source of the magnetic field and mechanism to regulate its application in the magnetocaloric
- hot and cold heat exchangers that handle the heat transfer to the hot and cold sink respectively
- heat transfer fluid, which pumps the heat between the magnetocaloric and the exchangers.

In the development of household magnetic cooling devices essential to optimize and integrate these elements, while keeping cost-efficiency in mind. This optimization raises different challenges in the realms of engineering, physics, and material science [12]. Within the context of physics, one of the main focuses has been dedicated to exploring the properties of the magnetocaloric material.

Although the concept of magnetic refrigeration devices is not new and has been applied long ago in paramagnetic salts at cryogenic temperatures [19, 20, 21], its development at room temperature is more recent. Historically, magnetic refrigeration at room temperature was developed around Gd-based materials. In 1976, Gerald V. Brown proved that magnetic refrigeration was feasible at room temperature with his, first of its kind, magnetic refrigerator with Gd as magnetic refrigerant [22]. Slowly, this field started capturing the attention of the scientific community till 1997, when Pecharsky and Gschneidner observed a giant MCE in the  $\text{Gd}_5(\text{Si}_2\text{Ge}_2)$  [23], establishing an important development of the field and attracting further investigation which led to a quick raise of scientific publications related with magnetocaloric refrigeration [24, 25]. In that work [23], Pecharsky and Gschneidner verified that  $\text{Gd}_5(\text{Si}_2\text{Ge}_2)$  has a first-order transition at 276K, and an entropy variation of 14 J/kg/K under application of a magnetic field of 2T was measured, considerably higher than other compounds known at the time.  $\text{Gd}_5(\text{Si}_2\text{Ge}_2)$  has shown a small thermal hysteresis, ideal for application in refrigeration devices. Unfortunately, being based on Gd, the commercialization of this material for domestic use is not economically appealing, which motivated the search for other materials. Despite its commercial

limitations, due to their great properties, Gd-based magnetocalorics are often used in prototypes and demonstrators of magnetic cooling devices [17].

### 1.3 Magnetocaloric Materials

As mentioned above, the performance of magnetocaloric materials in refrigeration cycles depends on both the  $\Delta S_{iso}$  and  $\Delta T_{adi}$  parameters [26]. However, both quantities only have significant values in a limited temperature range around the magnetic phase transition. This makes the temperature at which the magnetic phase transition occurs the first parameter to consider when evaluating the applicability of a specific magnetocaloric material.

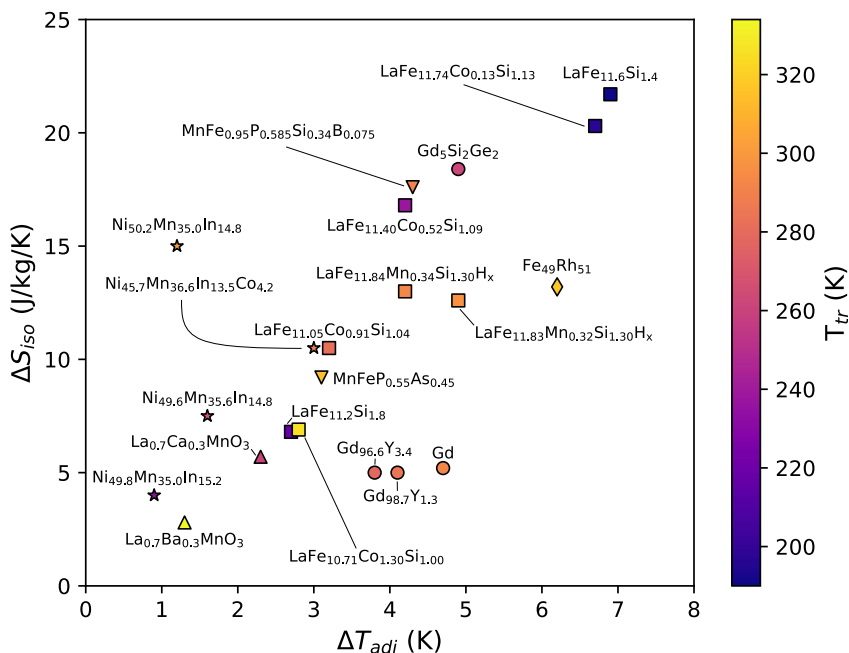


Figure 1.2. Magnetocaloric properties under cycling 2T field conditions. The colours indicate the temperature of the transition ( $T_{tr}$ ) associated with the magnetocaloric effect, while the different symbols group the compounds of the same class. Data extracted from Ref. [27].

Currently, within the most promising magnetocaloric materials for room-temperature applications, we find compounds related to MnAs,  $La(Fe,Si)_{13}$ ,  $Fe_2P$ , FeRh, NiMn-based Heusler alloys,  $LaMnO_3$ -like perovskites, Gd-based (and other rare earths) intermetallics [14, 27]. In Figure 1.2 we can get an idea of the magnitudes of  $\Delta S_{iso}$  and  $\Delta T_{adi}$  for interesting candidates within these classes [27]. In the context of this figure, the ideal magnetocaloric would be in the upper right corner to have a great MCE and be coloured with a tone between



yellow and orange coloured. Unfortunately, few compounds match those conditions, only the FeRh alloy and the  $\text{MnFe}_{0.95}\text{P}_{0.585}\text{Si}_{0.34}\text{B}_{0.075}$  for the  $\text{Fe}_2\text{P}$  family. In the figure, it is evident from a comparison of similar compounds, that the magnetocaloric properties are tunable to a certain degree. This motivates the continuation of research into these families, in an attempt to optimise the materials for a room-temperature application. Moreover, current investigations in Ni-Co-Mn-Ti Heuslers and  $\text{Mn}_{0.5}\text{Fe}_{0.5}\text{NiSi}_{1-x}\text{Al}_x$  alloys have shown to be promising and are gathering more attention [28].

It is also worth mentioning the existence of some research on magnetocaloric amorphous materials [29] and high-entropy alloys [30, 31] as the Fe-Mn-Ni-Ge-Si [32]. These materials usually show a smaller entropy variation, but an increased adiabatic temperature variation which can make their performance competitive with the compounds discussed earlier. A practical advantage that the materials offer is that their physical properties can be easily tuned [29].

Besides the mentioned figures of merit (temperature of the transition,  $\Delta S_{iso}$ ,  $\Delta T_{adi}$ ) [16, 18] there are other keys properties desirable to be present in a magnetocaloric for integration in cooling device:

- low Debye temperature
- low thermal or magnetic hysteresis
- low specific heat and high thermal conductivity
- high electrical resistance
- resistance to corrosion
- mechanically resilient and tough
- non-toxic
- low manufacturing costs and scalable production
- low environmental impact

Discovering a material that reunites (almost) all these properties, with a high  $\Delta S_{iso}$  and  $\Delta T_{adi}$  at room temperature constitutes the holy grail on the search of magnetocalorics for room temperature devices.

## Challenges

Despite the promising characteristics of the candidates depicted in Figure 1.2 there exist significant hurdles preventing their integration into magnetic cooling devices.

One notable example is the utilization of FeRh alloys, which exhibit remarkable MCE properties. However, rhodium (Rh) is exorbitantly expensive making it impractical to use [14, 27]. Similarly, the price of elements like germanium (Ge), gallium (Ga), and indium (In) would make compounds with these elements too expensive to be integrated into devices for commercial production [14].

Further limiting the pool of viable options, rare-earth-based compounds, like Gd alloys, while displaying attractive properties, are hindered by their costs [14, 27]. More importantly, the geopolitical sensitivity surrounding the mining and

processing of these compounds, due to their limited availability in economically significant quantities, discourages their application.

Taking into account these considerations the pool of viable magnetocalorics becomes very limited, underscoring the interest in finding new magnetocaloric materials, in order to make the technology commercially competitive.

Another crucial challenge to the development of magnetic cooling devices is the issue of hysteresis [33, 25]. Magnetocalorics with sharp magnetic transitions, which inherently yield the desired high  $\Delta S_{iso}$  and  $\Delta T_{adi}$ , inevitably have hysteresis losses. When subjected to cyclic conditions, hysteresis leads to a reduction in the effective  $\Delta S_{iso}$  and  $\Delta T_{adi}$ , resulting in compromised performance.

Recently [33, 34, 35] an innovative solution to this challenge was proposed: incorporating materials that exhibit not only magnetocaloric effects but also demonstrate barocaloric responses (pressure-response) should overcome the problems above described. Exploring multiple caloric responses in the thermodynamics cycles, coupled with strategic alloying or doping to fine-tune material properties, holds exceptional promise in mitigating the performance decay of magnetocaloric materials under cyclic conditions.

## 1.4 Scope of the Thesis

This thesis explores the intricate world of magnetocaloric materials, focusing on the entropy variation linked to the MCE using first-principles calculations. More exactly, it investigates the feasibility of a theoretical high-throughput search for new magnetocaloric materials, detailing the initial steps of such an approach.

The theoretical framework is established in the first few chapters (Chapters 2-4). Chapter 2 introduces the fundamental principles of the MCE. Chapter 3 describes the ab-initio methods utilized in this research, while Chapter 4 details the methodology for conducting magnetic simulations. This chapter also introduces and discusses a novel scheme proposed in Paper II.

The following chapters (Chapters 5-6) summarize the main results and models proposed in the Papers included in the thesis. Chapter 5 presents a summary of benchmark tests conducted on FeRh (as detailed in Paper I) and Gd (as in Paper II). In Chapter 6, the focus shifts to the interaction between lattice and magnetic subsystems. This interaction is explored in greater depth for Gd (in Paper IV) and for  $Mn_{0.5}Fe_{0.5}NiSi_{0.95}Al_{0.05}$  (in Paper III).

Furthermore, Chapter 7 offers an overview of the preliminary results from ongoing high-throughput calculations, with these findings being directly discussed in the thesis (manuscript in preparation).

In conclusion, the thesis encapsulates the key findings, drawing together the significant conclusions from the study.

## 2. Elements of Thermodynamics and Physical Statistics

*Order, entropy; a never-ending cycle.*

---

Heimerdinger

In this chapter, the theoretical background needed to understand the MCE is outlined.

### 2.1 Thermodynamics of MCE

A good start is the beginning so we start with the first law of thermodynamics: [9, 36]

$$dU = \delta Q - \delta W \quad (2.1)$$

with  $U$ ,  $Q$  and  $W$  as the internal energy, the heat flux and the performed work respectively. In the standard formulation,  $W$  often includes exclusively the mechanical work  $\delta W_{mec} = pdV$ . However, in magnetic materials, it is also convenient to add the magnetic work  $\delta W_{mag} = -\mu_0 H dm$ , which describes the change in the magnetic moment ( $m$ ) under the application of an external magnetic field ( $H$ ). If we consider a reversible process, the second law of thermodynamics tells us that  $\delta Q = TdS$ . Then we can expand Equation (2.1) to:

$$dU = TdS - pdV + \mu_0 H dm . \quad (2.2)$$

We have now a working expression for the internal energy, capable of describing the magnetocaloric effect. However, this differential equation is a function of entropy, volume and magnetic moment while it would be more convenient to have this relation in terms of the temperature, pressure and magnetic field, after all these are the parameters that we can easily measure and control experimentally. In order to do so, we can use a Legendre transformation to a different thermodynamic potential than  $U$ . A common choice is to use the Gibbs energy, that given Equation (2.2), would be defined as:

$$G = U - TS + pV - m\mu_0 H \quad (2.3)$$

$$dG = \left( \frac{G}{\partial p} \right)_{T,H} dp + \left( \frac{G}{\partial T} \right)_{p,H} dT + \left( \frac{G}{\partial H} \right)_{p,T} dH \quad (2.4)$$

$$= Vdp - SdT - m\mu_0 dH . \quad (2.5)$$

By comparing (2.4) with (2.5), and taking into account the equality between mixed second partial derivatives (Schwarz's theorem)  $\frac{\partial^2 G}{\partial T \partial H} = \frac{\partial^2 G}{\partial H \partial T}$  we get the Maxwell's relation, which relates the entropy with the magnetic moment:

$$\left(\frac{\partial S}{\partial H}\right)_{p,T} = \mu_0 \left(\frac{\partial m}{\partial T}\right)_{p,H} \quad (2.6)$$

$$dS = \left(\frac{\partial S}{\partial T}\right)_{H,p} dT + \left(\frac{\partial S}{\partial H}\right)_{T,p} dH. \quad (2.7)$$

In an isothermal process ( $dT = 0$ ) Equation (2.7) is reduced to :

$$dS_{iso} = \left(\frac{\partial S}{\partial H}\right)_{T,p} dH \quad (2.8)$$

then, combining Maxwell's relation with Equation (2.6) one obtains the entropy variation induced by the application of a magnetic field:

$$\Delta S_{iso} = S(T, H_f) - S(T, H_i) = \int_{H_i}^{H_f} \mu_0 \left(\frac{\partial m}{\partial T}\right)_{H,p} dH. \quad (2.9)$$

In a reversible adiabatic process ( $\delta Q = 0$ ), the entropy of a system is conserved ( $dS=0$ ), thus Equation (2.7) give us the following equality:

$$\begin{aligned} \left(\frac{\partial S}{\partial T}\right)_{H,p} dT &= - \left(\frac{\partial S}{\partial H}\right)_{T,p} dH \\ dT &= - \left(\frac{\partial S}{\partial T}\right)_{H,p}^{-1} \left(\frac{\partial S}{\partial H}\right)_{T,p} dH. \end{aligned} \quad (2.10)$$

Taking Maxwell's relation in Equation (2.6) and the definition of heat capacity,

$$C = \delta Q/dT = T \left(\frac{dS}{dT}\right) \quad (2.11)$$

the previous relation can be rewritten as:

$$dT = -\mu_0 \frac{T}{C_{H,p}} \left(\frac{\partial m}{\partial T}\right)_{H,p} dH \quad (2.12)$$

thus:

$$\Delta T_{adi} = -\mu_0 \int_{H_i}^{H_f} \frac{T}{C_{H,p}} \left(\frac{\partial m}{\partial T}\right)_{H,p} dH \quad (2.13)$$

From Equation (2.13), follows that the adiabatic temperature is enhanced in materials with low heat capacity provided the magnetic entropy change and temperature remain the same. Further, comparison of Equation (2.9) and

(2.13), tells us (as long as  $C_V > 0$ ) that  $\Delta T_{adi}$  peak is always opposite to  $\Delta S_{iso}$ .

Note that the term  $\partial m/\partial T$  appears in Equations (2.9) and (2.13). Since large variations in the magnetic moment are often found in the vicinity of magnetic phase transitions, the dependence from this term of  $\Delta S_{iso}$ , explains the enhancement of the MCE. In the case of ferromagnetic materials, for example, the MCE will be larger at the magnetic (Curie) ordering temperature and is bigger for materials with large magnetization and/or sharp variations in the magnetization as in first-order transitions.

Since the field dependence is not explicit in  $(\frac{\partial m}{\partial T})_{H,p}$  it is convenient to rewrite it such that the relation becomes more evident. To couple the change of the magnetic moment explicitly to the magnetic field, one can make use of the magnetic susceptibility ( $\chi$ ). In general terms, magnetic susceptibility is a measure of the magnetization response to an applied magnetic field:

$$\mathbf{M} = \chi \mathbf{H} . \quad (2.14)$$

Calculating the partial derivative of this gives us:

$$\begin{aligned} \frac{1}{V} \frac{\partial \mathbf{m}}{\partial T} &= \frac{\partial \chi}{\partial T} \mathbf{H} + \chi \frac{\partial \mathbf{H}}{\partial T} \\ \left( \frac{\partial m}{\partial T} \right)_H &= V \frac{\partial \chi}{\partial T} H . \end{aligned} \quad (2.15)$$

Equation (2.15) makes it evident how  $\Delta S_{iso}$  and  $\Delta T_{adi}$  increase with the magnetic field applied. Moreover, the general behaviour of  $\partial \chi/\partial T$  is known for different magnetic orderings (see Figure 2.1), allowing us to identify the cases where MCE is enhanced for conventional magnetic materials. As illustrated in Figure 2.1,  $\partial \chi/\partial T$  reaches its maximum close to the magnetic ordering temperature (Curie temperature for ferromagnetic,  $T_C$ , and Néel temperature for anti-ferromagnetic  $T_N$  systems), varying slowly ( $\approx 1/T$  in the high-temperature limit). This explains the enhancement of the MCE close to phase transitions in conventional order-disorder transformations. The order of magnitude of  $\chi$  is also relevant for the MCE, as materials with higher  $\chi$  will have a bigger  $\partial \chi/\partial T$  in the transition. Thus, ferromagnetic (FM) and ferrimagnetic (FiM) materials are of special interest for magnetocaloric applications since in general, their  $\chi$  is an order of magnitude bigger than paramagnetic (PM) and antiferromagnetic (AFM) materials, as seen in Figure 2.1. Analysing the  $\chi$  slopes in Figure 2.1 clarifies the exploration of the MCE from paramagnetic salts at cryogenic temperatures. Additionally, given the slow variation of the susceptibility even at low temperatures, it becomes clear that a weak MCE should be expected for conventional antiferromagnetic materials.

The discussion above highlights the importance of a large variation of  $(\frac{\partial m}{\partial T})_H$  or  $\frac{\partial \chi}{\partial T}$  for an enhanced MCE, explaining while the effect is stronger in the vicinity of a phase transition. While the absolute values of  $m$  or  $\chi$  play a

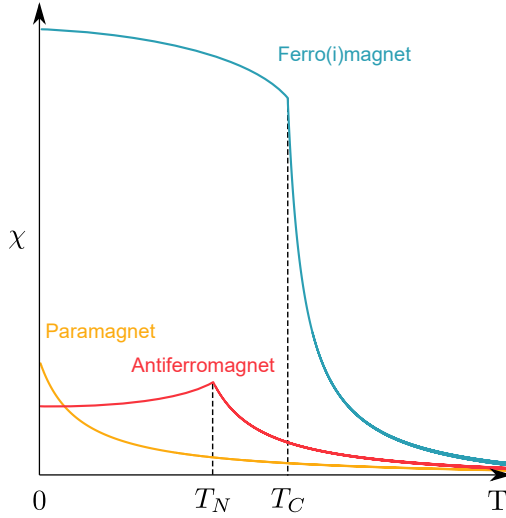


Figure 2.1. Illustration of the temperature dependence of the magnetic susceptibility for different magnetic orders. Ferrimagnets have a susceptibility that qualitatively resembles a ferromagnet, in particular, close to  $T_C$ .

role for these quantities, an equally important feature is the sharpness of the magnetic transitions.

### Order of the transition

The sharpness of a transition is closely related to its order. Phase transitions can be classified (Ehrenfest classification) according to the lowest derivative of temperature or generalized force (e.g. magnetic field, pressure) of the free energy that is discontinuous. Thus, a first-order transition has  $\frac{\partial G}{\partial x}$  ( $x = T, P, H$ ) discontinuous at the transition. Comparing Equations (2.5) and (2.4), we see these derivatives correspond, to the entropy, volume and magnetic moment, meaning that in first-order transitions these physical quantities change discontinuously. In a similar way, second-order transitions have discontinuities in  $\frac{\partial^2 G}{\partial x^2}$ , which manifests as discontinuous changes in the heat capacity, compressibility and differential magnetic susceptibility [37]. In real materials, these quantities are not exactly discontinuous but present sharp variations.

Due to these distinct properties between the 1st and 2nd order transitions different considerations are needed to calculate  $\Delta S_{adi}$ , see Figure 2.2. One convenient way (for both theoretical and experimental studies), is to explore the thermodynamic relation between heat capacity and entropy (Equation (2.11)) and integrate the heat capacity measured at two different magnetic fields  $H_1$  and  $H_2$ :

$$\Delta S(T) = \int_0^T \frac{C(T)_{H_2} - C(T)_{H_1}}{T} dT . \quad (2.16)$$

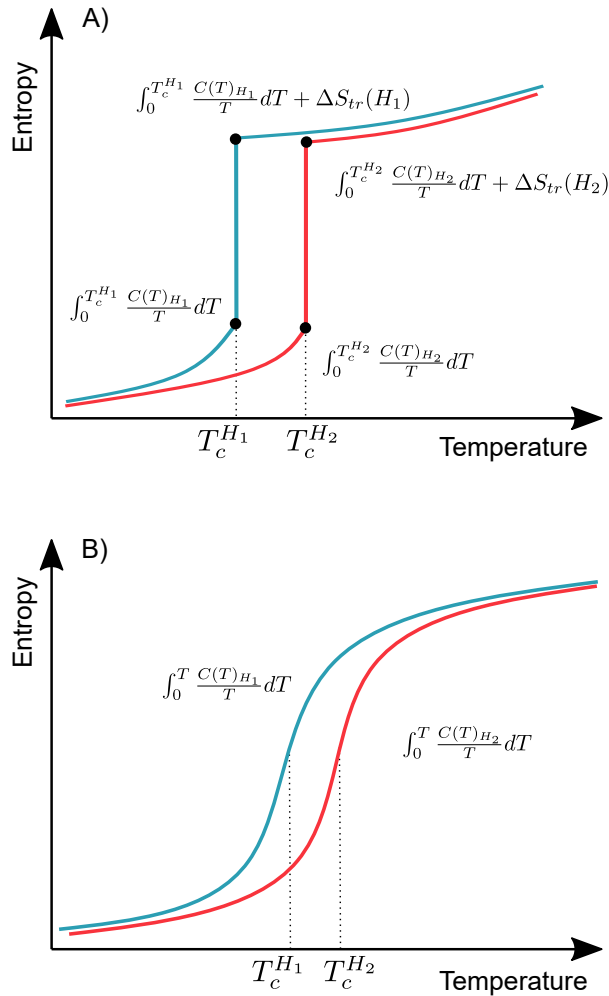


Figure 2.2. Illustrative T-S diagram of a magnetic system in the vicinity of first-order (a) and second-order (b) phase transition in two magnetic fields,  $H_1$  and  $H_2$ . a) Values of entropies at critical points are marked.

While this relation is valid for both first and second-order transitions, in first-order transitions, the discontinuity in the entropy implies an infinite spike in the heat capacity at the phase transition. This infinite spike refers to the latent heat ( $L$ , also known as heat/enthalpy of transformation) absorbed or emitted by the system during the transformation, as the temperature of the system will not change until the transformation is completed<sup>1</sup>. This mathematical singularity does not allow for direct integration of the heat capacity in the expression above. Instead, we need to reformulate Equation (2.16) to include the discontinuity of the entropy above the transition temperature, keeping in mind that the

<sup>1</sup>Just as we explore in a Bain-marie to melt e.g. chocolate.

transition temperature depends on  $H$ . For temperatures within the range defined by both transition temperatures for  $H = H_1$ , and  $H = H_2$  the analogous of Equation (2.16) for first-order transitions can be approximated to [38, 37]:

$$\Delta S(T) = \int_0^T \frac{C(T)_{H_2} - C(T)_{H_1}}{T} dT + \Delta S_{tr}(H) \quad (2.17)$$

where  $\Delta S_{tr}(H)$  is the discontinuous jump in entropy given by the difference between the entropies of the low and high-temperature states (see Figure 2.2a). The term  $\Delta S_{tr}(H)$  is a temperature-independent constant related to the latent heat associated with the first-order transition as  $L/T_{tr}$ . Since it has a weak dependence on the magnetic field, it is often reasonable to approximate  $\Delta S_{tr}(H_1) \approx \Delta S_{tr}(H_2)$  [38].

Comparing Equation (2.16) and (2.17) we can understand that first-order transitions have inherently a bigger entropy variation due to the additional term<sup>2</sup>. In fact, first-order transitions have often  $\Delta S_{tr}$  big enough so this term is the major contribution to the entropy change. For such cases, the main role of the magnetic field is not so much to change the heating properties as it is shifting the phase transition temperature.

Although it is out of the scope of this work, it is important to note that first-order transitions have always a hysteresis associated, which leads to losses of performance in magnetocaloric materials under cyclic conditions. While  $\Delta S$  is not very strongly affected by hysteresis, the different transition temperatures at  $H_1$  and  $H_2$  get closer, reducing effectively  $\Delta T_{adi}$  and the amount of heat exchange on the magnetocaloric refrigeration cycle.

## 2.2 Entropy

Entropy is a thermodynamic variable often associated with the 'disorder' of the system. Such association can provide a good illustration when comparing high and low entropy states for example the spins configurations (A) and (C) in Figure 2.3.

However, it can mislead in some cases and its physical interpretation is very limited. In statistical physics, entropy quantifies the number of distinct configurations (microstates,  $\Omega$ ) available to a system in a particular thermodynamic state:

$$S = k_B \ln(\Omega) \quad (2.18)$$

where  $k_B$  is the Boltzmann constant. From this definition, we can relate entropy with the different degrees of freedom of the system. To illustrate this point, let us revisit spin configurations (A) and (B) in Figure 2.3. On spin configuration (A), where the system is disordered and there is high entropy, we could rearrange the spins in different ways, equally disordered, without changing any of

<sup>2</sup>Note that  $\Delta S_{tr} > 0$  so the transition happens spontaneously.



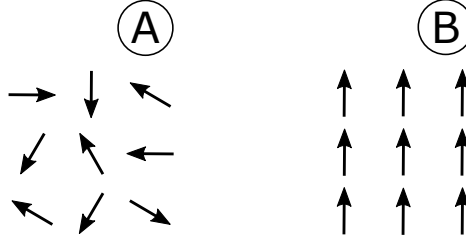


Figure 2.3. Illustration of spin configurations with different levels of disorder: the high entropy state (A) and the low entropy state (B).

the (macroscopic properties of the system) as the total magnetic moment and energy. These multiple possible configurations imply a high entropy value. In contrast, we have case (B) where the spins align along the direction of the external magnetic field. In such a case, there is only one way of rearranging the spins' orientation while keeping them aligned with the magnetic field. Hence resulting in a low entropy value.

The entropy of a system is closely related to fluctuations from the ground state. Fluctuations can be thought of as the system randomly exploring different microstates. As a system fluctuates and explores different configurations, its entropy tends to increase, since the number of accessible configurations grows. It seems logical that, during this exploration, the system is more likely to be found in the macrostate that has more microstates. Hence, entropy plays an important role in the stabilization of the state of a system. This clarifies why higher temperatures lead to increased thermal fluctuations, driving the system towards states with higher entropy, often characterized by greater 'disorder'. As is the case e.g. for ferromagnetic systems that become magnetically disordered above the Curie temperature. This role of the entropy to stabilize a state becomes evident in the  $TS$  term of the Gibbs (see Equation (2.4)) and Helmholtz energies.

As mentioned above, in magnetocaloric systems the entropy variation induced by the magnetic field is a figure of merit for the characterization of the MCE and for the performance in magnetic refrigeration. Commonly, the electronic, the structural (lattice) and the magnetic degrees of freedom enter the entropy and are treated as independent contributions,  $S_{ele}$ ,  $S_{lat}$ ,  $S_{mag}$  respectively. The total entropy is then given by [39]:

$$S_{tot} = S_{ele} + S_{lat} + S_{mag} . \quad (2.19)$$

It's important to note that assuming the decoupling of contributions can be a significant simplification in many cases. For example, in materials with itinerant magnetism or/and magnetism lead by  $3d$ -electrons, there is a strong coupling between the different degrees of freedom, so the description of the entropy

as in Equation (2.19) can lead to double counting of entropy contributions [38]. Moreover, most of the magnetocaloric systems of interest (e.g. FeRh, Fe<sub>2</sub>P and Heusler alloys) display magnetostructural transitions, hinting at a strong coupling between lattice and magnetic components. Unfortunately, the current knowledge on the accurate treatment of these couplings is limited, so often models are tailored to specific materials. In fact, the absence of a description that is both general and accurate is one of the main challenges in the study of magnetocaloric materials.

In general (while using Equation (2.19)) it is often considered that the application of the magnetic field has a direct effect only on  $S_{mag}$ , playing no part in  $S_{ele}$  and  $S_{lat}$  [38]. In such scenarios, we can deduce that during adiabatic processes, the change in magnetic entropy ( $\Delta S_{mag}$ ) induced by the magnetic field is absorbed by the electronic and lattice subsystems:

$$\begin{aligned} \Delta S_{tot} &= 0 \quad (\text{adiabatic process}) \\ -\Delta S_{mag}(T, H) &= \Delta S_{ele}(T) + \Delta S_{lat}(T) \end{aligned}$$

explaining the constant entropy in the adiabatic processes A→B and C→D in Figure 3.1) despite alterations in the alignment of the spin moments. While this 'proof' is trivial, it provides us with physical insight into how the change of the magnetic order leads to a temperature change.

Before diving into individual entropy contributions, let's first compare their relative magnitudes. In magnetocaloric materials, as it might have been expected, the dominant term is  $\Delta S_{mag}$ . In the following terms,  $\Delta S_{lat}$  usually dominates over  $\Delta S_{ele}$ . For materials undergoing magnetostructural transitions,  $\Delta S_{lat}$  can become comparable in magnitude to the magnetic contribution. Since electronic entropy is usually considerably smaller in magnetocaloric materials is often omitted in the description.

## 2.2.1 Electronic Entropy

Electronic entropy arises from the occupation of vacant electronic states by electrons within a system. At  $T = 0$  the system is in its ground state and  $S_{ele} = 0$ . At finite temperatures, thermal fluctuations allow the electrons to occupy excited states increasing the possible electronic configurations and thus the electronic entropy. Formally,  $S_{ele}$  is defined as the mixing entropy of occupied and unoccupied states [40]:

$$\begin{aligned} S_{ele} &= -k_B \int D(\epsilon) \left[ (1 - f(\epsilon, T)) \ln (1 - f(\epsilon, T)) \right. \\ &\quad \left. + f(\epsilon, T) \ln (f(\epsilon, T)) \right] d\epsilon . \end{aligned} \quad (2.20)$$

Here,  $D(\epsilon)$  represents the electronic density of states, and  $f(\epsilon, T)$  is the Fermi-Dirac distribution function:

$$f(\epsilon, T) = \left[ \exp\left(\frac{\epsilon - \mu}{k_B T}\right) + 1 \right]^{-1} \quad (2.21)$$

$$N_{ele} = \int D(\epsilon) f(\epsilon, T) d\epsilon \quad (2.22)$$

where  $\mu$  is the electronic chemical potential (the energy gain/cost of adding or removing one electron). At  $T=0$ ,  $\mu$  corresponds to the Fermi energy ( $\epsilon_F$ ) but for  $T > 0$  the chemical potential differs from  $\epsilon_F$  and has to be calculated in order to accurately compute  $S_{ele}$  at a given  $T$ . Thus to accurately compute  $S_{ele}$  using Equation (2.20) at a given temperature  $T$ , one needs to calculate the respective  $\mu$ . For a solid, one can explore Equation (2.22), since the number of electrons must be kept constant [40].

Given its popular use, it is worth noting that Sommerfeld's approximation allows to simplify the dependence of the entropy on the temperature to a linear relation. In this approximation, it is assumed that  $D(\epsilon)$  varies slowly close to  $\epsilon_F$  (i.e. no peaks in  $D(\epsilon)$  near  $\epsilon_F$ ) and that the temperature is low ( $T \ll \epsilon_F/k_B$ ). When such conditions are met, Equation (2.20) can be simplified to:

$$S_{ele} = \frac{\pi^2}{3} k_B^2 D(\epsilon_F) T. \quad (2.23)$$

While in theoretical studies, there are methods that allow estimating  $D(\epsilon)$ , in experiments it is not possible to determine  $D(\epsilon)$ , and therefore it is not straightforward to determine accurately  $\Delta S_{ele}$  using the definition (Equation (2.20)). In such cases, Sommerfeld's approximation provides a valuable approach for estimating this contribution. This estimation involves conducting linear fits to heat capacity measurements at low temperatures.

## 2.2.2 Lattice Entropy

Similarly, in the context of entropy variation in magnetocaloric materials, we identify various contributions to lattice entropy. Among these contributions is configuration entropy, a term that quantifies the potential arrangements of atoms within a crystal lattice, encompassing both spatial distribution (lattice type) and chemical compositions (commonly referred to as mixing entropy in high-entropy alloys) [41]. This contribution is crucial for phase stability, but since does not depend explicitly on temperature [41], it plays nearly no role in temperature-dependent properties, hence it has a small interest in the context of this work. Yet, another crucial, perhaps the most significant, contribution to lattice entropy is vibrational entropy, denoted as  $S_{vib}$ , which characterizes the dynamic behaviour of atoms. This term has an explicit dependence on the temperature and plays a fundamental role in most temperature-dependent physical properties of solids [42, 41]. As the name suggests,  $S_{vib}$  measures the vibrational degrees of freedom of the atoms in a given structure. In

solid-state physics, vibrations are effectively described using phonons, bosonic quasi-particles that represent the quantization of crystal vibrational modes. To calculate vibrational entropy, one can compute the entropy of phonons. Similarly as for electrons but attending to their bosonic nature, the entropy of phonons is related to the occupation of the respective density of states:

$$S_{vib} = k_B \int_0^\infty g(\omega) \left[ (1 + n(\omega, T)) \ln (1 + n(\omega, T)) - n(\omega, T) \ln (n(\omega, T)) \right] d\omega \quad (2.24)$$

with:

$$n(\epsilon, T) = \left[ \exp\left(\frac{\hbar\omega}{k_B T}\right) - 1 \right]^{-1} \quad (2.25)$$

where  $g(\omega)$  is the vibrational density of states (VDOS) and  $n(\omega, T)$  is the Bose-Einstein distribution (with chemical potential equal to zero)<sup>3</sup>. In the treatment of phonons, a common approximation made is the use of the harmonic model. This model assumes that phonons are independent of each other and independent of other sources of dynamical entropy, being successful at describing low-temperature properties where these conditions are often fulfilled. To consider thermal effects as the volume expansion, the model can be extended in the quasiharmonic model, which assumes independent phonons with altered frequencies [41].

The main challenge of computing  $S_{vib}$  through Equation (2.24) is needed knowledge of VDOS, which can be far from trivial to determine either theoretically or experimentally. The effort required to fully determine VDOS highly motivated the wide use (and misuse) of the Debye model [42]. In the limit  $\mathbf{q} \rightarrow 0$  (long wavelength) a continuum behaviour is achieved, and phonons behave as sound waves, displaying a linear relationship between the frequency,  $\omega$ , and the wave number  $|\mathbf{q}|$  [41]. The constant of such relation is the speed of sound of the medium,  $v_{sound}$ . In the Debye model the behaviour of the  $\mathbf{q} \rightarrow 0$  limit is assumed to all frequencies:

$$\omega = v_{sound} |\mathbf{q}|, \quad |\mathbf{q}| \leq q_D \quad (2.26)$$

till a maximum wave number  $q_D$  (Debye wave number) defined by normalisation conditions of  $g(\omega)$  [42]. As a consequence of this linear relation, we can determine the explicit expression of the vibrational density of states, with a quadratic dependence of  $\omega$ :

$$g(\omega) = \frac{9\hbar^3 \omega^2}{(k_B \Theta_D)^3} \quad (2.27)$$

---

<sup>3</sup>By convention, for phonons, the energy is expressed in angular frequency units according to  $E = \hbar\omega$ .

where  $\Theta_D$  is the Debye temperature, an important parameter of the model, given by [42]:

$$\Theta_D = \frac{\hbar v_{sound}}{k_B} \left( \frac{6\pi^2 N N_A \rho}{M} \right)^{1/3} \quad (2.28)$$

with  $N$  being the number of atoms in the compound/molecule,  $M$  the mass of a mole of the material,  $N_A$  the Avogadro's constant and  $\rho$  the mass density.

It becomes clear then that the Debye model reduces the problem of determining the full phonon spectrum of a material, to the determination of the Debye temperature (or more precisely, the speed of sound) of the material. Moreover, since  $g(\omega)$  has an analytical expression, it allows the creation and exploration of simple models of the thermophysical properties of the materials. If Equation (2.24) is combined with Equation (2.27) the vibrational entropy of the Debye model is given by [43]:

$$S_{vib} = 12N_A k_B \left( \frac{T}{\Theta_D} \right)^3 \int_0^{\Theta_D/T} \frac{x^3}{e^x - 1} dx - 3N_A k_B \ln \left( 1 - e^{-\Theta_D/T} \right). \quad (2.29)$$

The Debye model significantly simplifies the experimental and theoretical characterization of phonons, explaining its widespread use and popularity. Nevertheless, the Debye model has its limitations. The assumption of a linear dispersion ( $\omega(\mathbf{q})$ ) does not work for optical phonons (incoherent vibrations modes) and is inaccurate when  $\mathbf{q}$  approaches a reciprocal lattice vector i.e. when the vibration mode has the wavelength close to the interatomic distances, breaking the picture of a continuum medium. Hence the Debye model is accurate in the limit  $T \rightarrow 0$ , but fails close to  $\Theta_D$ . In the high-temperature limit,  $T \gg \Theta_D$ , the Debye model replicates the asymptotic behaviour expected as the system approaches the classical behaviour.

A source of lattice entropy usually discussed in the context of magnetocaloric materials is the elastic entropy,  $S_{ela}$ , associated with changes in the volume [44, 43]. As discussed before, first-order transitions are accompanied by a discontinuous variation in the volume. If this variation is large enough, we are in the presence of an isostructural transformation, and it might be important to consider the elastic entropy variation [44]:

$$\Delta S_{ela} = \frac{B}{2T} \frac{(\Delta V)^2}{V} \quad (2.30)$$

where  $B$  is the bulk modulus of the material. This entropy contribution is related to the vibrational entropy and can be seen as the entropy associated with changes in the phonon frequencies by variation of the volume, being then a quasi-harmonic correction [41, 43]. This is important to consider when calculating the lattice entropy for two phases, if  $S_{vib}$  already includes the effect of volume change, e.g. by calculating the VDOS of the phases with the respective different volumes, or not. Otherwise, a careless sum of  $\Delta S_{vib}$  and  $\Delta S_{ela}$  can lead to double counting.

### 2.2.3 Magnetic Entropy

The magnetic entropy is expected to be the dominant contribution for the MCE since this effect reflects changes in the magnetic degrees of freedom under the application of a magnetic field. At the atomic scale, the magnetic moment is characterized by the spin magnetic moment, which possesses two degrees of freedom: its magnitude and direction. Perturbations in magnitude are known as longitudinal fluctuations, and can be described by models such as the Stoner model, while the perturbations in the direction are known as transversal fluctuations and can be treated within a simplified Heisenberg model. Typically, longitudinal fluctuations are linked to weakly correlated magnetism, while transversal fluctuations are related to strongly correlated magnetism, such as in the case of  $4f$  orbitals. Transition metals can display both types of fluctuations and ideally, both descriptions should be included for a complete description of such magnetic systems [45]. Yet, when it comes to characterizing properties at finite temperatures, the Stoner model proves to be of limited applicability, at best serving as an adjustment for collective excitations [46]. Furthermore, disentangling the entropy contribution of Stoner fluctuations from the electronic density of states (DOS) is a challenging task. To simplify matters, we can assume that the entropy contribution from longitudinal fluctuations is accounted for within  $S_{ele}$  [28]. As a result, our focus shifts to transversal fluctuations when calculating  $\Delta S_{mag}$ . This choice is motivated by the fact that all the materials that possess a magnetic order have, eventually, an order-disorder transition caused by transversal fluctuations.

Although the spin magnetic moment is of quantum nature by origin, it is often more convenient and intuitive to describe it in a semi-classic picture. An aspect of its quantum nature is that the observable spin projection along a direction (by default the  $z$ -axis), denoted  $m_s$ , is quantized. It spans from  $-s$  to  $+s$  in one-unit increments with  $s$  being the spin quantum number of the particle. Consequently, the projected spin magnetic moment is also discretized as  $g_s m_s \mu_B$ , with  $g_s$  as the spin g-factor ( $\approx 2$ ) and  $\mu_B$  as the Bohr magneton constant. We can interpret the multiplicity of  $m_s$ ,  $2s + 1$ , as the number of possible directions the spin moment can take, as illustrated in Figure 2.4a. In this context, when a system transitions from a fully ordered state, where all spins align in one of these projections, to complete disorder at zero field ( $H = 0$ ), the maximum possible variation in magnetic entropy is [39]:

$$\Delta S_{mag} = Nk_B \ln(2s + 1) \quad (2.31)$$

where  $N$  is the number of independent spins. A quick analysis of Equation (2.31) tells us that  $\Delta S_{mag}$  would be maximized for higher spin moments, with the maximum being reached for  $s = 7/2$  (highest spin quantum number available according to Hund's rule). This explains the high MCE in Gd, and the interest in rare-earths compounds. When accounting for longitudinal fluctuations, the value of  $s$  fluctuates, consequently altering the number of possible projections for  $m_s$ . Thus, the entropy variation would depend on the variations

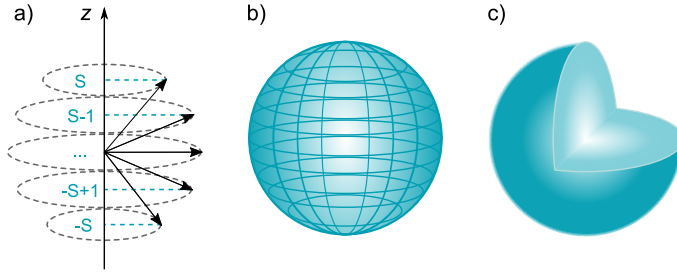


Figure 2.4. Space phase for transversal spin fluctuations in a quantum a) and classic b) description. In c) longitudinal fluctuations are included for the classic description.

in the  $m_s$  multiplicities, resulting in:

$$\Delta S_{mag} = Nk_B \ln \left( \frac{2s_f + 1}{2s_i + 1} \right) \quad (2.32)$$

with  $s_f$  and  $s_i$  being the final and initial spin respectively. Note that the entropy variation in Equation (2.32) is always smaller or equal to the one predicted in Equation (2.31), with the equality being reached when  $s_i$  or (exclusively)  $s_f$  equals to zero.

This quantum description holds at low temperatures, far from the order-disorder magnetic transition. However, it starts to break down at higher temperatures as the fluctuations increase and the energy scale changes. In this regime, a classical description becomes appropriate, as the previously quantized  $m_s$  becomes continuous. The classical estimate for the maximal  $\Delta S_{mag}$  is given by [47]:

$$\Delta S_{mag} = Nk_B \ln(4\pi) . \quad (2.33)$$

This expression refers to the entropy of a spherical surface in the space-phase of the spin moment versor as illustrated in Figure 2.4b. Note that the classic limit does not depend on the magnitude of the magnetic moment, since we only considered changes in the direction of the spin moment. Moreover, this estimate is always higher than in the quantum description, Equation (2.31), since  $s \leq 7/2$ . When considering continuous changes in magnitude, the maximum  $\Delta S_{mag}$  becomes dependent on the spin moment. For instance, if a material undergoes a magnetic phase transition from an ordered state to a fully disordered state with spin moments spanning any value between 0 and the initial spin,  $s$ , the entropy variation can be expressed as:

$$\Delta S_{mag} = Nk_B \ln \left( \frac{4}{3} \pi s^3 \right) . \quad (2.34)$$

This would correspond to a spherical space-phase as illustrated in Figure 2.4c. Note that the dependence on the spin moment magnitude is recovered. For  $s = 7/2$  this scenario corresponds to the maximal magnetic entropy variation that can be achieved.

The approximations discussed above for  $\Delta S_{mag}$  provide valuable insight into how the magnetic subsystem contributes to  $\Delta S$ , but they do not predict the actual  $\Delta S_{mag}$  in the MCE, instead, they can be views as upper limits i.e. the maximal possible value that  $\Delta S_{mag}$  takes. These estimates overlook finite temperature effects and only compare extreme states (fully ordered or fully disordered), leading to an overestimation of entropy variation to the point where it becomes unreasonable. A more accurate form of  $\Delta S_{mag}$  including finite temperature effects can be done by resorting to Monte Carlo simulations and the Heisenberg model to describe fluctuations of the magnetic ordering. The interatomic exchange describes the interactions between localised spin moments and can be expressed as:

$$\mathcal{H} = -\frac{1}{2} \sum_{i \neq j} J_{ij} \mathbf{S}_i \cdot \mathbf{S}_j - \mu_0 \sum_i \mathbf{H} \cdot \mathbf{S}_i \quad (2.35)$$

where  $J_{ij}$  are the exchange parameters,  $\mathbf{S}$  the spin moment vectors, and  $\mathbf{H}$  the magnetic field applied. The exchange parameters  $J_{ij}$  originate from the quantum mechanical properties of electrons, which are indistinguishable fermions. These parameters take positive values for parallel spin alignment (FM interaction) and negative values for anti-parallel spin alignment (AFM interaction). In the Heisenberg Hamiltonian,  $J_{ij}$  quantifies the interactions between spins located on different lattice sites, reflecting the tendency of these spins to either align or oppose each other, depending on the sign and magnitude of  $J_{ij}$  [46].

From the Hamiltonian the internal energy,  $U$ , of the magnetic subsystem can be derived and used to compute  $\Delta S_{mag}$  from the following thermodynamic relations:

$$C_V = \left( \frac{\partial U}{\partial T} \right)_V \quad (2.36)$$

where  $C_V$  is heat capacity at constant volume. This thermodynamic quantity is related to the entropy by:

$$\Delta S_{mag}(T) = \int_0^T \frac{\Delta C_V}{T} dT . \quad (2.37)$$

It is important to stress that the  $\Delta S_{mag}(T)$  calculated in such an approach is slightly different from the one measured experimentally. This is because for simplification, in theoretical calculations the volume is often considered constant, so  $C_V$  is computed, while in experimental conditions pressure is the constant instead, so  $C_P$  is measured. These two quantities should be equal at  $T=0K$  but their difference increases with temperature [41]:

$$C_P - C_V = 9Bv\alpha^2 T \quad (2.38)$$

where  $B$  is the bulk modulus,  $v$  is the specific volume, and  $\alpha$  is the linear coefficient of thermal expansion. The relation above, tells us that for  $T > 0$  the



Equation (2.37) underestimates the magnetic entropy measured experimentally. In practice, other factors, including impurities, defects, and hysteresis - factors not considered in the theoretical model - contribute to the reduction of  $\Delta S_{mag}$ . Consequently, the theoretical  $\Delta S_{mag}$  often exceeds the experimental values.

Note that we used a classic description of the spins in the Heisenberg Hamiltonian, Equation (2.35). A different approach can also be obtained from the quantum description. In a quantum treatment, the magnetic fluctuations behave as spin waves i.e. as collective excitations of the spin subsystems, which propagate as waves. Instead of individual changes in the direction of magnetic moment of the sites, a small perturbation on the magnetic moment direction is propagated. Analogous to phonons, the lattice vibration modes, magnons quantize the spin waves. As phonons, magnons are bosonic quasi-particles and the entropy associated is given by Equation (2.24) but with  $g(E)$  being the magnon density of states (MDOS) instead. While theoretically, this approach is more accurate than the physical treatment, in practice, its use is limited to low temperatures or, more precisely, at temperatures much smaller than the order-disorder transition. This is because, with the increase in temperature, the magnetic fluctuations start to have more of a local nature instead of the collective one described by magnons. In principle, one would only need to calculate a temperature-dependent MDOS to include such behaviour. However, in practice, this is not a straightforward calculation.

### 3. First-principles Calculations

*Give me a CIF file and a DFT code on which to place it, and I shall calculate the crystal properties.*

---

paraphrasing Archimedes

In this chapter, the fundamental ideas behind the methods used for the first-principles calculations performed in this work are briefly described.

#### 3.1 Basics of Density Functional Theory

Density functional theory (DFT) is a very successful and widely used ab-initio method for solving the electronic structure problem using the variational principle. The fundamental basis of the theory was established by Hohenberg and Kohn [48], who proposed that the ground-state properties of a system of many interacting particles could be rewritten as a functional of the charge density  $n(\mathbf{r})$ . In its original formulation, DFT starts from the Born-Oppenheimer approximation, where the nuclei of the atoms are pictured as frozen/fixed. Thus, their kinetic energy can be neglected, the electrostatic interactions between ions are a constant, and the interaction between electrons and ions are equivalent to the electrons moving in an electrostatic field generated by the  $M$  nuclei situated at the sites  $\mathbf{R}_i$  :

$$V_{e-ion}(\mathbf{r}) = \sum_{i=1}^M \frac{eZ_i}{|\mathbf{r} - \mathbf{R}_i|} \quad (3.1)$$

where  $Z_i$  denotes the atomic charge of the ion at site  $i$ . The relevant terms of the Hamiltonian for a system of  $N$  interacting electrons in this field will then be [49]:

$$\mathcal{H} = -\frac{1}{2} \sum_{i=1}^N \nabla_i^2 + \frac{1}{2} \sum_{i \neq j}^N \frac{e^2}{|\mathbf{r}_i - \mathbf{r}_j|} - \sum_{i=1}^N V_{e-ion}(\mathbf{r}_i) . \quad (3.2)$$

The first theorem of Hohenberg and Kohn states that for a system of interacting particles in an external potential  $V_{ext}$ , like e.g.  $V_{e-ion}$ , there is a ground state density,  $n_0(\mathbf{r})$ , which determines uniquely, except for a constant, the Hamiltonian system. In other words, this theorem establishes a mapping between  $n_0$  and the external potential. Once the Hamiltonian is determined, but for a constant shift in potential energy, it follows that the many-body wavefunctions for all states are determined i.e. as corollary of this theorem, we have that all the properties of the system are determined if  $n_0$  is given [49].

As second theorem, Hohenberg and Kohn established the existence of a universal functional of the energy in terms of the charge density, valid for any external potential. This functional is defined in such a way that in principle for a given external potential, the ground state energy is the global minimum of the functional and the density, which minimizes it, is the ground state density  $n_0$ . As corollary, this functional is sufficient to determine the ground state energy and density.

The combination of these two theorems constitutes the logical basis of DFT. Proof of the theorems can be easily found in literature (e.g. Refs. [49, 50]) and it is worth mentioning that there is a more general and abstract formulation of the functional described above, made by Levy and Lieb, which addresses problems related to the functional representability. Their description guarantees an one-to-one mapping between the external potential and  $n_0$ .

It is important to stress that rewriting the many-body problem in terms of the charge density:

$$n(\mathbf{r}) = \sum_{i=1}^N |\phi_i(\mathbf{r})|^2 \quad (3.3)$$

brings a huge numerical simplification of the problem since it reduces a problem of  $3N$  (at the simplest cases) variables to 3 variables. In practice this means the many-body problem is reduced into an effective one-particle description. This is the key feature that allows DFT to treat quantum mechanical systems more efficiently than other methods and made it so attractive and popular for studying the electronic structure.

Although Hohenberg and Kohn proved the existence of a universal energy functional dependent on  $n(\mathbf{r})$ , its analytical form is unknown and a guess of the functional seems equally hopeless as a direct guess of the ground state density and energies. The key problem in writing such functional (and studying the electronic structure in general) is to address the interaction between electrons (2nd term of Equation(3.2)). Since electrons are quantum particles with spin, two new effects arise from the Coulomb interaction - exchange and correlation. While the explicit form of the exchange potential is known for the uniform electron gas under the Hartree-Fock approximation, the same does not apply to correlations in many-body systems.

The development that made DFT a success was proposed by Sham and Kohn [51], who replaced the original many-body problem with an auxiliary independent particle problem, which is assumed to have the same ground state density. In their approach, all the difficulties arising from many-body terms are swept into an exchange-correlation functional of the density:

$$E_{xc}[n] = E_{HK}[n] - T_0[n] - \frac{1}{2} \int \frac{n(\mathbf{r})n(\mathbf{r}')}{|\mathbf{r} - \mathbf{r}'|} d^3r d^3r' - \int V_{ext}(\mathbf{r})n(\mathbf{r})d^3r \quad (3.4)$$

where  $E_{HK}[n]$  is the Hohenberg and Kohn functional,  $T_0[n]$  is the kinetic energy of an effective one-electron system and the latter term is the Hartree en-

ergy. Essentially  $E_{xc}$  is the difference between the interactions and kinetic energies of the true interacting system from those of an auxiliary independent-particle system. The advantage of such approximation is that all unknown/difficult terms of many-body interactions are gathered in one term, which can be approximated as a local (as in the Local Density Approximation - LDA) or nearly local (as in the Generalized Gradient Approximation - GGA) functional [49]. Thus, the auxiliary Kohn-Sham functional  $E_{KS}[n]$  is given by:

$$E_{KS}[n] = T_0[n] + \frac{1}{2} \int \frac{n(\mathbf{r})n(\mathbf{r}')}{|\mathbf{r} - \mathbf{r}'|} d^3r d^3r' + \int V_{ext}(\mathbf{r})n(\mathbf{r})d^3r + E_{xc}[n]. \quad (3.5)$$

Minimizing the functional in Equation(3.5) with respect to the charge density is equivalent to minimising it to the one-particle wave-functions  $\phi_i^*$  gives<sup>1</sup>:

$$\frac{\partial E_{KS}[n]}{\partial \phi_i^*} = 0 \quad (3.6)$$

$$-\frac{\nabla^2}{2}\phi_i + \frac{\partial E_{Hartree}}{\partial n} \frac{\partial n}{\partial \phi_i^*} + \frac{\partial E_{ext}}{\partial n} \frac{\partial n}{\partial \phi_i^*} + \frac{\partial E_{xc}}{\partial n} \frac{\partial n}{\partial \phi_i^*} - \epsilon_i \phi_i = 0$$

$$\left( -\frac{\nabla^2}{2} + V_{Hartree}(\mathbf{r}) + V_{ext}(\mathbf{r}) + V_{xc}(\mathbf{r}) \right) \phi_i - \epsilon_i \phi_i = 0 \quad (3.7)$$

where  $\epsilon_i$  are the Lagrange multipliers for handling the normalization constraints. Equation (3.7) is the well-known Kohn-Sham equation, which can be solved in a self-consistent way to find the groundstate density and the Lagrange multipliers  $\epsilon_i$  also known as the Kohn-Sham eigenvalues. A sketch of a typical DFT cycle is shown in Figure 3.1. Using this approach, the electronic structure can be estimated from first principles with an accuracy determined only by the approximations considered in the exchange-correlation functional.

Since the fundamentals of DFT theory were proposed, there were multiple developments that allowed the extension of the theory beyond its fundamentals as e.g. extension to excited states, time-dependent calculations, spin-polarized calculations and relaxing the Born-Oppenheimer approximation [50]. There are currently a multitude of different DFT-based methods, which differ mainly on the choice of the wave-functions basis and the approximations for the electronic potential. In the work here presented, most of the DFT calculations were made using three distinct methods, the Linear-Muffin-Tin-Orbital, the Korringa-Kohn-Rostoker, and the Projected-Augmented Wave methods, which are briefly introduced in the following sections.

---

<sup>1</sup>In Rydberg atomic units

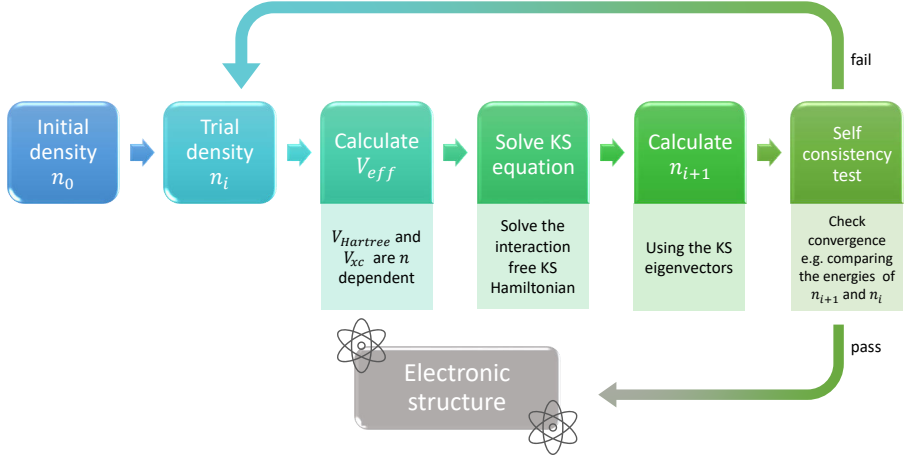


Figure 3.1. Scheme of a typical DFT self-consistent loop.

## 3.2 Linear-Muffin-Tin-Orbitals (LMTO) method

### Muffin-Tin-Orbitals (MTO) method

In the MTO and related methods there is an artificial division of the space into atomic regions, often muffin-tin (MT) or Wigner-Seitz (WS) spheres, and the interstitial space. This division is motivated by the different behaviour of the wave-function within an atomic structure: smooth between atoms, and rapidly varying near the nuclei. Such contrasting behaviour can be better described if the basis is constructed with functions that have alike behaviour. Methods with this spatial division are called augmented.

The MTO method was proposed by Andersen [52], with the goal of providing an accurate electronic structure in terms of a minimal basis. Like in the KKR method (to which, MTO is closely related), the basis is constructed from solutions of the Schrödinger equation inside MT spheres,  $\chi_{lm}^{MT}$ , which are propagated within the interstitial region by envelope functions,  $\chi_{lm}^{Int}$ . In the MTO theory, the former functions (inside the MT) are commonly designated as the heads of the MT orbital while the latter functions (in the interstitial region) are known as tails of the MT orbital. Continuity of the basis functions must be assured at the boundary of the MT spheres between the head functions of the local MT and the tails of the surrounding MTs. This approach results in an energy-dependent basis,  $\chi_{lm}(\epsilon)$ , with Kohn-Sham eigenvalues determined by solving the matching conditions at the MT surfaces. The fundamental difference between these methods is the construction of the envelope functions. In the KKR method,  $\chi_{lm}^{Int}$  must be a solution of the Helmholtz equation [50], which describes the diffusion of spherical wavefunctions with wavenumber  $\kappa$  through the interstitial space. As a consequence, the  $\chi_{lm}^{Int}$  functions are only

properly defined at energies corresponding to the Kohn-Sham eigenvalues. By contrast, in the MTO method, Andersen proposed a set of functions, which depend separately on  $\kappa$  ( $\kappa^2$  referred to as tail energies in the MTO formalism) and  $\epsilon$  [52]. This way, simpler envelope functions can be defined for any energy value obtained and  $\kappa$  can be carefully fixed to obtain a minimal and yet accurate basis for solving the electronic structure [49]:

$$\chi_{lm}(\epsilon, \kappa, \mathbf{r}) = i^l Y_{l,m}(\mathbf{r}) \begin{cases} R_l(\epsilon, r) + \kappa \cot \eta_l(\epsilon) j_l(\kappa r), & r < MT \\ \kappa n_l(\kappa r), & r > MT \end{cases} \quad (3.8)$$

where  $\eta_l$  and  $j_l$ , in the region inside the MT spheres, are spherical Neumann and Bessel functions. For practical reasons in the interstitial region,  $n_l$  function is often constructed using spherical Hankel or Neumann functions (as is the case in the RSPt code [50]).

### Linearization

The key idea of linear methods in DFT is the linearization of non-linear functions around selected reference energies in order to lift the energy dependence of the basis in augmented methods [49] allowing it to be solved numerically more efficiently. Andersen [53] proposed an orbital function  $\Phi_{l,m}$  to be constructed from two augmented functions  $\phi_{l,m}(\epsilon, \mathbf{r})$  and  $\dot{\phi}_{l,m}(\epsilon, \mathbf{r})$  calculated each one at a chosen reference energy  $\epsilon_v$ :

$$\Phi_{l,m}(D, \mathbf{r}) = \phi_{l,m}(\epsilon_v, \mathbf{r}) + \omega(D) \dot{\phi}_{l,m}(\epsilon_v, \mathbf{r}) \quad (3.9)$$

where the factor  $\omega(D)$  assures that the basis function has logarithmic derivative equal to  $D$ . The logarithmic derivative  $D$  is determined by the tails of the surrounding MT and by the local MT heads functions, and can be used to specify the functions of the energy-dependent basis.

The full-potential LMTO method (FP-LMTO) is a highly efficient approach for solving the electronic structure problem in a transparent way, while using as well, an intuitive and correct physical description of the problem. The RSPt (Relativistic Spin Polarized toolkit) [50] is a DFT code based in the FP-LMTO method, which allows for spin-polarized and spin-orbit calculations. The available features implemented, as the exchange parameters calculation, make this code very suitable for solving the electronic structure of the systems of interest for this project. However, being an all-electron method with a site-dependent basis set, it is difficult to implement the evaluation of the linear response and the stress tensor. As a consequence, for structural relaxation of the system and phonon calculations, it is necessary to use another method (and code).

### 3.3 Korringa-Kohn-Rostoker (KKR) method

In its original formulation [54, 55], the KKR method was analogous to the MTO method, sharing the same limitations, such as the use of energy-dependent basis

functions and the need to seek solutions through a secular equation. Despite these challenges, the integration of KKR within scattering theory facilitated a natural transition to Green's functions (GF) formalism.

The KKR approach can be reformulated into a multiple-scattering framework, where electrons are considered to propagate freely between atomic sites, which serve as scattering centres. The Green's function  $G(E, \mathbf{r}, \mathbf{r}')$  represents the propagation of an independent particle with energy  $E$  from point  $\mathbf{r}$  to  $\mathbf{r}'$ .

Instead of employing a variational approach to solve the Kohn-Sham single-particle equation (see Equation (3.7)), the GF formalism modifies the problem to compute the single-particle Green's function  $G(\mathbf{r}, \mathbf{r}', E)$  associated with the Hamiltonian  $\mathcal{H}$ :

$$(E - \mathcal{H}) G(\mathbf{r}, \mathbf{r}', E) = \delta(\mathbf{r} - \mathbf{r}') . \quad (3.10)$$

This Green's function shares eigenfunctions ( $\phi_i$ ) with the Hamiltonian [56], allowing for its expansion in terms of these eigenfunctions:

$$G(\mathbf{r}, \mathbf{r}', E) = \sum_i \frac{\phi_i^*(\mathbf{r})\phi_i(\mathbf{r}')}{E - \epsilon_i} . \quad (3.11)$$

The eigenvalues of  $\mathcal{H}$  emerge as the poles of the GF, illustrating that both the Hamiltonian and its associated Green's function contain equivalent information. So the GF is defined in the poles  $G(\mathbf{r}, \mathbf{r}', \epsilon_i)$ , the domain of  $E$  is extended into the complex plane, approaching the pole through the imaginary component. In the vicinity of a pole  $E + i\delta$  (where  $\delta$  is a positive infinitesimal), the Green's function expands as follows:

$$\begin{aligned} G(\mathbf{r}, \mathbf{r}', E + \delta) &= \mathcal{P} \sum_i \frac{\phi_i^*(\mathbf{r})\phi_i(\mathbf{r}')}{z - \epsilon_i} \\ &\quad - i\pi \sum_i \phi_i^*(\mathbf{r})\phi_i(\mathbf{r}')\delta(E - \epsilon_i) \end{aligned} \quad (3.12)$$

where  $\mathcal{P}$  denotes the Cauchy principal part. The electronic density, a critical aspect of any DFT method, is then defined by:

$$\rho(\mathbf{r}) = -\frac{1}{\pi} \int_C \text{Im} [G(\mathbf{r}, \mathbf{r}, z)] dz . \quad (3.13)$$

While it is evident that density and energy-related quantities can be derived from the single-particle GF, the rationale for preferring this method over the variational approach is not obvious, in particular since generally, GF methods demand more computational effort than variational methods. However, the significant advantage of GF approaches lies in the application of the Dyson equation:

$$\begin{aligned} G(\mathbf{r}, \mathbf{r}', E) &= G_0(\mathbf{r}, \mathbf{r}', E) \\ &\quad + \int G_0(\mathbf{r}, \mathbf{r}'', E)V(\mathbf{r}'')G(\mathbf{r}'', \mathbf{r}', E)d\mathbf{r}'' \end{aligned} \quad (3.14)$$

or in operator notation:

$$\mathbf{G} = \mathbf{G}_0 [1 - \mathbf{V}\mathbf{G}_0]^{-1} . \quad (3.15)$$

This equation links the Green's function of a perturbed system ( $\mathcal{H} = \mathcal{H}_0 + V(\mathbf{r})$ ) with that of a reference system ( $G_0$ ), thereby allowing for the treatment of systems with defects (such as vacancies or impurities) and excited states.

The Spin-Polarized Relativistic KKR (SPR-KKR) [57] is a well-established DFT code that employs the KKR method within the GF formalism. By default, SPR-KKR utilizes the Atomic Sphere Approximation (ASA), wherein the potential is expanded in overlapping spheres. However, the code also supports full-potential calculations. Similar to RSPT, SPR-KKR facilitates the computation of exchange parameters. Both tools share a limitation in structural relaxations due to their reliance on a site-centered basis. The main reason for considering SPR-KKR in this project is its efficiency in handling systems with chemical or/and magnetic disorders. The code's ability to handle such complexities makes it particularly valuable for studying alloys and the properties of the paramagnetic phase.

### 3.4 Projected-Augmented-Wave (PAW) method

Similarly, to the MTO, PAW [58] is also an augmented method with a spacial division of the problem into interstitial and augmentation spheres around the nuclei, although a plane wave (PW) basis is used instead. The use of plane waves simplifies greatly the implementation and numerical effort of the calculations, allowing e.g. to calculate easily the atomic forces. These functions are smooth, thus, ideal to describe the wavefunctions in the interstitial space. However, near the nucleus the wavefunctions oscillate rapidly and the brute force expansion of plane wave functions in this region is unsustainable.

In the PAW method two different sets of basis are used to construct the wavefunctions. A pseudo basis ( $\tilde{\psi}$ ) with plane-wave functions ( $\tilde{\phi}$ ) for the smooth part of the valence wave function, and a basis with all-electron valence functions ( $\psi$ ) that is related to the pseudo-basis for a linear transformation  $\psi = \mathcal{T}\tilde{\psi}$ . The idea is to construct a wavefunction for the whole space as:

$$|\psi_n\rangle = |\tilde{\psi}_n\rangle - \sum_i |\tilde{\phi}_i\rangle \langle \tilde{p}_i | \tilde{\psi}_n \rangle + \sum_i |\phi_i\rangle \langle \tilde{p}_i | \tilde{\psi}_n \rangle \quad (3.16)$$

where  $\tilde{p}_i$  is a projection operator related to the linear transformation  $\mathcal{T}$ . The second term "cuts" the planewave basis from the augmentation sphere while the third term "fills" the spheres with the projection of  $\psi$  in  $\tilde{\psi}$ . As in the previous methods, the continuity in the boundary of the augmentation region must be guaranteed.

Using this construction with localized functions in the augmented spheres allows to retain the nodal structure near the nuclei that PW basis sets fail to



describe. In practice, the localized basis is pre-calculated from frozen-core calculations, and only  $\tilde{\psi}$  has to be solved. The problem then resembles a pseudopotential method (which can be derived formally from [49]) carefully built to preserve the nodal structure of the wavefunctions near the nuclei. The methodology for the PAW method can be viewed as a mixture of the pseudopotential approach and the LMTO method.

VASP is a commercial PAW code [59, 60, 61], widely used in the scientific community for solving the electronic structure. One of the most interesting features is the ability to calculate forces, stress and linear responses. This motivated the choice of using VASP to calculate the atomic forces either for structural relaxation or for computation of the phonons.

### 3.5 Simulating Disorder

The physical properties of systems with chemical or magnetic disorder, such as in alloys or magnetic phases, can be estimated using first-principles calculations with various levels of approximation:

**Virtual Crystal Approximation (VCA)** VCA [62] is a mean-field approach that simplifies chemical disorder as a compositionally weighted average [63]. In an alloy system  $A_xB_{1-x}$ , each site is treated as if it was occupied by a virtual atom  $C$ , whose properties are a weighted average of A and B. For instance, the atomic number of the virtual atom  $Z_C$  is calculated as  $Z_C = xZ_A + (1 - x)Z_B$ . This method can be extended to model an alloy as a mixture of pure crystals, with properties like the phonon spectrum derived as weighted averages from these crystals [64]. VCA's simplicity offers a quick initial estimate of an alloy's properties but is best suited for elements close in the periodic table (e.g., Fe-Co, Co-Ni).

**Coherent Potential Approximation (CPA)** CPA adds complexity to the VCA model by calculating an effective potential that simulates the alloy's electronic properties [65, 66]. In the CPA, often formulated using Green's functions, mixed composition sites are treated within a single-site impurity approximation, i.e. the presence of the impurity atom does not affect the potentials at neighbouring sites. The coherent potential is calculated to average out the scattering caused by impurities, e.g., A and B in  $A_xB_{1-x}$ . This integration leads to an 'effective medium' in which the average scattering effect of the impurities is represented.

The treatment performed in CPA is more suitable for elements with similar atomic sizes and allows for the detailed study of properties of different species in the alloy. It is particularly useful in describing PM configurations within disordered local moment approximations (DLM). In DLM, the magnetic disorder is emulated by considering an alloy  $A_xB_{1-x}$  with A and B belonging to the same atomic species but retaining opposing spin moments.

**Special Quasi-random Structures (SQS)** Unlike VCA and CPA, which describe chemical or magnetic disorder as an isotropic ideal alloy, SQS accounts for local environmental effects. SQS are supercells designed to mimic the correlations in an infinite random alloy [67]. This involves generating various supercells with different occupations for the  $A_xB_{1-x}$  sites. Then, the atomic arrangements on the different configurations are discretized into clusters of order  $k$  ( $k=2$  being pairs of atoms,  $k = 3$  being trios,...) and coordination shell  $m$ . The correlations  $\Pi_{mk}$ , calculated as products of a 'spin' variable identifying the species (e.g. 1 for A, -1 for B), are averaged. For a fully random alloy, these averages are determined as  $\Pi_{m,k}^- = (2x - 1)^k$ , and the aim of the SQS approach is then to generate supercells with correlations matching these target correlations. The more cluster ( $mk$ ) types included, the more accurate the description of a random alloy is, but at a higher computational cost. Thus a balance, in function of the physical property of interest, must be made in the expansion of the clusters. For instance, in studying magnetic properties within the Heisenberg model, pair clusters might suffice, as the model focuses on pair interactions. Unlike the previous methods, the SQS approach is not limited by the difference in the chemical properties of the elements alloyed.

These methods vary in their detail and computational demands, with SQS being the most comprehensive but also the most resource-intensive. Generating and evaluating a representative SQS, although facilitated by tools like `mcqs` [68], can be time-consuming. CPA is often limited to Green function-based methods like KKR. VCA is the most versatile option, simplicity allows for easy implementation and revision [63]. In general, both VCA and CPA are capable of reproducing experimental trends for alloying effects being comparable with the results from SQS [69, 70] for alloying elements close in the periodic table.

In the present work, these approaches are applied in various contexts. SQS was used in Paper III to investigate the formation of local environments during structural relaxation. CPA, implemented with the SPR-KKR code, was applied in Papers II and IV to describe disordered local magnetic moments and in Paper III to calculate the magnetic properties of alloyed compounds.

### 3.6 DFT+U

DFT is a mean-field theory, which is very adequate to describe the "sea of electrons" from metallic bonding. However, some  $d$  and most  $f$  transition metals present strongly correlated electrons which cannot be successfully described in standard DFT methods since they require a more localized description of the states. The DFT plus interaction term  $U$  (DFT+U or LSDA+U/GGA+U according to the exchange-correlation potential) approach is an "on top of DFT" modification which allows to treatment of strongly correlated materials. To describe localized  $d$  and  $f$  states an additional repulsion term  $U$  describing an

intra-atomic Hubbard interaction is included in the Coulomb interaction. This term drives correlated orbital occupation numbers ( $n_i$ ) to integer values 0 or 1 [71]. In a simple version of DFT+U method, the shift on the DFT eigenvalues is [72]:

$$\epsilon_i = e_i^{DFT} + U\left(\frac{1}{2} - n_i\right) \quad (3.17)$$

that is, more than half-filled bands are shifted down in energy, while less than half-filled bands are shifted up. The addition of a Hubbard  $U$  interaction also introduces the need for "double counting" correction terms in the energy functional since the Coulomb energy was already included in the functional. This means that the DFT+U method is sensitive to the choice of the double-counting term.

## 3.7 Applications

### 3.7.1 Phonon Calculations

The study of lattice dynamics of crystals can be simplified by focusing on the movement of the nuclei, as they contain the majority of an atom's mass [41]. This approach is in line with the Born-Oppenheimer approximation, which effectively decouples the energy of the electronic system from the kinetic energy of the nuclei. As a result, the equations of motion for the nuclei are predominantly determined by their positions, denoted as  $\mathbf{R}$ , the electrostatic interactions between nuclei and the total energy  $E(\mathbf{R})$  of the electronic system for the respective nuclear configuration. In this context, a general Hamiltonian for the nuclei can be formulated to capture these dynamics:

$$H_n = \sum_{jl} \frac{\mathbf{p}_{jl}^2}{2m_j} + \phi(\mathbf{R}) \quad (3.18)$$

with characteristics of the atom vibrations determined by the potential energy  $\phi$ . Expanding  $\phi(\mathbf{R})$  in respect of the atomic displacement  $\mathbf{u}_{jl} = \mathbf{R}_{jl}^0 - \mathbf{R}_{jl}$  where  $\mathbf{R}_{jl}^0$  are the equilibrium positions of the atoms,  $j, j'$  is the index of the atom in the unit cell, and  $l, l'$  is the index of the unit cell. For convenience, the displacement vector  $\mathbf{u}_{jl}$  is expressed in Cartesian coordinates with its components expressed by the  $\alpha, \beta$  indices.

$$\begin{aligned} \phi(\mathbf{u}) = & \phi_0 + \sum_{\alpha jl} \left( \frac{\partial \phi}{\partial u_{\alpha jl}} \right)_0 u_{\alpha jl} \\ & + \frac{1}{2} \sum_{\alpha jl} \sum_{\alpha' j' l'} \left( \frac{\partial^2 \phi}{\partial u_{\alpha jl} \partial u_{\alpha' j' l'}} \right)_0 u_{\alpha jl} u_{\alpha' j' l'} + \dots \end{aligned} \quad (3.19)$$

The first derivative of the total energy with respect to the nuclei corresponds to the forces and the second derivative to the second-order force constants  $\Phi_{\alpha\beta}(jl, j'l')u_{\alpha jl}$ . In equilibrium, the forces acting on any atom must vanish [41]:

$$\left( \frac{\partial \phi}{\partial u_{\alpha jl}} \right)_0 = 0. \quad (3.20)$$

Including the expanded  $\phi$  in Equation (3.18):

$$H_n = \sum_{jl} \frac{\mathbf{p}_{jl}^2}{2m_j} + \phi_0 + \frac{1}{2} \sum_{\beta jl} \sum_{\alpha' j'l'} \Phi_{\alpha\beta}(jl, j'l') u_{\alpha jl} u_{\beta j'l'}. \quad (3.21)$$

This Hamiltonian defines the equations of motion, which correspond to Newton's second law. To solve this system, an ansatz with the form of plane waves with wavevector  $\mathbf{q}$  and angular frequency  $\omega$  can be used [73]:

$$u_{\alpha}(jl, t) = \frac{1}{\sqrt{m_j}} \sum_{\mathbf{q}} U_{\alpha}(j, \mathbf{q}) \exp(i[\mathbf{q} \cdot \mathbf{R}_{jl}^0 - \omega t]). \quad (3.22)$$

Replacing this ansatz in the equation of motion, the dynamics of the system are reduced to an eigenvalue problem:

$$\omega^2 U_{\alpha}(j, \mathbf{q}) = \sum_{j'\beta} D_{\alpha\beta}(jj', \mathbf{q}) U_{\beta}(j', \mathbf{q}) \quad (3.23)$$

where  $D_{\alpha\beta}$  is the dynamic matrix:

$$D_{\alpha\beta}(jj', \mathbf{q}) = \frac{1}{\sqrt{m_j m_{j'}}} \sum_{l'} \Phi_{\alpha\beta}(jl, j'l') \exp(i\mathbf{q} \cdot [\mathbf{R}^0(j'l') - \mathbf{R}^0(jl)]). \quad (3.24)$$

The eigenvectors of the dynamical matrix correspond to the normal modes of vibration, and the respective eigenvalues correspond to the squared phonon frequencies.

To calculate phonons from first-principles, usually the finite displacement method is used. In this method, one or more atoms are shifted by finite displacements  $\Delta \mathbf{r}_{jl}$  from their equilibrium positions. This shift induces variations in the forces between atoms ( $\mathbf{F}(jl)$ ) that are approximated to the force constants[74]:

$$\Phi_{\alpha\beta}(jl, j'l') \simeq - \frac{F_{\beta}(j'l'; \Delta r_{\alpha}(jl)) - F_{\beta}(j'l')}{\Delta r_{\alpha}(jl)}. \quad (3.25)$$

As suggested by the sum over the unit cells in equation (3.24), it is generally necessary to calculate the forces in a large supercell to include all meaningful contributions. A rule of thumb is to observe whether the forces calculated on the atoms further away from the displaced ones are small enough. In the work discussed in this thesis, the calculations of phonons were performed with the Phonopy package [74] as an auxiliary tool for post-processing the forces calculated in DFT and calculating the phonon spectra and density of states.

### 3.7.2 Elastic Properties

Full phonon calculations provide a comprehensive description of the vibrational properties at  $T = 0\text{K}$ . However, they are resource-intensive, which makes them impractical for large structures. Furthermore, for compounds undergoing structural transitions, the high-temperature phase often exhibits dynamic instability, manifested as imaginary phonon modes corresponding to a static distortion that minimizes the system's energy. In these scenarios, the Debye model emerges as a suitable alternative for describing vibrational properties, with parameters such as sound velocity  $v_{\text{sound}}$  (see Equation (2.28)) derived from the elasticity constants.

Hooke's law establishes a relationship between an applied force, the elastic strain tensor ( $\delta$ ) and the system's response, the stress tensor ( $\sigma$ ) [42]:

$$\sigma_i = \sum_{j=1}^6 c_{ij} \xi_j \delta_j . \quad (3.26)$$

Here, the Voigt notation was used for the components of the tensor<sup>2</sup>, and  $\xi_i$  is a factor to account for the symmetry of the  $\delta$  tensor:

$$\xi_i = \begin{cases} 1 & \text{for } i = 1, 2, 3 \\ 2 & \text{for } i = 4, 5, 6 \end{cases} . \quad (3.27)$$

The constants  $c_{ij}$  represent the elastic stiffness or second-order elastic constants. Due to their symmetry,  $c_{ij} = c_{ji}$ , 21 independent constants exist, which are reduced further based on structural symmetry [42]:

- Cubic (3 constants):  $c_{11}, c_{12}, c_{44}$
- Hexagonal (5 constants):  $c_{11}, c_{12}, c_{13}, c_{33}, c_{44}$
- Orthorhombic (9 constants):  $c_{11}, c_{12}, c_{13}, c_{22}, c_{23}, c_{33}, c_{44}, c_{55}, c_{66}$

The constants  $c_{ij}$  are linked to the slopes of long-wavelength acoustic phonon branches ( $\mathbf{q} \rightarrow 0$ ), thus associating with sound wave velocities in various modes (transversal or longitudinal) along certain directions [42].

In polycrystalline samples, comprising multiple single crystals oriented in different directions, these samples exhibit statistical isotropy and homogeneity, making  $c_{ij}$  less effective as elastic descriptors. Alternatively, the polycrystalline bulk modulus  $B$  and shear modulus  $G$  are more appropriate, representing the average elastic properties of an isotropic assembly of single crystals [75]. Commonly used averaging methods include Voigt (isostress), Reuss (isostrain), and Hill (an average of Voigt and Reuss).

The average sound velocity can be approximated from these moduli [76]:

$$v_{\text{sound}} = \sqrt{\rho} \left( \frac{1}{3} \left[ \frac{2}{G^{3/2}} + \frac{1}{(B + \frac{4}{3}G)^{3/2}} \right] \right)^{-1/3} \quad (3.28)$$

<sup>2</sup>1, 2, 3, 4, 5, and 6 correspond to xx, yy, zz, yz, xz, and xy, respectively.

where  $\rho$  is the density of the materials (volumetric mass).

The internal energy  $E$  of a crystal under strain  $\delta$  can be expanded using the Taylor series in terms of the strain tensor, relative to the initial energy of an unstrained crystal. Considering the relations

$$\sigma_i = \frac{1}{V_0} \frac{\partial E}{\partial \delta_i} \quad (3.29)$$

$$c_{ij} = \frac{\partial \sigma_i}{\partial \delta_j} = \frac{1}{V_0} \frac{\partial^2 E}{\partial \delta_i \partial \delta_j} \quad (3.30)$$

the harmonic approximation (2nd order) of the Taylor expansion is given as [75]:

$$E(V, \delta) = E_0 + V_0 \left( \sum_i \sigma_i \xi_i \delta_i \right) + \frac{1}{2} \sum_{ij} c_{ij} \delta_i \xi_i \delta_j \sigma . \quad (3.31)$$

Reference [75] details the process to determine  $c_{ij}$  from first principles calculations, by fitting DFT energies for various strains  $\delta$  in Equation (3.31). Different distortions are needed to calculate distinct  $c_{ij}$  values. Small, volume-conserving strains are preferable for accuracy, except when determining  $c_{11}$ ,  $c_{22}$ , and  $c_{33}$ <sup>3</sup>. Once the independent stiffness constants are determined, the full matrix  $c$  can be constructed, and the elastic stiffness matrix  $s$  is calculated as  $s = c^{-1}$ . With  $s$  and  $c$ , the bulk and shear moduli are obtainable, allowing for first-principles determination of  $v_{\text{sound}}$ .

### 3.7.3 Exchange Parameters ( $J_{ij}$ )

The Heisenberg Hamiltonian (Equation (2.35)) is often a starting point to describe magnetic subsystems. However, a first-principles estimate of the  $J_{ij}$  can be troublesome since the magnitude of these parameters is relatively small, around 1 or 2 mRy in strong couplings, requiring an additional effort in the accuracy of the calculations. From DFT, the parameters can be estimated from total energy variation for small deviations of some magnetic moments relative to the magnetic ground state [77]. This can be done using the so-called frozen-magnons approach, or using the more mathematically involved approach suggested by Liechtenstein-Katnelson-Antropov-Gubanov (LKAG) [78]. In the latter, a rigorous approach for calculating the  $J_{ij}$  is formulated within DFT approach (more exactly using Local Spin Density Functional Theory) using KKR Green functions formalism. The key idea of this approach is to calculate the pair interaction  $J_{ij}$  from the energy variation caused by small rotations ( $\theta \rightarrow 0$ ) on opposite angles  $\pm\theta/2$  of two spin moments at sites  $i$  and  $j$  [78]:

$$J_{ij} \approx 2 \frac{\delta E_{ij} - \delta E_i - \delta E_j}{\theta^2} \quad (3.32)$$

as illustrated in Figure 3.2.

<sup>3</sup>Such volume-conserving distortions would require more than one strain to be applied

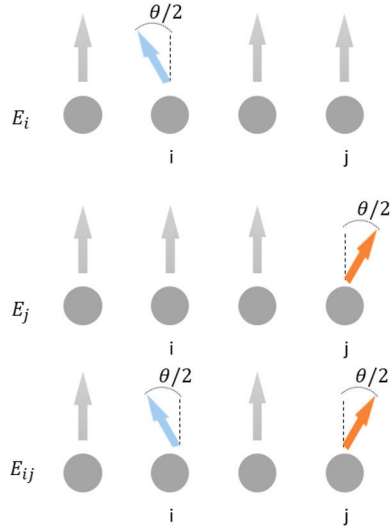


Figure 3.2. Illustration of the spin moments rotation considered in the LKAG approach.

For small enough angles, the magnetic force theorem should be valid, and the problem can be simplified to the computation of perturbations instead of calculating total energy variation. The LKAG method describes this perturbation in the multiple scattering formalism leading to an expression for the exchange parameters [77]:

$$J_{ij} = -\frac{2}{\pi} \int \text{Im} \left\{ \text{Tr}_L \left\{ \Delta_i G_{ij}^\uparrow \Delta_j G_{ji}^\downarrow \right\} \right\} d\epsilon \quad (3.33)$$

where  $G_{ij}^{\downarrow/\uparrow}$  are the Green's functions that operate the small  $\theta$  rotation, and  $\Delta$  is the exchange spin splitting matrix. In this formulation, the exchange parameter is determined by the inter-atomic interactions between sites with the  $J_{ij}$  parameters depending on  $\Delta$  in a more complex way than in the Stoner model, which is closely related to the intra-atomic exchange interaction.

In the RSPt code, the LKAG method is implemented as described in Ref. [79], with  $\Delta$  calculated, for pure DFT calculations, as the difference between spin, and site projected Kohn-Sham Hamiltonian. In SPR-KKR the LKAG method is also implemented for the calculation of  $J_{ij}$ .

# 4. Magnetic Monte Carlo Simulations

*Mix it all together and you know that it's the best of both worlds*

---

Hannah Montana's "Best Of Both Worlds"

This chapter describes the Monte Carlo method employed in the magnetic simulations to determine the magnetic entropy and magnetic ordering temperature. Additionally, it offers a more detailed explanation of the rescaling scheme introduced in Paper II, providing context and detailed insights into its application.

## 4.1 Metropolis Monte Carlo

For most realistic systems, the exact analytical solution of the Heisenberg Hamiltonian is unknown and remains a significant challenge, particularly to determine magnetic properties at finite temperatures since it requires the evaluation of the partition function and expectation values, which becomes impractical for problems with many degrees of freedom. Monte Carlo (MC) techniques offer a powerful alternative in this context [80]. These encompass a class of methods used for randomly selecting a set of representative states, i.e. sampling, from a larger distribution. By taking a large number of samples, MC methods can estimate probabilities and expectation values (averages), thereby providing a practical solution for calculating equilibrium properties in systems where direct analytical approaches are not feasible.

Typically, MC simulations involve state sampling supported by a distribution that determines the acceptance probability, which varies based on the chosen sampling method. Within statistical physics, the Metropolis algorithm [81] employs the Boltzmann distribution for sampling, making it suitable for classical physics problems. For the magnetic simulations described in this thesis, the algorithm functions as follows [82]:



1. Initialize the magnetic configuration.
2. Randomly propose a new trial configuration by altering the direction of magnetic moments at one or more sites within the simulation box.
3. Compute the energy of the trial configuration.
4. Accept the new configuration if it reduces the system's energy ( $\Delta E \leq 0$ ). If  $\Delta E > 0$ , the new configuration is accepted with a certain probability  $W$  given by:

$$W = \begin{cases} \exp\left(-\frac{\Delta E}{k_B T}\right) & , \text{ if } \Delta E > 0 \\ 1 & , \text{ otherwise} \end{cases} \quad (4.1)$$

5. Repeat steps 2 to 4, constituting a MC step, until convergence of certain quantity, e.g. the  $\langle E \rangle$  or other stop criteria are met. Often the number of MC steps is considered.

The Metropolis algorithm has proven to be effective in solving the Heisenberg Hamiltonian and accurately calculating equilibrium properties such as magnetization [83, 84, 80], heat capacity, magnetic susceptibility, and other thermal averages. It is also popularly employed to predict magnetic transition temperatures for  $J_{ij}$  values derived ab-initio calculations. However, its performance diminishes at low temperatures where quantum effects dominate, and the Boltzmann distribution becomes invalid. This limitation manifests in a faster variation in comparison with measurements of the temperature-dependent magnetization curves at low temperatures (see Figure 4.1), due to the treatment of the energy spectrum as continuous. Additionally, the calculated  $\lim_{T \rightarrow 0} C_{mag} = k_B$  for bulk systems contradicts the third law of thermodynamics' expectation of  $\lim_{T \rightarrow 0} C_{mag} \rightarrow 0$ .

## 4.2 Quantum Rescaled Monte Carlo

At low temperatures, magnetic fluctuations are predominantly governed by magnons that adhere to the Bose-Einstein distribution. Although current quantum Monte Carlo methods can accurately describe the quantum Heisenberg Hamiltonian, they are computationally intensive and thus limited to simpler problems [83, 84]. For more complex systems, more practical approaches have been proposed, involving rescaling conventional Monte Carlo simulations to mimic quantum behaviour at low temperatures [84, 83, 86]. The approach proposed in parallel by Woo C.H. et al [86] and Evans R.F.L et al [83] are particularly interesting for its simple implementation as it only involves adjusting the temperature within the Metropolis algorithm. This rescaling of the temperature can be done using semi-empirical parameters along with a phenomenological model [83], or using a theoretical approach based on the Bose-Einstein distribution [86]. In this work, the latter is chosen, as it has fewer free parameters.

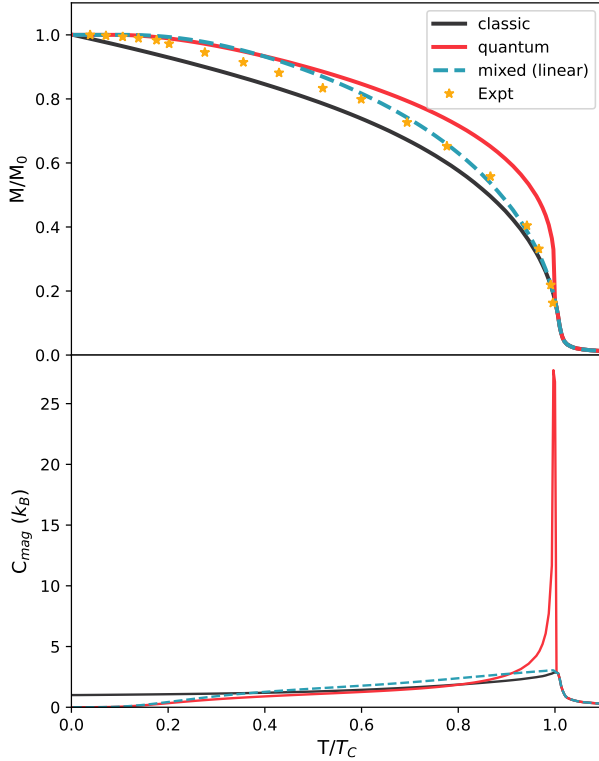


Figure 4.1. Comparison of the mixed ( $\alpha$  as a linear function) rescaling of the reduced magnetization and magnetic heat capacity with the quantum rescaling and the conventional curves from the (classic) Boltzmann distribution. Experimental data from Ref. [85].

The Boltzmann distribution, characterized by the factor  $\beta_{\text{classic}} = (k_B T)^{-1}$ , sets an energy scale for variations in energy (see Equation (4.1)). In Ref. [86] a quantum equivalent,  $\beta_{\text{quantum}}$ , derived from the Bose-Einstein distribution is introduced as follows:

$$\beta_{\text{quantum}} = \left[ \int_0^\infty g(E, T) \frac{E}{\exp(E/k_B T) - 1} dE \right]^{-1}. \quad (4.2)$$

Here,  $g(E, T)$  represents the magnon density of states (MDOS). By equating  $\beta_{\text{quantum}}$  with  $\beta_{\text{classic}}$ , this model effectively redefines temperature, introducing a quantum temperature,  $T_{\text{quantum}}$ , calculated as  $T_{\text{quantum}} = [k_B \beta_{\text{quantum}}(T_{\text{classic}})]^{-1}$ . Note that  $\beta_{\text{quantum}}^{-1}$  is equivalent to the average magnon energy at a given temperature, which is intuitively

consistent with the average energy  $k_B T$  in a classic system (equipartition theorem).

This approach promises an accurate description of the system's statistics across the whole temperature range, unlike conventional Monte Carlo methods. However, deriving MDOS at finite temperatures from first principles, especially near magnetic-ordering temperatures, remains challenging [80]. Thus for a practical application of quantum rescaling, a simpler approach must be made to determine  $g(E, T)$ . In Ref. [86] a magnon quasi-harmonic approximation (MQHA) is proposed in order to include the softening of the magnon modes due to anharmonic effects. Thus, this MQHA approach can be applied to the adiabatic MDOS, in order to extend it to finite temperatures according to [80]:

$$E_c(T) = E_c(0) \left(1 - \frac{T}{T_C}\right)^{\beta_c} \quad (4.3)$$

where  $E_c$  is the cut-off energy of MDOS, i.e. the highest energy with a finite contribution to the MDOS,  $T_C$  the magnetic ordering temperature, and  $\beta_c$  which is the critical exponent associated with the magnetization (in the calculations presented here  $\beta_c=0.365$  was considered as in Ref. [80]). As illustrated in Figure 4.2, this approach is a shape-conserving rescaling of MDOS [80, 86]. In the limit  $T \rightarrow T_C$ , MDOS approaches a singularity with all magnon modes with the same energy, aligning with a classic statistic which is insensitive to the frequency distribution [86].

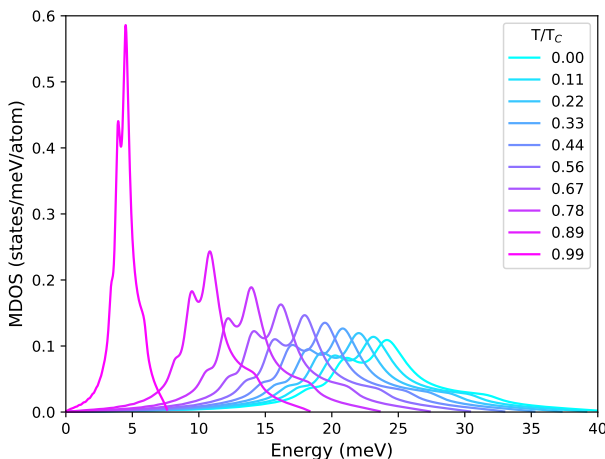


*Figure 4.2.* Softening of the bulk hcp Gd adiabatic magnon density of states under the shape-conserving magnon quasi-harmonic approximation (as indicated in the text) for different temperatures. Data from Gd calculations performed for Paper II.

By combining Equations (4.2) and (4.3), we can compute the rescaled temperature,  $T_{rescaled}$ , which allows the Boltzmann distribution to replicate the

thermodynamic averages of the Bose-Einstein distribution. As shown in Figure 4.3,  $T_{rescaled}$  is consistently lower than its classical counterpart. This temperature rescaling significantly improves system descriptions at low temperatures, as is evident from the comparison to the experiment in Figure 4.1. Note that for the simple Heisenberg Hamiltonian, see Equation (2.35), the equilibrium magnetization should be a state function of the temperature. Thus no additional calculations are necessary in order to apply this temperature rescaling to the results of the MC simulations, offering a very practical on-top correction.

Nonetheless, near the magnetic transition temperature, this scheme diverges from experimental results, and conventional Monte Carlo simulations perform better. The limitations of this approach near  $T_C$  arise partly from the simplistic MQHA used, which causes a discontinuous temperature change at  $T_C$  between  $\beta_{quantum}$  and  $\beta_{classic}$ , artificially sharpening the magnetic transition.

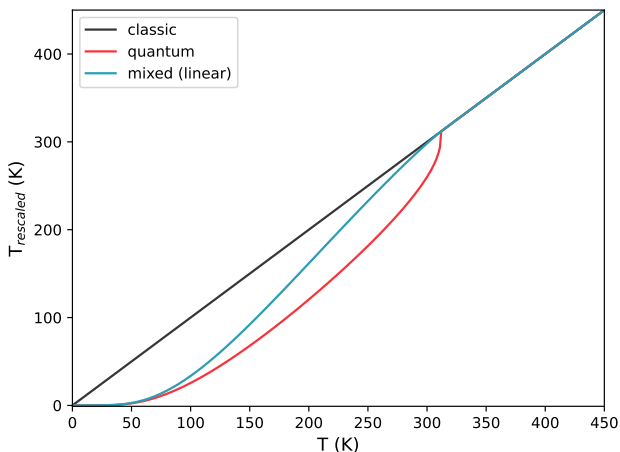


Figure 4.3. Rescaled temperature used internally in the MC simulations as a function of the input temperature for different recalling schemes. Data from Gd calculations performed for Paper II.

### 4.3 Mixed Rescalling

In Paper II, a novel scheme has been proposed to avoid this discontinuous change by interpolating between  $\beta_{quantum}$  and  $\beta_{classic}$ . Instead of sampling the statistic distribution of the system with a classic or a 'quantum' Boltzmann distribution, it was proposed to consider their mixture, with the transition probability between MC steps then given by:

$$W_{mixed} = \alpha \exp(\beta_{classic} \Delta E) + (1 - \alpha) \exp(\beta_{quantum} \Delta E) \quad (4.4)$$

here  $0 < \alpha < 1$  is a weight factor that balances the classic and quantum contributions. Physically this distribution can be interpreted as describing the co-existence of local fluctuations (spin-flip like), described by classic statistics, and non-local fluctuations, described by the magnons with quantum statistics. Within this interpretation it is clear that  $\alpha$  must be chosen so its temperature dependence ensures that the quantum effects dominate at low temperatures, while classic statistics becomes more significant near the critical temperature  $T_C$ . With this in consideration,  $\alpha(T)$  is defined as linear function of temperature in Paper II, to avoid abrupt transitions between the two statistical regimes:

$$\alpha(T) = \begin{cases} \frac{T}{T_C} & , T \leq T_C \\ 1 & , T \geq T_C \end{cases} . \quad (4.5)$$

For convenience and easier interpretation Equation (4.4) can be rewritten using the conventional Boltzmann distribution:

$$W_{mixed} = \exp(\beta_{mixed}\Delta E) \quad (4.6)$$

where the scaling term  $\beta_{mixed}$  is defined by:

$$\beta_{mixed} = \frac{\ln [\alpha \exp(\beta_{classic}\Delta E) + (1 - \alpha) \exp(\beta_{quantum}\Delta E)]}{\Delta E} . \quad (4.7)$$

Notably, Equation (4.7) shows a dependence of the scaling factor on the energy difference between MC steps, not allowing for an intuitive guess of its magnitude. However, at thermal equilibrium, the system fluctuates around the average energy,  $\langle E \rangle$ , and thus the average energy difference between the trial configurations tends to approach zero. In this limit, Equation (4.7) simplifies to:

$$\lim_{\langle \Delta E \rangle \rightarrow 0} \beta_{mixed} = \alpha \beta_{classic} + (1 - \alpha) \beta_{quantum} \quad (4.8)$$

or in a more convenient form:

$$T_{mixed} = \frac{T_{quantum} T_{classic}}{\alpha T_{quantum} + (1 - \alpha) T_{classic}} . \quad (4.9)$$

This formulation allows for a clearer understanding of the temperature used in rescaling. As for the previous quantum scheme,  $T_{mixed}$  can be used as an on-top correction to the conventional MC simulations. The application of this rescaling scheme, has the benefits of both the quantum and the classic statistics, being able to describe correctly both limits  $T \rightarrow 0$  and  $T \rightarrow T_C$ , see Figure 4.1. Moreover, the scheme improves the description in the intermediate temperature range, closing the gap between the experimental data [85] and the calculated temperature-dependent magnetization for Gd.

## Other Mixing Functions

The linear choice for  $\alpha$  offers simplicity and a solid starting point for interpolation without presupposing specific physical behaviours. However, other functional forms for  $\alpha$  that meet the requisite conditions are also worth considering. In order to explore how the mixed rescaling reacts for different choices of  $\alpha$ , two common relations in physics were considered: a logistic function, and a generalization of (4.5) to a power law.

The logistic function  $f(T)$  was parametrized so the following conditions were respected to suffice the requirements of  $\alpha$ :

$$\begin{aligned} f(T_C) &= 1 - \text{tol} \\ f(0) &= \text{tol} \end{aligned} \quad (4.10)$$

with 'tol' represents a numerical tolerance (set to  $10^{-6}$  for these calculations), to handle the asymptotic behaviour of the logistic function. Within these conditions  $\alpha$  is defined as:

$$\alpha = \frac{1}{1 + \exp \left[ -2 \ln \left( \frac{1}{\text{tol}} - 1 \right) \left( \frac{T}{T_C} - \frac{1}{2} \right) \right]} . \quad (4.11)$$

This logistic blending leads to a distinct kink in the rescaled magnetization, indicative of a rapid transition from quantum to classic regimes (Figure 4.4). This abrupt transition also results in an unphysical peak in the heat capacity, indicating that the logistic function is not an ideal choice for the mixing factor.

The power law version of  $\alpha$ , introduced in Paper II, generalizes the linear relation:

$$\alpha = \begin{cases} \left( \frac{T}{T_C} \right)^\gamma & , T \leq T_C \\ 1 & , T \geq T_C \end{cases} . \quad (4.12)$$

Here, the exponent  $\gamma$  (satisfying  $\gamma > 0$ ) dictates the curvature of the  $T_{mixed}$ . It can serve as an adjustable parameter, offering flexibility in fitting the data. For instance, when fitting the simulated magnetization curves to experimental data [85] for bulk Gd, a  $\gamma$  value of 0.549 was determined. Interestingly, the magnetization curve corresponding to this  $\gamma$  value shows a small deviation from that derived from a linear mixing, as illustrated in Figure 4.5. This observation lends support to the choice of a linear  $\alpha$  as a robust initial assumption. Nonetheless, to solidify this conclusion, additional investigations across diverse systems are necessary.

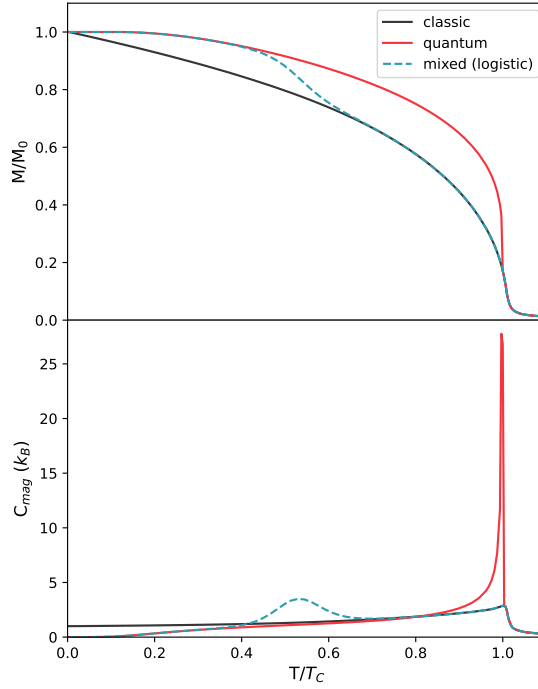


Figure 4.4. Comparison of the mixed ( $\alpha$  as a logistic function) rescaling of the reduced magnetization and magnetic heat capacity with the quantum rescaling and the conventional curves from the (classic) Boltzmann distribution.

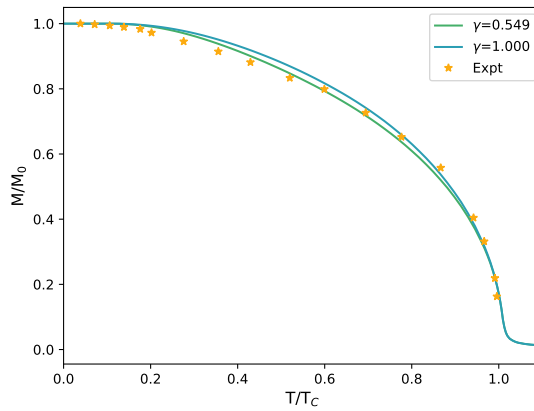


Figure 4.5. Comparison of the mixed ( $\alpha$  as a power function) rescaling of the reduced magnetization for  $\gamma=1$  (linear mixing) and the  $\gamma$  fitted against the experimental data[85].

## 4.4 Remarks and Outlook

The mixed rescaling proposed in Paper II offers a quick and parameter-free approach to model the temperature-dependent magnetization curves obtained in conventional magnetic Monte Carlo simulation in order to describe correctly simultaneously low temperatures and the classic statistic close to the magnetic ordering temperature. For the moment the choice of mixing function is not backed by a physical explanation, and as shown for the  $(T/T_C)^\gamma$  power law case it can be used as a fitting parameter.

Conceptually, this scheme can be seen as a correction to the magnon quasiharmonic approximation in order to estimate the temperature-dependent MDOS. In principle, if the exact MDOS(T) was known, the quantum rescaling proposed in Ref. [86] would be sufficient to calculate the magnetic behaviour in the whole temperature  $[0-T_C]$  range. With this in mind, it would be interesting to explore the behaviour of the mixing function in several different magnetic systems and find a phenomenological model to describe universally the temperature evolution of the MDOS, in a similar way as was done by Ref. [87] for the magnetization.

Moreover, it would also be interesting to extend this scheme to atomistic spin dynamics (ASD) calculations to investigate if it is capable of improving such calculation for temperatures far from the low-temperature limit and from the magnetic ordering temperature.



## 5. Benchmarking Entropy Calculations

*If you know the enemy and know yourself,  
you need not fear the results of hundred battles.*

---

Sun Tzu, 'The Art of War'

The theoretical background for the entropy calculations has been laid out in previous sections, including, some approximations for  $S_{lat}$ , the Debye Model, and  $S_{ele}$ , the Sommerfeld's approximation. These approximations simplify the calculation of the entropy contribution, which is of interest for calculations on a large scale. However, it is important to first evaluate their performance in describing  $\Delta S$  in the context of the MCE. Moreover, since DFT is a groundstate theory, by using it to calculate physical parameters, we are blind to fluctuations such as the ones from finite temperature effects. Does this have a meaningful impact on calculating  $\Delta S$ ?

Phase transitions often have intermediate stages. Is it reasonable to only consider the initial and final states?

This chapter summarises the results of benchmarking studies for  $\Delta S$  calculation to explore the effect of commonly used approximations. The benchmark tests were made for two systems, FeRh and Gd, well-known magnetocalorics, to cover the aspects of the different nature of the transition (1st and 2nd order, respectively).

### 5.1 FeRh

The main aim of this project was to test the performance of well-known methods for the entropy estimation of the electronic, lattice, and magnetic subsystems while discussing their applicability in a high-throughput scheme, in which the balance between accuracy and the computational effort is a key point. To benchmark the different approximations, the metamagnetic AFM→FM transition of FeRh was considered as a test case for the entropy estimations. This material is a well-known magnetocaloric with broad and detailed information available in the literature, which is convenient for comparison of results. Also, FeRh has a simple crystalline structure (CsCl) that eases the computational effort required and allows for a careful treatment of its complex behaviour.

In literature, the Debye model is commonly used as an approximation to estimate the vibrational entropy, which motivates a detailed discussion about the advantages and limitations of this model. Conveniently, the Debye model avoids the need to calculate cumbersome full phonon calculations, being a cheap approach to estimate the thermodynamic properties of the structure, which makes it an attractive option for application in HT schemes.

A systematic treatment of the Debye model has been made, different elastic properties for the distinct magnetic phases and even extending the model to the Debye-Grüneisen approach was considered [88]. This resulted in an increase of the elastic properties to values closer to the ones measured experimentally. Nevertheless, the approximated  $\Delta S_{lat}$  diverges in sign and magnitude from the one calculated from full phonon calculations, as is represented in Figure 5.1. This deviation of the Debye model, in FeRh, can be justified by the

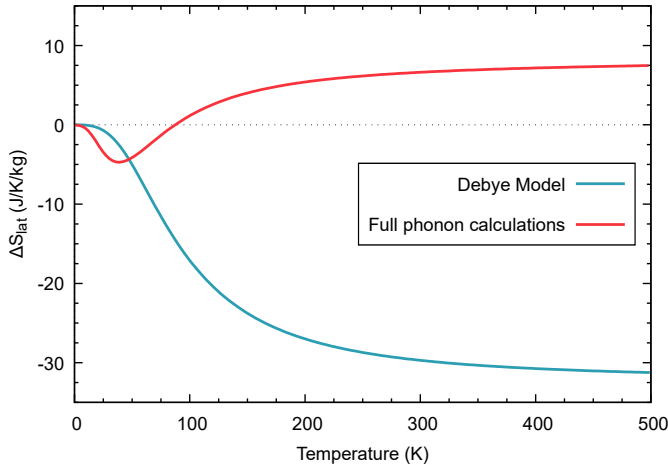


Figure 5.1. Comparison of approximations for the lattice entropy variation between FM and AFM phases using the Debye Model (blue) and full phonon calculations (red). Data from Paper I.

presence of soft vibration modes on the phonon spectrum, which are not included in the model. In magnetic materials, these softenings usually hint at the existence of possible phase transitions and even (if imaginary) predict structural instability. It is reasonable to assume that potential candidates for magnetocaloric materials show similar features in their phonon spectrum, since the existence of a magnetostructural transition <sup>1</sup> appears to be key to achieve the desired high  $\Delta S_{tot}$  for application in refrigeration. Thus, full phonon calculations are necessary for a reliable estimation of  $S_{lat}$  in this class of materials.

However, if we assume that the  $\Delta S_{lat}$  derived from Debye's estimate is correct, then, according to Equation(2.19), a huge contribution of the magnetic subsystem to the total entropy variation is estimated, so  $\Delta S_{tot}$  is close to the observed result. In Ref.[89], the magnetic contribution to the entropy variation was extracted following this assumption. That result of  $\Delta S_{mag} = 43 \text{ J/kg/K}$ , is not reliable and contrasts with other theoretical predictions.

The metamagnetic transition in FeRh differs significantly from the conventional order-disorder transition displayed by popular magnetocaloric materials

<sup>1</sup>in FeRh the transition is isostructural, existing a discontinuous variation of the volume

(except for MnAs which have a similar transition). The conventional Heisenberg Hamiltonian, see Equation (2.35), fails to describe the magnetic ground-state of FeRh correctly, i.e. an expansion of the model is necessary to capture the AFM ground-state [90, 91, 92]. The use of a tailored model is not practical for the HT approach so the  $S_{mag}$  was computed from the adiabatic magnon spectra, as performed in Ref. [93]. Following this approach, the magnetic fluctuations are addressed directly, avoiding the problem above. The calculation of  $S_{mag}$  from the FeRh magnon spectra is achievable since the transition happens at lower temperatures ( $\approx 340\text{K}$ ) well below the Curie temperature ( $\approx 675\text{K}$ ), where it is reasonable to assume spin-wave excitations.

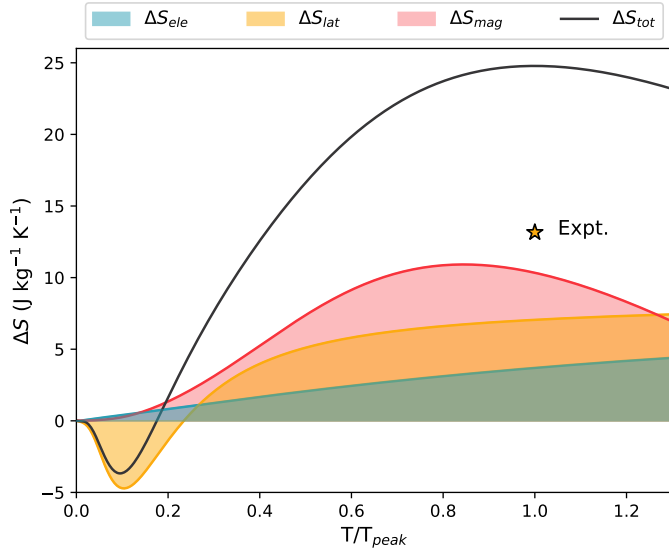


Figure 5.2. Total entropy variation and respective components estimated for the AFM  $\rightarrow$  FM transition of FeRh. Temperature is normalized according to the entropy peak temperature of the experimental (312) and calculated (373) data. Adapted from Paper I with experimental data from Ref. [27].

The estimated total entropy variation between the FM and the AFM phase and respective contributions (lattice, electronic and magnetic) for the entropy are represented in Figure 5.2. All entropy contributions are comparable in magnitude and add with the same sign, which explains the high entropy variation for the order-order transition in FeRh. The highest contribution is from the magnetic subsystem which is responsible for the peak of the total entropy variation at 373 K, in the expected range for AFM $\rightarrow$ FM transition to happen. Associating the entropy peak to the phase transition, the estimated value of  $\Delta S_{tot} = 24.8\text{ J/K/kg}$  is close to experimental findings [12 - 19]  $\text{J/K/kg}$  [94]. The fact that the peak is produced by  $\Delta S_{mag}$  hints that the transition is driven by the magnetic subsystem. More specifically, it hints that the metamagnetic transition in FeRh is driven by small magnetic fluctuations in agreement with previous

works [90, 95, 93, 92], since this result is obtained in the magnon description which is characterized by small magnetic perturbations.

The results discussed above were calculated at the relaxed volumes for the two magnetic phases without consideration of thermal expansion effects. The inclusion of such effects might improve the physical description and lead to more accurate entropy estimations. To verify that, a new estimate for the entropy was performed within the quasiharmonic approximation.

No significant improvement of the calculated values due to the quasiharmonic approximation has been observed, which would justify from a high-throughput point of view, the extra numerical effort. It is observed that although the volume expansion favours an increase in the lattice contribution for the entropy, this happens at the cost of a decrease in the magnetic contribution, which keeps the total variation value nearly constant. The total entropy peak in the quasiharmonic approximation is now located at 316 K, with a value of  $\Delta S_{tot} = 24.4 \text{ J/K/kg}$ . Qualitatively, the physical description becomes more accurate, since the entropy peak becomes sharper, as expected from a first-order transition. Thus, from the obtained results, it can be stated that calculations at the relaxed volumes balance in a very satisfactory way the accuracy and the computational effort, which is key for high-throughput applications.

## 5.2 Gadolinium

Metamagnetic transitions like the one in FeRh are uncommon around room temperature. More commonly, the MCE is explored around the ferromagnetic (and ferrimagnetic) to paramagnetic transition. Thus, it is pertinent to benchmark the entropy calculations in this context.

Elemental Gd (metal) serves as a reference system in characterising magnetocalorics for room-temperature applications. Gadolinium undergoes a FM  $\leftrightarrow$  PM transition around 298K, with a significant magnetocaloric response  $\Delta S_{iso} = 5.2 \text{ J/K/kg}$  and  $\Delta T_{adi} = 4.7 \text{ K}$  (cyclic conditions under a field of 2T). Then, Gd is a natural choice as a benchmark system for the entropy calculations for a conventional MCE. Moreover, since its magnetic ordering has a 2nd order transition nature, we must use a different treatment than the previously used in FeRh, to accommodate the continuous phase transformation. This need was also shown in Ref. [96], where an analogous calculation of  $\Delta S_{mag}$  from the MDOS for Gd resulted in an overestimate.

This continuous evolution between FM and PM behaviour can be simulated for the magnetic subsystem with MC simulations. In contrast to the metamagnetic transition of FeRh, the simple Heisenberg Hamiltonian (see Equation 2.35) performs very reasonably in describing the continuous variation of the magnetization with temperature. The magnetic entropy contribution to the MCE can then be calculated by comparing the magnetic heat capacities computed for two different applied magnetic fields, as in Equation (2.16).

However, the calculation of  $\Delta S_{lat}$  and  $\Delta S_{ele}$  is not as straightforward as  $\Delta S_{mag}$ . The direct comparison of the initial and final states  $S_{x,FM}$  and  $S_{x,PM}$ , as done for FeRh, does not take into account the continuous variation of the magnetization with the temperature. Thus, following that approach, one would overestimate the alterations in physical properties during the transition. For an accurate calculation, it is necessary to consider the intermediate stages, which translate into additional computations. As an alternative, to save resources, we can explore the smooth nature of 2nd order transitions and estimate  $S_x$  of the intermediate phase as a weighted (by  $\alpha$ ) average of the initial and end stages:

$$S_{x,inter} = \alpha S_{x,FM} + (1 - \alpha) S_{x,PM} . \quad (5.1)$$

This approximation is analogous to the use of VCA to calculate alloy properties. Instead of chemical species, we mix two distinct magnetic phases: the FM, fully ordered with the magnetization equal to  $M_0$  and the PM phase, fully disordered with zero magnetization. In this sense, at a given temperature, the intermediate state can be characterized by its magnetization, which varies between  $M_0$  and 0. Thus, the normalized magnetization,  $M(T)/M_0$  is a natural choice for the weight  $\alpha$ :

$$S_x = \frac{M(T)}{M_0} S_{x,FM} + \left(1 - \frac{M(T)}{M_0}\right) S_{x,PM} . \quad (5.2)$$

In practice, this approach is equivalent to using a linear interpolation of the vibrational/electronic density of states to describe the intermediate states, as illustrated in Figure 5.3. Combining Equation (5.2) with the magnetization curves simulated with MC for different fields, the  $\Delta S_{ele}$  and  $\Delta S_{lat}$  contributions to the MCE can be calculated.

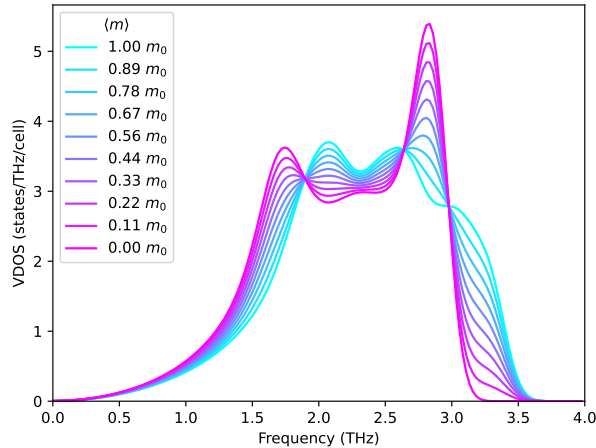


Figure 5.3. VCA-like interpolation of VDOS between the FM,  $\langle m \rangle = m_0$ , and PM,  $\langle m \rangle = 0$ , states for Gd.

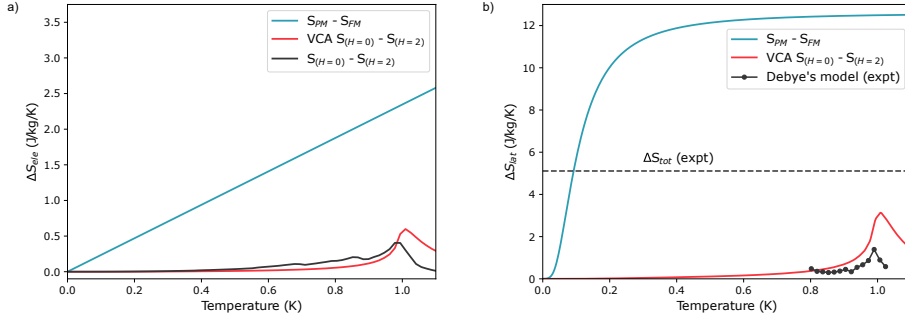


Figure 5.4. Comparison of different approaches for the calculation of the electronic a) and lattice b) entropy contributions for Gd. Data from Paper II

In Figure 5.4, the results of a 2nd-order description can be compared against the first-order treatment ( $S_{FM} - S_{PM}$ ) performed in FeRh. It becomes evident that the latter overestimates  $\Delta S$  by the value of  $\Delta S_{lat}$ , which is twice as big as the total  $\Delta S$  measured. The performance of the VCA-like approximation in Equation (5.2) was tested against the proper calculation of the physical properties of the intermediates states (using CPA-DLM) for the  $\Delta S_{ele}$  within the Sommerfeld approximation. As seen in Figure 5.4a, the VCA-like approximation captures the behaviour and the same order of magnitude as the more complete approach, motivating its use in HT calculations. While  $S_{ele}$  calculations are not resource intensive, since the intermediate states and the PM phase can be described easily with CPA-DLM, the same does not hold for  $S_{lat}$ . The calculation of full-phonons is resource intensive and often performed on codes with plane waves basis, in which the magnetic disorder must be mimicked with SQS that also needs to be computed. Therefore for  $S_{lat}$  the VCA-like scheme has the optimal balance between accuracy and cost.

Comparing the entropy contributions calculated with each other and their sum (the total entropy variation) with the experimental values, in Figure 5.5, offers a better insight into the accuracy of the calculations. In the literature, the MCE of Gd is often associated exclusively with the magnetic subsystem since no structural transformation is observed. In Figure 5.5, we can observe that  $S_{mag}$  is the dominant term and  $S_{ele}$  has a negligible contribution, in agreement with the expectations. However, the calculated  $\Delta S_{lat}$  is unexpectedly large for a pure magnetic transition. Since the calculated  $\Delta S_{mag}$  is close values reported in similar calculations [97], it is possible to determine the overestimation of the total entropy contribution with the high  $\Delta S_{lat}$ .

To investigate the unexpected value of  $\Delta S_{lat}$ , the respective estimate from Debye's model,  $\Delta S_{Debye}$ , was calculated with experimental inputs of the elastic properties of Gd under different temperatures and magnetic fields [98]. While the calculations were in good agreement for  $\Delta S_{Debye}$  based on low-temperature properties, for elastic constants at room temperature, the  $\Delta S_{Debye}$  estimated is considerably smaller. In that case, the entropy contribution is predicted to be

smaller, and the  $\Delta S_{tot}$  becomes close to the experimental value. Such results hint at two important insights. The first is the calculated  $\Delta S_{lat}$  is overestimated by the lack of inclusion of the finite temperature effects, which have a greater impact than the change of magnetic phase. The second is that contrary to what is usually assumed for Gd,  $\Delta S_{lat}$  has a finite non-neglectable contribution to the entropy variation in the MCE.

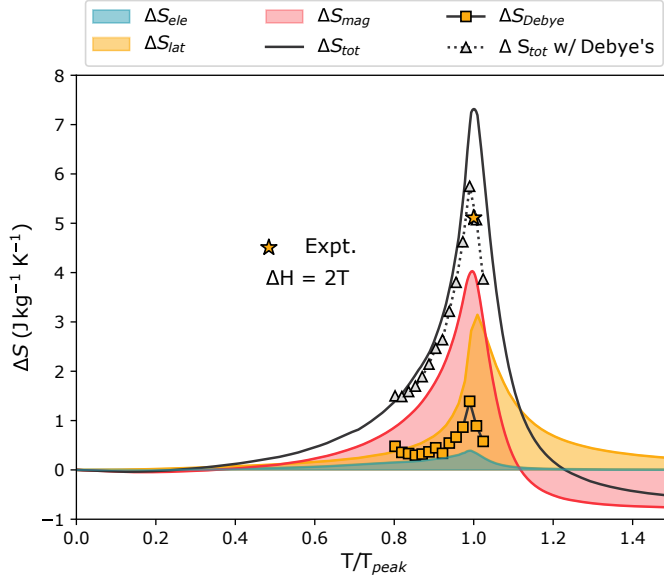


Figure 5.5. Variation of the total and individual contribution of entropy change between the PM and FM configuration at a magnetic field change of 2T. Temperature is normalized according to the entropy peak temperature of the experimental (291K) and calculated (317K) data. Adapted from Paper II, experimental data from Ref. [27]

### 5.3 Remarks

The results from the benchmark tests suggest that it is possible to calculate the entropy variation associated with the MCE without tailoring a material-specific model. This suggests using  $\Delta S$  as a screening parameter in high-throughput calculations to search for new magnetocaloric materials. It is dangerous to generalize the conclusions from two tests, but it seems sensible to expect that:

- individual contributions  $\Delta S_i$  are overestimated when calculated from first-principles.
- the vibrational/elastic properties of both phases magnetic phases involved should always be considered.
- VCA-like schemes for mixing phases seem reasonable.

- in 1st-order transitions the inclusion of thermal effects via a quasi-harmonic treatment is less important for a reasonable estimate of  $\Delta S$ , but it could be more relevant in the treatment of 2nd-order transitions.

It is important to note that in the phonon calculations for the PM of Gd, a simplification was made by treating the f-electrons as core states without spin-polarization. While this treatment is reasonable for Gd [99], its application is limited to rare-earth elements. In general, it is necessary to generate a SQS and calculate the forces. However, since the magnetic disorder breaks the symmetry, this requires a bigger effort to do full phonon calculations than the ordered configuration. In the literature, there are proposed averaging schemes that reduce the computational effort [100, 101], but nevertheless, the heavy cost of these calculations should be kept in mind when planning for HT calculations.



# 6. Magnetism and Lattice Coupling

*Prepare for trouble!  
And make it double!*

---

intro of Team Rocket's motto

It is generally accepted in the field that the coupling between the lattice and the magnetic subsystems plays a crucial role in the MCE [43]. The description of this coupling is not trivial and often requires some system-tailored approach. This chapter explores the magnetic properties' dependence on the structural properties. More specifically, it discusses how volume changes, structural changes and phase mixing can affect the magnetism in systems such as FeRh, Gd, and  $\text{Mn}_{0.5}\text{Fe}_{0.5}\text{NiSi}_{0.95}\text{Al}_{0.05}$ , respectively.

The analysis of FeRh expands upon the findings presented in Paper I. For Gd, the discussion is based on Paper IV and for  $\text{Mn}_{0.5}\text{Fe}_{0.5}\text{NiSi}_{0.95}\text{Al}_{0.05}$  on Paper III.

## 6.1 FeRh

Most promising magnetocaloric materials exhibit magnetostructural transitions, indicating a strong coupling between lattice and magnetic components. The quasiharmonic calculations for FeRh (see Supplement of Paper I), suggest an interplay between  $\Delta S_{mag}$  and  $\Delta S_{lat}$ , which motivates further analysis.

Table 6.1 presents the volume-dependent variation of the stronger exchange coupling parameters  $J_{ij}$  in the quasiharmonic calculations (for  $V > V_0$ ). The trend in the FM state suggests an increase in the Curie temperature with volume expansion. This is due to the FM coupling between Fe and Rh atoms weakening more slowly than the AFM coupling between Fe atoms, aligning with experimental data [102], see Figure 6.1. In the AFM phase, while the exchange couplings follow a similar trend, their impact on the transition temperature is less clear. The quasiharmonic indicates a lower transition temperature for larger volumes, consistent with measurements [102], but free energy results observe a different trend, precluding definitive conclusions.

The results highlight the sensitivity of Fe-Fe coupling to volume changes, particularly in the FM phase where the interplay of FM (Fe-Rh) and AFM (Fe-Fe) couplings is crucial. At the relaxed volume, Fe-Rh couplings predominate, but AFM Fe-Fe couplings change more rapidly with volume variation, suggesting potential magnetic configuration changes under pressure.

Subsequent calculations for compressed FeRh volumes corroborate these findings (see Figure 6.1a). MC simulations at  $T=1\text{K}$  predict pressure-induced alterations in the magnetic arrangement.

Coupling	$J_{ij}$ (mRy)		$\partial J_{ij}/\partial V$ (mRy/Å <sup>3</sup> )	
	AFM	FM	AFM	FM
Fe-Fe <sub>1st</sub>	-0.54	-0.08	0.14	0.07
Fe-Fe <sub>3rd</sub>	-0.46	-0.42	0.04	0.14
Fe-Rh	-	0.94	-	-0.04

**Table 6.1.** Stronger exchange couplings calculated for FeRh's AFM and FM phases and their volume variation. Includes interactions between Fe atoms at nearest and third-nearest neighbours.

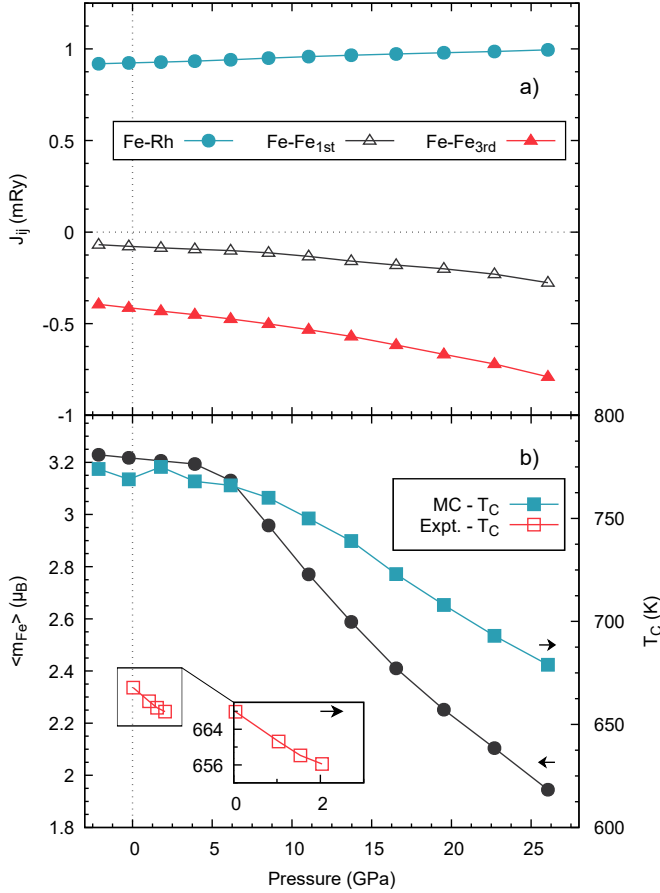


*Figure 6.1.* Magnetic parameter variations in the FM phase under isotropic pressure. The top panel a) shows stronger exchange parameters, while the bottom panel b) displays mean-field estimates for the Curie temperature for FeRh and average magnetic moment for Fe atoms from Monte Carlo simulations (blue squares). Experimental Curie temperature data are inset (red squares).

Figure 6.1.b shows the averaged magnetic moment for Fe sites decreasing at pressures above 6 GPa, hinting at a disordered phase. Rh atom moments remain constant, but the deviation of the direction of Fe moments around Rh suggests a competition between FM (Fe-Rh) and AFM (Fe-Fe) couplings, leading to a non-collinear configuration (see Figure 6.2) and a reduced total magnetic moment.

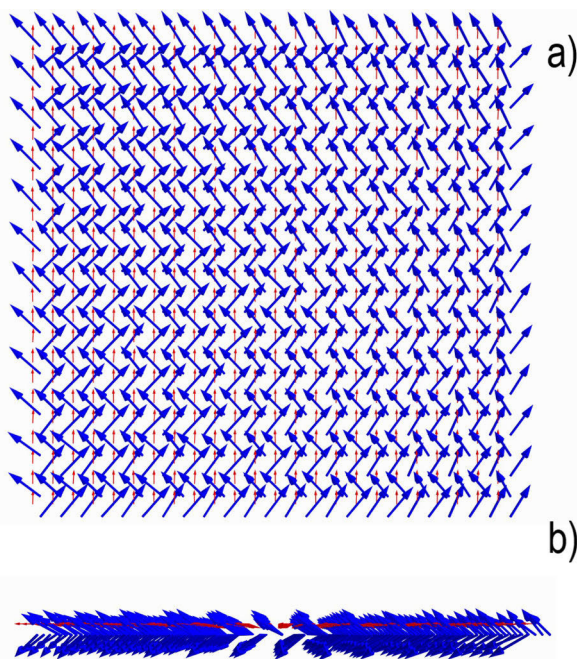


*Figure 6.2.* Cross-sectional (a) and transversal (b) view of the magnetic configuration along a x-plane at 22.6 GPa. Blue and red arrows represent magnetic moments of Fe and Rh, respectively.

Literature references to such non-collinear configurations are sparse. Gu et al. [93] predicted a non-collinear ground state in LDA calculations, but this was deemed unstable with non-local corrections. Zhou et al. [103] hinted at a non-pure FM state, while Sandratskii et al. [104] confirmed a non-collinear configuration.

## 6.2 Gadolinium

The benchmarking tests for *hcp* Gd show that  $\Delta S_{lat}$  has a non-negligible contribution (Paper II), due to the alteration of the vibrational properties induced by the change of the magnetic phase. Experimentally, the link between lattice and structure for *hcp* Gd is evidenced by the behaviour of the  $C_{33}$  elastic constant, which displays a sharp variation around the Curie temperature [98].

In Paper IV, the interplay between the magnetic properties and structure of Gd was further explored, specifically focusing on how pressure affects its magnetic ordering temperature. Experimental data reveals that as pressure increases, the Curie temperature undergoes a roughly linear decrease, reaching a reduction of about 22% at 6 GPa [105, 106, 107]. Beyond this critical pressure threshold, the magnetization collapses.

Unlike the previous case of FeRh, volume changes in Gd have minimal impact on its magnetic properties, being insufficient to replicate the experimental trend observed under pressure. This aligns with the established model where the half-filled  $4f$  shell leads to well-localized  $4f$  spin moments. While the application of pressure often reduces the localization of states, potentially altering the magnetic properties, literature consensus holds that this is not the case for the Gd  $f$ -states within the considered pressure range [108]. In Ref. [109] it is advanced that the decrease of the lattice by pressure lowers the bottom of the conduction band, causing a decrease in the density of states at Fermi energy,  $D(\epsilon_F)$ , and thus weakening the exchange parameters between spin moments, which results in the decrease of  $T_C$ . However, DFT calculations and the pressure dependence shown in Figure 6.3 challenge this view, showing neither a consistent decrease of  $D(\epsilon_F)$  with pressure nor a positive correlation between  $D(\epsilon_F)$  and  $T_C$ <sup>1</sup>.

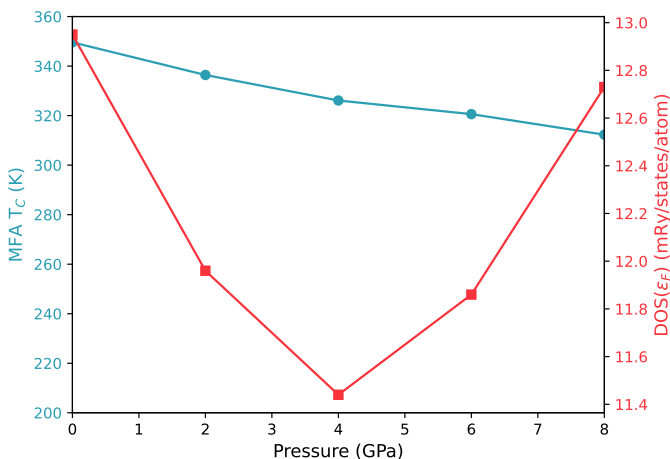


Figure 6.3. Mean-field Curie temperature (blue, left) and density of states at the Fermi energy (right, red) dependence with pressure, calculated for the *hcp* Gd considering exclusively volumetric effects,

Like other rare-earth metals, Gd undergoes pressure-induced polymorphism, transitioning through structural phases from *hcp* to *9R* (Sm-type) around 2 GPa and then to *dhcp* around 6.5 GPa. These structural transforma-

<sup>1</sup>Estimated in the mean-field approximation with calculated  $J_{ij}$

tions are important for the change of the magnetic properties. In experimental studies of Gd, neutron diffraction patterns have revealed different magnetic orderings in the Sm-type (AFM) and *hcp* (FM) structures [105] confirming the expectations. There are also indications that the *dhcp* phase may have a distinct (AFM) magnetic character, although the observations are not conclusive [105].

**Table 6.2.** Crystallographic properties of Gd polymorphs: comparison between the layer multiplicities, symmetries, and distances between Nearest Neighbours (NN) for *fcc* and *hcp* environments.

Structure	Spacegroup	Layer environment	Site symmetry	1st NN	2nd NN	3rd NN
<i>hcp</i>	194	2 × <i>hcp</i>	-6m2	6	6	6
Sm-type (9R)	166	6 × <i>hcp</i>	3m	3	3	6
		3 × <i>fcc</i>	-3m	3	6	6
<i>dhcp</i>	194	2 × <i>hcp</i>	-6m2	6	6	6
		2 × <i>fcc</i>	-3m.	6	6	6

The polymorphs of Gd within the 0-6.5 GPa pressure range can be described as hexagonal stacked structures with different repeating patterns of A, B, and C hexagonal layers as illustrated in Figure 6.4. According to the pattern formed, the layers have face-centred-cubic (*fcc*) or *hcp* environment environments, which possess different site symmetries (see Table 6.2). Within these 3 structures, the Sm-type stands out by its lower symmetry. The different coordination of *fcc* sites found in the Sm-type structure is explained by a small difference in separation between the first and second nearest neighbours ( $\approx 0.014 \text{ \AA}$ ), which are grouped to the same coordination shell in the other structures. Aside from the symmetry considerations, the main distinction between the structures centres on the ratio between *hcp* and *fcc* layers, as shown in Figure 6.4 and Table 6.2.

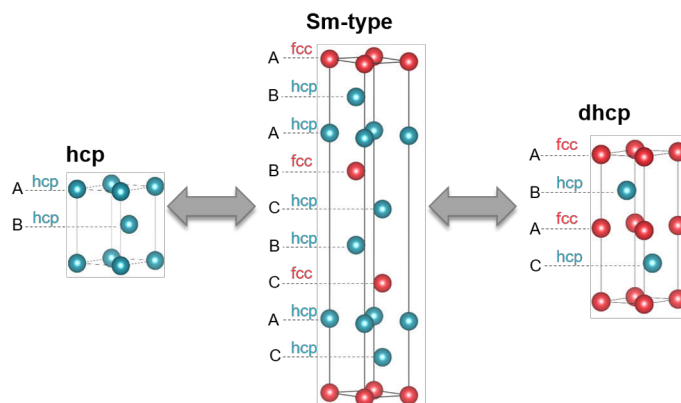


*Figure 6.4.* Illustration of polymorph structures of Gd. Sites with *fcc* environment are coloured red while sites with *hcp* environment are coloured blue.

## Groundstate and magnetic properties

While FM order is well-established for bulk Gd *hcp* under standard temperature and pressure conditions<sup>2</sup>, the magnetic orderings of its Sm-type and *dhcp* structures remain an open debate. Considering the magnetic behaviour of similar rare-earth metals and the fact that pressure within the discussed range does not delocalize the  $4f$  orbitals, it is anticipated that these structures exhibit AFM ordering between hexagonal planes. Neutron diffraction patterns from Ref. [105] and first-principles calculations [108] for the Sm-type structure support this expectation but also indicate some magnetic frustration. For the *dhcp* structure, the diffraction data from Ref. [105] remains inconclusive, although there are indications of a complex AFM ordering, accompanied by magnetic frustration.

The magnetic configuration for the Sm-type structure as proposed by Ref. [105] is a 2-layer *hcp* block that aligns anti-ferromagnetically in a periodic pattern, with *fcc* sites in between characterised by magnetic frustration, see Figure 6.5. If we assume a static configuration, this frustration implies that the *fcc* layer sites are either completely disordered (PM) or they are ordered within the layer without forming a periodic pattern along the stacking direction. The findings in Paper IV support the latter scenario.

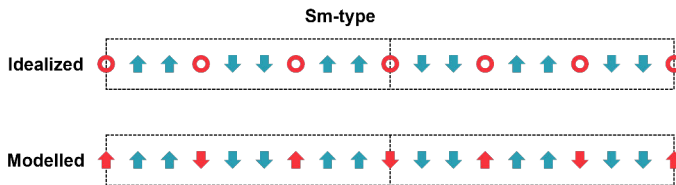


Figure 6.5. Diagram of the magnetic configurations along the hexagonal stacks. The circles represent sites with frustrated magnetic while the colours indicate *fcc* (red) and *hcp* (blue) environments.

To identify the ground state, the energies from DFT calculations for various magnetic configurations in the Sm-type and *dhcp* structures were compared. The frustration was considered by an AFM pattern between the frustrated sites to ensure a net magnetic moment of zero, see Figure 6.5. Under these constraints, the ground state of the Sm-type structure was found to be a 3-layer block AFM, i.e. the variant in Figure 6.5 with ordered moments at the frustrated sites, while the ground state of the *dhcp* structure is a 2-layer block AFM.

The  $J_{ij}$  exchange parameters calculated in Paper IV for the ground states of the considered structures exhibit a common trend: the nearest in-plane and out-of-plane interactions are FM, while the second and third nearest out-of-plane interactions are AFM. Additionally, the stronger interactions seem to be confined in the range within two hexagonal planes/layers. In both the Sm-type and the *dhcp* structures, the  $J_{ij}$  involving *fcc* sites ( $fcc - fcc$ ,  $fcc - hcp$ ) are generally weaker than pure *hcp - hcp* interactions. This trend could account for

<sup>2</sup>273.15 K and 100 kPa ( $\approx 1$  atm)

the transition from FM to AFM orderings under pressure due to the formation of *fcc* layers during the structural transformations. The diminished FM couplings at *fcc* sites amplify the effects of AFM couplings, resulting in an AFM ordering. This scenario of competing AFM and FM couplings is supported by the small difference in energy obtained in DFT for most considered magnetic configurations and by the non-collinear configurations obtained in MC simulations for the Sm-type, using these  $J_{ij}$  as input. Similarly, MC simulations for the *dhcp* phase indicate unexpected configurations, evidencing strong FM-AFM coupling competition, in line with this paradigm.

A key question remains regarding the magnetic ordering of the Sm-type structure in Gd. While there is a consensus in the literature about its AFM ordering, supported by both theoretical and experimental evidence, a puzzle remains: how to account for the observed finite magnetization in Gd up to about 6 GPa, well beyond the *hcp* to Sm-type transition? Diffraction techniques indicate the presence of *hcp* domains even above the transition pressure, suggesting that these domains contribute to the magnetization in the mixed *hcp* + Sm-type phase until it eventually collapses [110, 106, 105]. In Paper IV, MC simulations have been used to investigate whether the Sm-type structure could adopt a magnetic configuration with a finite magnetization under the influence of a magnetostatic field generated by the *hcp* phase, or when the frustrated *fcc* sites are modeled with FM ordering. However, these simulations yield a small finite magnetization, not in line with the magnitude observed experimentally, suggesting that a more comprehensive description is needed to accurately represent the interaction between these phases.

## Stacking fault model

Since the different structures of Gd are closely related, the structural transitions among these Gd polymorphs can be understood as variations in the *fcc* – *hcp* ratio. Then, the emergence of *fcc* layers during e.g. the *hcp* → Sm-type transition is comparable to the formation of period stacking faults in the *hcp* structure. Consequently, a key question emerges about the nature of pressure-induced transformations [111]: Do two-phase regions distinctly separate *hcp* and Sm-type structures, as well as Sm-type and *dhcp* structures, with pressure favouring the growth of one phase over the other? Or do *fcc* stacking faults build up and order to form the new phase?

Though the formation and accumulation of *fcc* stacking faults occur in both, in the first scenario, these processes take place at the interface between phases, whereas in the second, they lead to the creation of periodic structures with intermediate ratios of *fcc* – *hcp* layers. Distinguishing between a two-phase system and an intermediate structure using diffraction patterns poses a significant challenge since intermediate structures, such as those between *hcp* and Sm-type, may exhibit characteristics of both ends of the spectrum.

The attractiveness of a gradual transformation between the polymorph structures due to stacking fault formation/accumulation as a perspective lies in its capacity to provide a simplified framework for understanding the structural transformations in Gd. It reframes the issue, focusing on how magnetic properties correlate with the presence of *fcc* stacking faults, which, as discussed earlier, have exchange couplings weaker than the *hcp* layers, likely stabilising the AFM ordering with their accumulation. In Paper IV, a simplified model is presented to demonstrate how the formation of *fcc* stacking faults influences the magnetic ordering temperature.

In systems with a single magnetic sub-lattice, the mean-field approximation applied to the Heisenberg Hamiltonian yields the magnetic ordering temperature ( $T_{critical}$ ) given by [79, 46]:

$$T_{critical} = \frac{2J_0}{3k_B}. \quad (6.1)$$

Here,  $J_0$  denotes the sum of exchange interactions at a magnetic site, defined as  $J_0 = \sum_k J_{0k}$ . In the previous analysis of the  $J_{ij}$  parameters it was possible to identify two sets of  $J_{ij}$  parameters according to the environment of the layer, suggesting two distinct  $J_0$  values. The first,  $J_0^{hcp}$ , is based on a *hcp* site and includes interactions between *hcp*–*hcp* and *hcp*–*fcc* pairs. The second,  $J_0^{fcc}$ , is centered on a *fcc* site and accounts for *fcc*–*fcc* and *fcc*–*hcp* interactions.

This distinction in principle corresponds to the presence of two magnetic sub-lattices, making Equation (6.1) inapplicable (except for the *hcp* structure), however, the similarities between *hcp* and *fcc* structures, particularly in terms of magnetic moment and coordination, allow for an alternative approach. In Paper IV it is proposed to calculate a mixed  $J_0$  as a weighted average, similar to a VCA approach, of the two environment-specific  $J_0$ :

$$J_0 = xJ_0^{hcp} + (1 - x)J_0^{fcc} \quad (6.2)$$

where  $x$  is the proportion of *hcp* sites in the unit cell. For the *hcp*, Sm-type, and *dhcp* structures, the value of  $x$  is 1, 2/3, and 1/2, respectively. Applying Equation (6.2) in Equation (6.1) one obtains a relation linking  $T_{critical}$  with the *fcc* stacking faults:

$$T_{critical} = 2 \frac{xJ_0^{hcp} + (1 - x)J_0^{fcc}}{3k_b}. \quad (6.3)$$

Note that  $J_0^{hcp}$  and  $J_0^{fcc}$  are structure-specific values. Thus, Equation (6.2) is most accurate when  $x$  closely aligns with the *hcp* ratio inherent to the structure under consideration. However, for simplification purposes and to discern general trends, in Paper IV is introduced a practical simplification, where  $J_0^{hcp}$  and  $J_0^{fcc}$  are fixed to values characteristic of the Sm-type structure.

Further Equation (6.3) must be reformulated to relate  $x$  to the pressure. Assuming a constant rate of *fcc* stacking faults formation between the *hcp* → Sm-type and Sm-type → *dhcp* transformation, one obtains that  $x$  varies at the rates



-0.16 GPa and -0.037 GPa respectively. This leads to a linear interpolation for the proportion of *hcp* layers in the unit cell:

$$x = \begin{cases} 1 - \frac{1}{6}P, & \text{for } P \leq 2.0 \text{ GPa} \\ \frac{2}{3} - \frac{1}{27}P, & \text{for } 2.0 < P < 6.5 \text{ GPa} . \end{cases} \quad (6.4)$$

Combining Equations (6.3) and (6.4) one obtains a simple model describing the dependence of the magnetic ordering temperature on the formation of *fcc* layers.

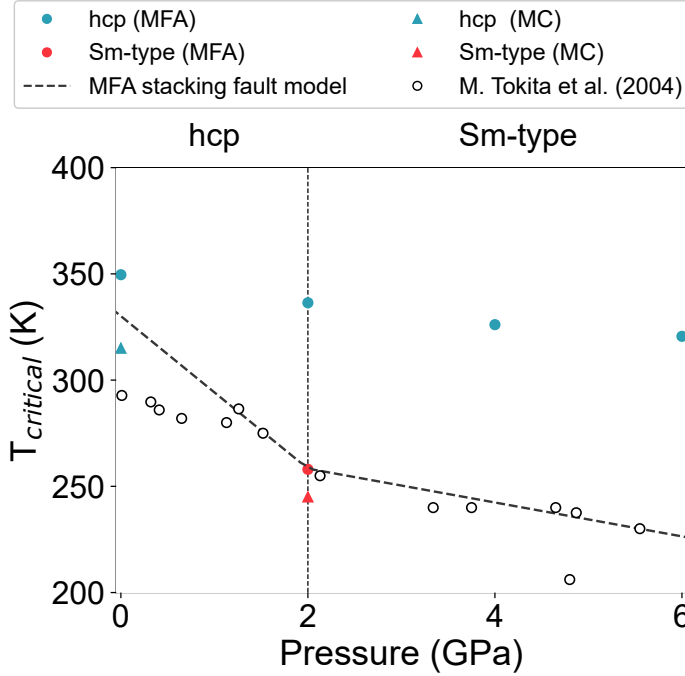


Figure 6.6. Magnetic ordering temperature variation ( $T_{Critical}$ ) with pressure of Gd. Open circles represent experimental data taken from Ref. [109]. Filled circles denote  $T_{Critical}$  values derived from mean-field approximations using ab-initio exchange parameters. Triangles illustrate critical temperatures obtained from Monte Carlo simulations. The solid line in the figure signifies the mixing model for *hcp* and *fcc* stacks. Extracted from Paper IV.

The results of this model are in good agreement with experimental findings reported in Ref. [109], as shown in Figure 6.6. Such agreement in the pressure range of the Sm-type structure (2-6.5 GPa) supports the hypothesis of the formation of *fcc* stacking faults under pressure as the primary mechanism for the variation of  $T_{critical}$  observed experimentally. In the region between 0-2 GPa, the model does not follow so closely the experimental data, since it predicts a sharper decrease of  $T_{critical}$  compared to the observed value. While the estimated trend aligns with the data points closer to *hcp*  $\rightarrow$  Sm-type transition, where the application of Equation (6.3) should be more accurate, for lower

pressures the experimental trend is closer to the calculations of  $T_{critical}$  based solely on volumetric effects (depicted as blue circles in Figure 6.6). Intuitively, it sounds reasonable that the *hcp* structure would withstand some volume contraction before entering the regime of formation of *fcc* environments.

The model distinctly highlights two different rates of change in  $T_{critical}$  with pressure: one during the *hcp*  $\rightarrow$  Sm-type transformation and another during the Sm-type  $\rightarrow$  *dhcp* transition. This trend is visible also in experimental data and supports the hypothesis of *fcc* stacking fault accumulation as a primary mechanism for the pressure-induced variation in  $T_{critical}$ . More precisely, the experimental observation of two trends aligns with Equation (6.4) where it is estimated that *fcc* stacks form at a different rate between the polymorphs in the transition chain, and thus varying  $T_C$  differently.

However, the model has limitations due to its simplicity (based on MFA) and the use of fixed  $J_0^{hcp}$  and  $J_0^{fcc}$  values. It doesn't predict the collapse of magnetization near the transition to the *dhcp* phase. The inclusion of  $x$  dependence on the  $J_0^{hcp}$  and  $J_0^{fcc}$  is an obvious and fairly simple extension of the model but requires calculating  $J_{ij}$  parameters for theoretical intermediate structures, which poses challenges in validating magnetic configurations. Furthermore, the observed competition between FM and AFM couplings, particularly in the Sm-type structure, results in non-collinear configurations in MC calculations and potential magnetic frustration in the *dhcp* structure, complicating the interpretation of calculated  $T_{critical}$  values in terms of magnetization.

### 6.3 $Mn_{0.5}Fe_{0.5}NiSi_{0.95}Al_{0.05}$

Intermetallic MnTX compounds (where T = Co or Ni, and X = Si or Ge) are an interesting class of materials, due to the possibility of magnetostructural transitions [112]. At room temperature, these compounds typically exhibit an orthorhombic TiNiSi type structure. However, as temperatures increases, they generally transition to a hexagonal, ordered  $Ni_2In$  type structure, as depicted in Figure 6.8. This transformation is diffusionless and classified as first-order [112].

The parent compound, MnNiSi, undergoes a structural transition at approximately 1200K [113] and a magnetic transition at around 600K. The presence of both transitions spurred the interest in this compound in the search for new magnetocaloric and shape-memory materials, due to the possibility of coupling the magnetic and structural transitions through alloying. Alloys such as  $Mn_{1-x}Fe_xNiSi_{1-y}Al_y$  are particularly promising, as they not only enable tuning and coupling of these transitions but also exhibit significant magnetocaloric potential due to the large entropy change associated with their first-order transition. Moreover, these alloys have a structural transition temperature ( $T_{st}$ ) close to room temperature. In Paper III, the magnetic properties of  $Mn_{1-x}Fe_xNiSi_{0.95}Al_{0.05}$  are examined, focusing on compositions near  $x =$

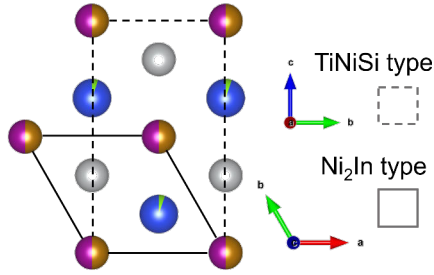


Figure 6.7. Hexagonal phase of  $\text{Mn}_{0.5}\text{Fe}_{0.5}\text{NiSi}_{0.95}\text{Al}_{0.05}$  represented in the  $\text{Ni}_2\text{In}$  type and  $\text{TiNiSi}$  type (dashed) structures. Adapted from Paper III

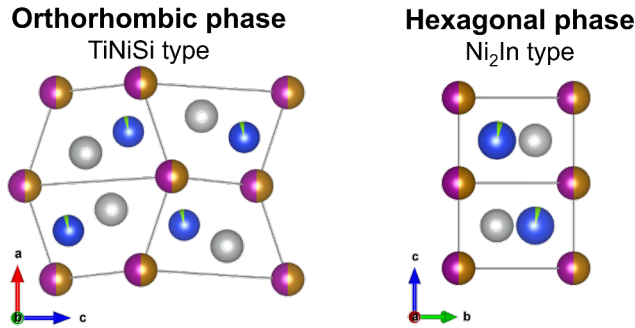


Figure 6.8. Hexagonal and orthorhombic phases of  $\text{Mn}_{0.5}\text{Fe}_{0.5}\text{NiSi}_{0.95}\text{Al}_{0.05}$ . The colours represent the site occupation by different chemical elements: Mn (pink), Fe (orange), Ni (grey), Si (blue) and Al (green). Adapted from Paper III

0.5. This study also delves into the underlying mechanisms of the magnetostructural transition.

## Magnetic properties of the phases

Although the orthorhombic and hexagonal phases share structural similarities, as illustrated in Figure 6.8, their magnetic properties differ significantly. Paper III reveals minimal differences in local magnetic moments, but the  $J_{ij}$  values, as shown in Figure 6.9, exhibit distinct characteristics. Notably, in the hexagonal phase, the third and fourth nearest neighbours exhibit AFM coupling, while in the orthorhombic phase, these couplings are FM. This leads to a competition between FM and AFM couplings in the hexagonal phase, resulting in a non-collinear magnetic configuration with an ordering temperature of 265 K in MC simulations. In contrast, the orthorhombic phase stabilizes into an FM configuration with a Curie temperature of 625 K.

The hexagonal phase can be described within a  $\text{TiNiSi}$  type structure, see Figure 6.7. This representation highlights small differences in lattice parameters between the phases, while in the hexagonal phase the atoms populate high

**Table 6.3.** Variation of the mean-field Curie Temperature with the structural parameters of the phases. Adapted from Paper III

Phase	Wyckoff positions	a (Å)	b/a	c/a	MFA $T_C$ (K)
hexagonal	hex	6.88	0.74	0.58	305
intermediate	ort	6.88	0.74	0.58	611
intermediate	ort	6.94	0.74	0.58	617
orthorhombic	ort	6.94	0.81	0.53	823

symmetry sites, in the orthorhombic phase the atoms are slightly displaced from these sites. Analysis of hypothetical structures combining geometric properties (sites, lattice parameters and respective ratios) from both phases indicates that lattice ratios and site displacements significantly influence their magnetic characteristics, as detailed in Table 6.3. The analysis of the  $J_{ij}$ , see Figure 6.9, suggests that AFM coupling increases with lattice ratio variations, possibly due to expanded distances between hexagonal planes. Furthermore, atom displacements in the orthorhombic phase contribute to stronger FM couplings, particularly around  $d = 4.8\text{Å}$ . These couplings correspond to the furthest couplings from the splitting of the hexagonal phase's in-plane nearest neighbour coupling into three distinct interactions.

Since the high-temperature hexagonal phase has its  $T_C$  below the structural transition  $T_{tr}$ , experimental confirmation of its non-collinear state is difficult. Therefore, the description of the magnetic properties of this compound predominantly focuses on the orthorhombic phase. The observed ferromagnetic configuration and magnetization ( $2.2\mu_B/f.u.$ ) closely align with experimental findings ( $\approx 2.0\mu_B/f.u.$ ), although the Curie temperature predicted by Monte Carlo simulations (625K) is significantly higher than the experimentally measured value ( $\approx 300\text{K}$ ). Intriguingly, this predicted  $T_C$  is closer to that of the parent compound MnNiSi (600K [113]) and the similar alloy  $\text{Mn}_{0.5}\text{Fe}_{0.5}\text{NiSi}$  (475 K [114]). Note that the  $T_C$  for the latter case differs unexpectedly from the compound studied in Paper III,  $\text{Mn}_{0.5}\text{Fe}_{0.5}\text{NiSi}_{0.95}\text{Al}_{0.05}$ , considering the small doping with Al, a non-magnetic species.

## Magnetic composite

Reference [115] shows that increasing Al doping in  $\text{Mn}_{0.6}\text{Fe}_{0.4}\text{NiSi}_{1-x}\text{Al}_x$  alloys favours the hexagonal phase, consequently lowering the temperature of the magnetostructural (MST) transition. Supporting this, X-ray powder diffraction (XRPD) data from Paper III and other studies (e.g., [116, 117]) reveal the co-existence of orthorhombic and hexagonal phases in similar compounds, even at temperatures far from the MST transition. In these cases, the minority phase typically constitutes 10%-15% of the total. Given the gradual increase in the minority phase's proportion until the first-order transition and the significant

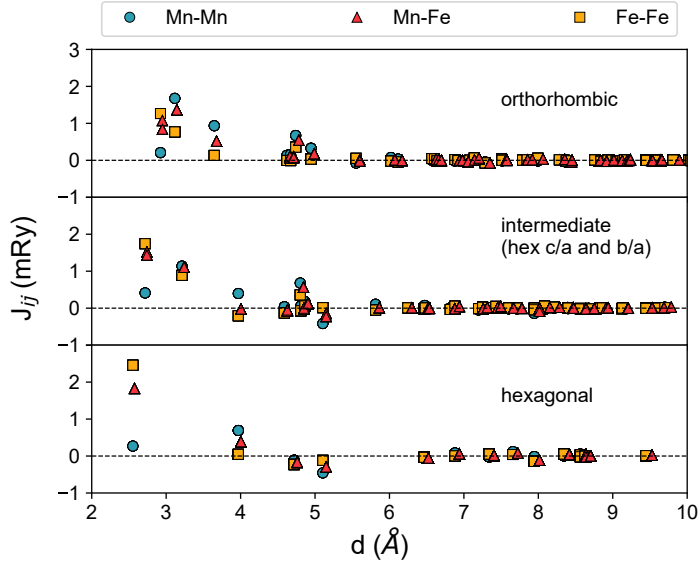


Figure 6.9. Calculated exchange parameters  $J_{ij}$  for  $\text{Mn}_{0.5}\text{Fe}_{0.5}\text{NiSi}_{0.95}\text{Al}_{0.05}$  in the hexagonal, orthorhombic phases and an intermediate structure corresponding to the orthorhombic phase with the lattice parameters ratio  $c/a$  of the hexagonal phase

difference in magnetic properties ( $T_C$  and ordering) between the phases, Paper III suggests the need for accounting for phase mixture to accurately calculate  $T_C$ .

A similar situation is described in the model proposed by Skomski and Sellmyer [118] for nanocomposites. Despite the different Curie temperatures of the phases within these composites, nanocomposites generally exhibit a singular  $T_C$  [118]. The findings of Ref. [118] reveal that  $T_C$  is influenced by the microstructure, typically exceeding the average of the transition temperatures of the constituent phases. Building on these insights, Paper III investigates the magnetic properties of  $\text{Mn}_{0.5}\text{Fe}_{0.5}\text{NiSi}_{0.95}\text{Al}_{0.05}$  by describing it as a magnetic composite comprising both phases.

Existing experimental data does not provide clear insight into the existence of a microstructure in the magnetic composite. In Paper III, for simplification, the mixture of phases was modelled as atomic-like mixing, treating the magnetic sites (Mn and Fe)<sup>3</sup> as a quaternary high-entropy alloy. In practice, as Figure 6.10 illustrates, both phases and their exchange couplings were mapped in the idealized TiNiSi structure, containing exclusively Mn/Fe sites. Each site was associated with a composition of  $\text{Mn}_{y/2}^{hex}$ ,  $\text{Fe}_{y/2}^{hex}$ ,  $\text{Mn}_{(1-y)/2}^{ort}$ , and  $\text{Fe}_{(1-y)/2}^{ort}$ , where  $y$  is the concentration of the hexagonal phase in the magnetic composite. The UppASD code handles chemical disorder by randomly occupying  $N$  of the sites with the disorder in the simulation box, with  $N$  proportional to

<sup>3</sup>The magnetic moment of Ni is found to behave as an induced magnetic moment, not having an active role in the magnetic order.

the species occupancy. This approach can yield a microstructure with specific magnetic properties. To ensure the results are not dependent on the randomised structure, three independent calculations with  $y = 0.5$  and different seeds for the random number generator were performed, showing no indication of microstructure effects.

Mapping both structures into the same simulation box presents challenges in describing their interactions since inter-phase coupling constants  $J_{Fe^{ort}-Fe^{hex}}$ ,  $J_{Mn^{ort}-Mn^{hex}}$ ,  $J_{Fe^{ort}-Mn^{hex}}$ , and  $J_{Mn^{ort}-Fe^{hex}}$  are unknown and difficult to calculate from first principles. Therefore the  $J_{ij}$  from the pure phases were used and two calculations were performed: one treating inter-phase couplings as within-phase interactions in the hexagonal phase (e.g.  $J_{Fe^{ort}-Fe^{hex}} = J_{Fe^{hex}-Fe^{hex}}$ ), and another treating them as within-phase interactions in the orthogonal phase (e.g.  $J_{Fe^{ort}-Fe^{hex}} = J_{Fe^{ort}-Fe^{ort}}$ ). This method aims to delimit the range of magnetic properties, assuming the correct inter-phase coupling lies between these two extremes.

The MC simulations show a decrease in the magnetization and the magnetic ordering temperature for increasing hexagonal presence in composites majorly orthorhombic. In hexagonal dominant composites, the competition between FM and AFM couplings results in non-collinear configurations, explaining the divergent trends for the two sets of  $J_{ij}^{inter}$  used. Even though these findings indicating a clear variation in magnetic properties with different fractions of hexagonal and orthorhombic phases, the calculated  $T_C$  remains higher than experimental values for hexagonal fractions before transition (12%-31%) at 316 K.

This necessitates accounting for both phase fractions and their temperature variation in simulations. Temperature-dependent magnetization  $M(T)$  curves for various hexagonal fractions were bilinearly interpolated to create a magnetization surface  $M(T, y)$  as a function of temperature and hexagonal fraction, see Figure 6.11. Then, the experimental  $y(T)$  from X-ray powder diffraction analysis was used to trace a path on this surface, reflecting the growth of the hexagonal phase and the structural transition in MC simulation results. The resultant magnetization curves closely align with experimental data, see Figure 6.12, suggesting the MST is driven by structural changes. This is further supported by the relative indifference of  $T_C$  to the set of  $J_{ij}^{inter}$  used, and the sharp magnetization drop at  $T_C$  observed experimentally.

The nature of the MST seems analogous to the one reported for Heusler alloys of the Ni-Mn-X(-Co) (X=Al,Ga) [120], in which it is observed a sharp variation of the magnetization caused by the structural transition. However, in that case, the high-temperature phase is FM and the lower-temperature phase PM.

The MST apparent structural dominance raises questions about the mechanism behind the high MCE observed. This is particularly intriguing given the small predicted  $\Delta S_{mag}$  using a method similar to that for the magnetization curves to calculate the magnetic heat capacity with and without an applied

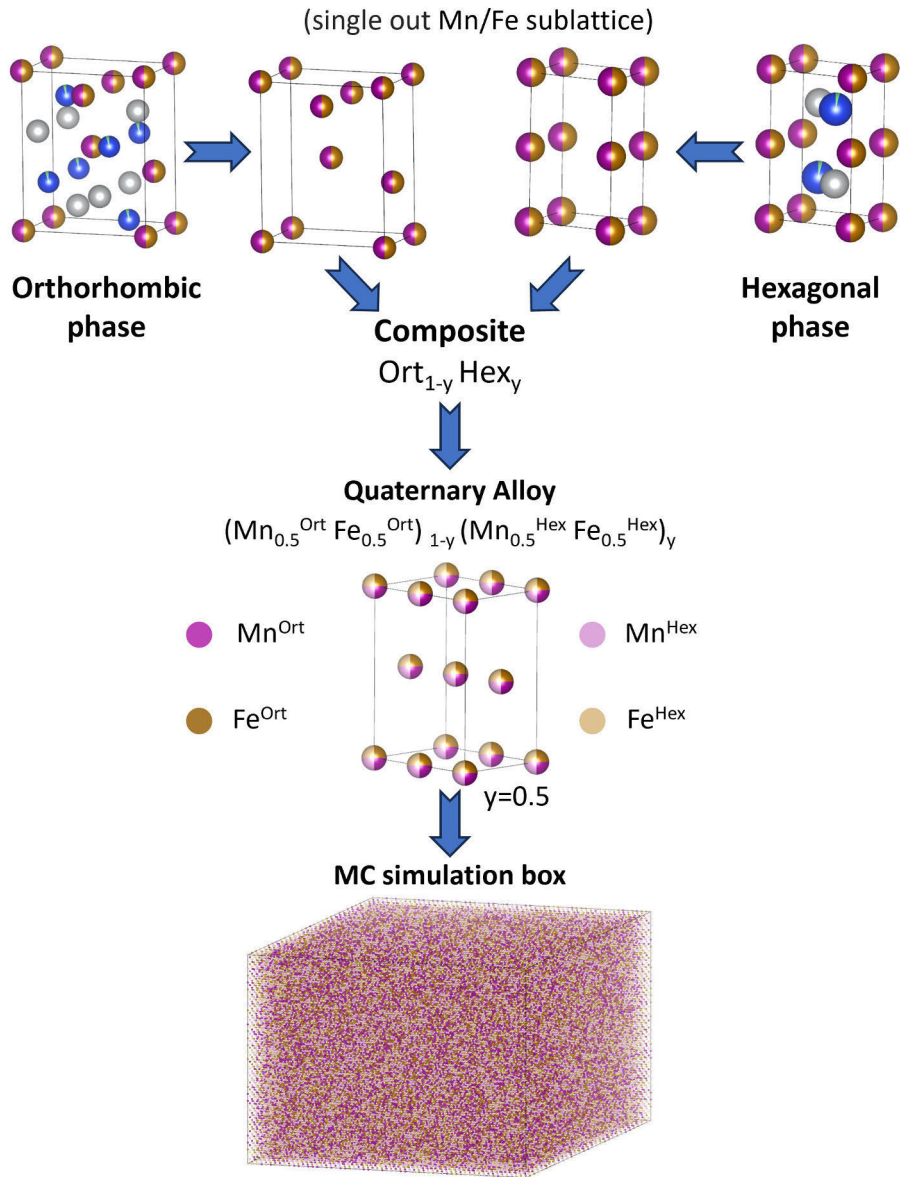


*Figure 6.10.* Schemization of the setup used for the magnetic composite in the Monte Carlo simulations. The colours represent the site occupation by the different chemical elements: Mn (pink), Fe (orange), Ni (grey), Si (blue) and Al (green). The illustrations of the structures were made with VESTA [119]

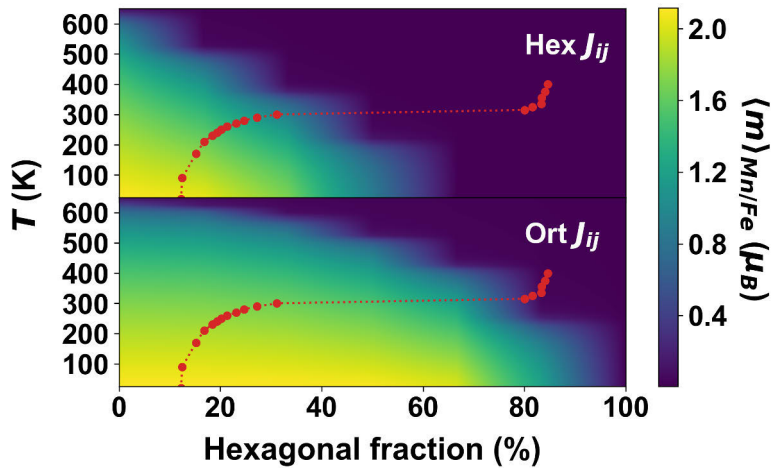


Figure 6.11. Magnetization surface in function of the temperature and the fraction of the hexagonal phase. On the top (bottom) panel are the results from the simulation with the interphase couplings equal to interactions within the orthorhombic (hexagonal) phase. Red circles correspond to the experimental temperature-dependent hexagonal fraction which defines the path taken along the magnetization surface. Adapted from Paper III.

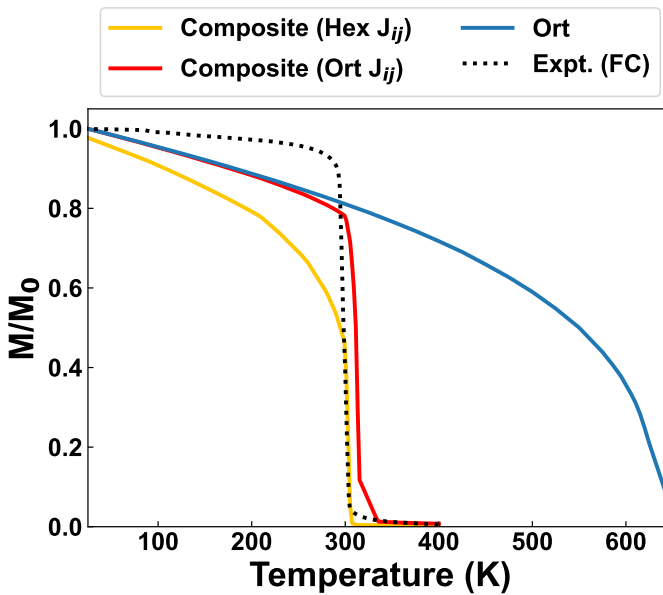


Figure 6.12. Calculated (solid lines) and measured (dotted line) curves for the temperature-dependent normalized magnetization. The results from the MC simulations for the pure orthorhombic (blue) are compared with the results from the magnetic composite combined with the experimental temperature-dependent fraction of the hexagonal phase. The red (yellow) curve is the result of taking the interphase couplings equal to interactions within the orthorhombic (hexagonal) phase. Adapted from Paper III.



magnetic field. The calculated  $\Delta S_{mag}$  of 0.36 J/K/kg contrasts sharply with the total entropy variation measured at 20.2 J/K/kg, indicating a minimal response to the magnetic field. Experimental data validates this small response, with no alteration of  $T_C$  under the application of a magnetic field.

In Paper III, this discrepancy is associated with treating the composition of the composite  $y(T)$  as independent of the magnetic field due to the lack of relevant experimental data. Given the distinct magnetic properties of the phases, it is plausible that the magnetic field could stabilize one phase over the other. While rigorous free energy calculations are necessary for confirmation, it is reasonable to hypothesize that the magnetic field favours the orthorhombic phase, which shows higher magnetization.

To test this conjecture, the  $\Delta S_{mag}$  was calculated in Paper III at the transition temperature  $T_{st}$  (316 K), considering a sharp change in the initial hexagonal fraction  $y$  in the magnetic composite to a final fraction of 84.6%, representative of the high-temperature ( $T > T_{st}$ ) composition:

$$\Delta S_{mag}(T_{st}) = \int_0^{T_{st}} \frac{C_{mag}(T, y = 84.6\%) - C_{mag}(T, y = y_i)}{T} dT . \quad (6.5)$$

This calculation captures the effects of both magnetic field and temperature. With  $y_i=12.2\%$ , the approach mimics a first-order magnetic entropy calculation, similar to the one performed previously for FeRh.

The resulting  $\Delta S_{mag}$  values suggest that sharp changes in the hexagonal fraction significantly impact magnetic entropy. The values are comparable to the total measured entropy variation (around 20 and 50 J/K/kg for magnetic fields of 2T and 5T, respectively), indicating that MCE in this material likely results from the stabilization of one phase over another by an external magnetic field. The fact that substantial  $\Delta S_{mag}$  is generated even for minor shifts in the fraction of the hexagonal phase, corroborates the proposed paradigm since it only relies on the sharpness of the induced structural transformation. Moreover, such behaviour also has practical implications, being advantageous for cyclic applications, as it implies appreciable MCE despite potential hysteresis.

Thus, the mechanism behind the significant MCE observed for the  $\text{Mn}_{0.5}\text{Fe}_{0.5}\text{NiSi}_{0.95}\text{Al}_{0.05}$  compound seems to be the competition between the coexistent hexagonal and orthorhombic phases which possess very distinct magnetic properties. Specifically, the substantial MCE near the first-order structural transition arises from the fact that in a magnetic field one phase is favoured<sup>4</sup>. This, in turn, affects the growth rate and the initial/final fractions of the hexagonal phase. The model introduced in Paper III provides for the first time a relatively straightforward framework for describing the MCE in this compound. A more comprehensive validation of this model can be achieved through free energy calculations and by comparing the temperature-dependent phase fractions measured under various magnetic field strengths. Neverthe-

---

<sup>4</sup>Likely the orthorhombic phase.

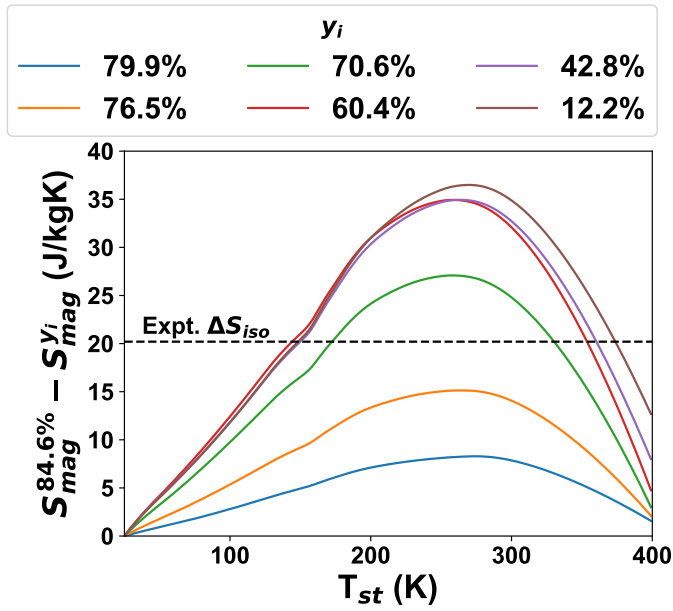


Figure 6.13. Calculated change of magnetic entropy associated with the first-order structural transformation, assuming different initial values of the hexagonal fraction  $y_i$ . The maximal value of 84.6% was fixed for the final hexagonal fraction. Adapted from Paper III.

less, this model contributes toward comprehending the impact of interactions between multiple magnetic phases on the MCE at the atomistic scale.

## 6.4 Remarks

In the systems explored here, the intricate relationship between magnetic properties and structural characteristics is evident. This connection spans from volumetric impacts to minor lattice distortions and encompasses transitions between closely related structures. Particularly in systems exhibiting both AFM and FM interactions in neighbouring shells, we observe that even slight structural variations can significantly amplify the competition between these interactions, leading to notable changes in the magnetic configuration.

While a strong coupling between lattice and structural properties is advantageous for maximizing the magnetocaloric effect  $\Delta S$ , it also introduces a complexity that complicates our understanding and interpretation of calculated and experimental data. This complexity is well exemplified in the case of  $\text{Mn}_{0.5}\text{Fe}_{0.5}\text{NiSi}_{0.95}\text{Al}_{0.05}$ , where integrating experimental and theoretical insights is crucial for comprehending the mechanisms that contribute to a pronounced MCE. This underscores the challenge of predicting the  $\Delta S$  using first-principles calculations without prior information.

## 7. High-throughput Calculations

*The first 90 percent of the code accounts for the first 90 percent of the development time.*

*The remaining 10 percent of the code accounts for the other 90 percent of the development time.*

---

Tom Cargill (aka the ninety-ninety rule)

With the surge in computational capabilities and the growth of extensive databases, high-throughput (HT) calculations have become fundamental in the realm of new materials discovery. This paradigm harnesses the power of vast computational resources, being centred on the rapid evaluation and prediction of properties for a wide dataset of materials. Through effective screening of thousands of potential candidates with screening parameters carefully selected, HT calculations pinpoint those materials most likely to excel in specific applications. In collaboration with experimental validation, this process aims to speed up the discovery of new novel materials. Additionally, the data amassed through HT calculations are crucial for augmenting current databases or establishing new ones [121]. This data production through HT is crucial, particularly for employing techniques like neural networks in materials science.

The success of the computational HT has already been verified for several applications of high technological interest, e.g. in the search of 2D materials [122, 123] and of new permanent magnets [124, 125, 126, 127, 128, 129]. In the search for magnetocaloric materials, various flavours of HT approach have been applied and discussed [130, 131, 132, 133, 134, 28, 133, 135].

Zarkevich et al. (2018) proposed a general approach for an HT-guided search of caloric materials [134]. Their workflow starts with selection criteria based on known properties such as structure and composition. The materials are then screened to determine their physical properties through heuristic fast estimates and ab initio calculations. Later, Zarkevich et al. (2019) discuss the HT approach more specifically in view of magnetocaloric materials, proposing thermodynamic estimates for assessing caloric properties [28]. This work emphasized the entropy change, the isothermal enthalpy change, the transition temperature and respective compositional sensitivity and field dependence.

The calculation of thermodynamic predictors from first principles is a complex and computationally intensive task. This challenge has motivated the search for alternative predictors that could correlate with magnetic entropy variation. For instance, Tantillo et al. (2021) suggested to use the presence of sharp peaks near the Fermi energy as a screening parameter, a potential indicator of itinerant-electron metamagnetism, as observed in MnFe(P,As) alloys and La(Fe,Si)<sub>13</sub> [135, 136].

Examining current promising magnetocaloric materials (Figure 1.2), it becomes evident that the presence of a magnetostructural transition is strongly

beneficial for effective performance. Such transitions imply a strong coupling between magnetic and lattice degrees of freedom, with signatures that can be assessed more easily from first principles. Bocarsly et al. (2017) and Garcia et al. (2020) considered the distortion of the lattice between relaxed structures in magnetic and non-magnetic calculations as a screening parameter, finding it a good correlation with experimental entropy variations [130, 131]. While this approach identifies some potential candidates, it overlooks isostructural transitions, such as those observed in FeRh. In contrast, Batashev et al. (2021) discussed and applied the magnetoelastic response as a screening parameter [133], offering the advantage of encompassing isostructural transitions.

A more direct HT calculation of thermodynamic properties for magnetocaloric materials was performed by Fortunato et al. (2023) [132]. This study concentrated on identifying magnetostructural transitions of the martensite type between orthorhombic and hexagonal structures in  $MM'X$  ( $M/M' = \text{metal}$ ,  $X = \text{main group element}$ ) alloys. It involved calculating structural transformation temperatures (if a transition is present) and magnetic ordering temperatures from first principles.

While the HT studies conducted on magnetocaloric materials have not yet calculated the entropy associated with the MCE to evaluate the material's performance, undertaking these computationally intensive calculations, as previously discussed, would enable a realistic identification of potential candidates. This represents an exciting opportunity for advancing our understanding and application of these materials.

This chapter presents ongoing efforts of a HT calculation to identify new magnetocaloric materials, using as a screening parameter one of the main parameters of the MCE - the entropy variation. A workflow strategically designed for the entropy calculations and preliminary results is briefly presented.

## 7.1 Workflow

In the previous projects, the discussion focused on the performance of the methods to calculate the different entropy contributions of the MCE ( $\Delta S_{ele}$ ,  $\Delta S_{mag}$ ,  $\Delta S_{lat}$ ). This benchmarking provided essential insights for developing an efficient HT workflow to identify new magnetocaloric materials based on entropy variation. The proposed workflow, illustrated in Figure 7.1, consists of three primary stages: initial database screening, followed by the calculation of magnetic properties, and finally, the calculation of  $\Delta S_{lat}$ . The design of this workflow escalates in computational demand, incorporating a screening process at each stage to ensure only the most promising candidates proceed, thus assuring an efficient use of the computational resources.

Applying a HT approach blindly to a vast database is inefficient. The first step in an HT workflow is to narrow the search scope using simple screening parameters [134], allowing for an initial reduction in the dataset without computational effort. For instance, structures might be filtered based on chemical

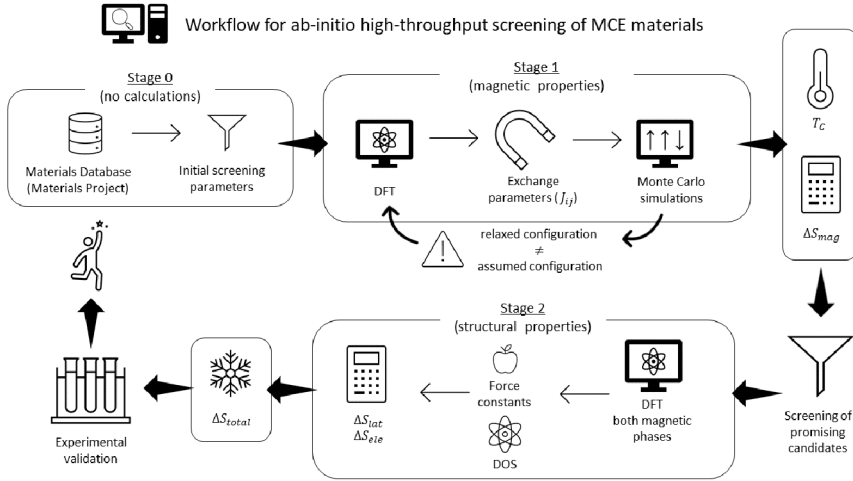


Figure 7.1. Diagram of the high-throughput workflow proposed for the search of magnetocaloric materials.

composition to exclude harmful elements. These parameters can be adjusted if expanding the search space becomes necessary. The choice of database(s) is crucial. In this project, the Materials Project [137] database was considered due to its comprehensive electronic structure data and accessible API, which eases data retrieval. The pre-relaxed structures in this database also eliminate the need to include structural relaxation in the workflow.

Once the search space is defined, the magnetic properties are calculated using the RSPt code, determining local magnetic moments and  $J_{ij}$  (Stage 1 in Figure 7.1). These parameters are then used as input for MC atomistic magnetic simulations in UppASD to find the magnetic ordering temperature and the magnetic entropy contribution under a magnetic field of 2T. These figures serve as criteria for intermediate screening, indicating potential applications and the primary entropy variation.

The magnetic configurations obtained from MC simulations also provide an assessment of the assumed magnetic order in DFT calculations of  $J_{ij}$ . If inconsistencies arise, a thorough analysis of the exchange parameters and configurations helps in hypothesizing the magnetic ordering corresponding to the groundstate in DFT. This iterative approach, while not definitive, aids in identifying the magnetic ground state.

The final stage of the workflow is dedicated to computing the remaining entropy contributions (Stage 2 in Figure 7.1), focusing on  $\Delta S_{lat}$ . This involves calculating the phonon density of states using the Phonopy package and VASP for computing Hellmann-Feynman forces, performed twice for each magnetic phase. The high computational effort required for the phonon calculations is unreasonable for high-throughput calculations, in particular since for each com-

pound, two phases must be considered, and big supercells might be required to describe PM and AFM configurations. Therefore this step is reserved only for candidates that pass the previous screening parameters. From the electronic DOS of both phases,  $\Delta S_{ele}$  is calculated, setting the stage to determine the total  $\Delta S$ .

As evidenced in our benchmark tests (Papers I and II), the model to calculate  $\Delta S$  varies depending on the nature of the transition. In cases of magnetostructural transitions, it is reasonable to assume a first-order transition. However, subsequent experimental measurements should allow us to develop a more tailored model, enhancing our understanding of the associated MCE mechanism.

## 7.2 Screening parameters

In the screening process of a crystallographic database, the chemical composition of the compounds is determined first. First, the focus is on binary ( $MX_1$ ) and ternary ( $MX_1X_2$ ) compounds, where M denotes a magnetic element, essential for inducing or carrying the magnetic properties of the compounds. Due to the criticality associated with rare-earth elements [5], emphasis was on *3d* metals known for magnetism: Cr, Fe, Ni, Mn, and Co<sup>1</sup>. For an initial high-throughput search, the scope is limited to binary and ternary alloys/compounds including *3d*, *4d*, and some *p*-block elements, excluding prohibitively expensive, radioactive, or highly toxic elements like As, Se, Cd, Hg[14], and other heavy-metal elements. Oxide compounds, usually requiring methods beyond DFT for their strongly correlated electronic structures, are not considered in this initial search due to computational constraints. Considering thus the elements highlighted in Figure 7.2, it is obtained a starting dataset with 3050 structures.

Additional screening parameters are then applied to the initial dataset of 3050 structures:

**Space group  $\geq 75$  (3050  $\rightarrow$  1866)** High symmetry structures (cubic, hexagonal, tetragonal) are selected for their enhanced lattice contribution to the entropy variation in magnetostructural transitions and reduced computational efforts. Despite closed-packed structures (bcc, fcc, hcp) tendentially having lower magnetic moments and being less likely associated with potential magnetocalorics [14], their inclusion is justified as known magnetocalorics such as  $Ni_2MnGa$  or  $Gd$  possess these structures. Additionally, magnetocaloric material performance does not necessarily scale with the magnetic moment, as shown in Figure 1.2.

**Energy above hull  $\leq 1000 k_B$  and Formation energy  $\leq 0$  (1866  $\rightarrow$  1071)**

These criteria assess structure stability at 0K, ensuring compounds are bound to form and include structures that become stable up to 1000K, allowing for multiple structures per compound.

---

<sup>1</sup>Co is also a critical element [5], but its partial substitution by Ni and Fe is considered to decrease Co usage

1 1,008 <b>H</b> hydrogen																											
3 6,94 <b>Li</b> lithium																											
11 22,99 <b>Na</b> sodium	12 24,31 <b>Mg</b> magnesium																	5 10,81 <b>B</b> boron	6 12,01 <b>C</b> carbon	7 14,01 <b>N</b> nitrogen							
19 39,10 <b>K</b> potassium	20 40,08 <b>Ca</b> calcium																	13 26,98 <b>Al</b> aluminium	14 28,09 <b>Si</b> silicon	15 30,97 <b>P</b> phosphorus							
		22 47,87 <b>Ti</b> titanium	23 50,94 <b>V</b> vanadium	24 52,00 <b>Cr</b> chromium	25 54,94 <b>Mn</b> manganese	26 55,85 <b>Fe</b> iron	27 58,93 <b>Co</b> cobalt	28 58,69 <b>Ni</b> nickel	29 63,55 <b>Cu</b> copper	30 65,38 <b>Zn</b> zinc	31 69,72 <b>Ga</b> gallium																
		40 91,22 <b>Zr</b> zirconium	41 92,91 <b>Nb</b> niobium	42 95,95 <b>Mo</b> molybdenum																	47 107,9 <b>Ag</b> silver	49 114,8 <b>In</b> indium	50 118,7 <b>Sn</b> tin	51 121,8 <b>Sb</b> antimony			
		57 138,9 <b>La</b> lanthanum																									

Figure 7.2. Periodic table highlighting elements considered in the screening parameters, with magnetic elements in blue.

**Has a magnetic order (1071 → 488)** The MCE requires the system to have a magnetic order. In principle for collinear magnetic orders, only the FiM and FM configurations should display a field-response. However, to include as well possible metamagnetic transitions FiM-AFM or FM-AFM (as for FeRh in Paper I), AFM configurations were also included.

**Number of magnetic sub-lattices > 1 (488 → 345)** A high magnetic moment is important, but a sharp variation at the transition temperature, often linked to multiple magnetic sublattices, is critical for enhanced entropy contribution. This is observable in compounds like FeRh and Fe<sub>2</sub>P [138]. The existence of multiple magnetic sublattices is predicted by analyzing the presence of different magnetic elements or varying coordination numbers of magnetic elements in the composition.

This pool of 345 structures is a promising starting point for new magnetocaloric discoveries, evidenced by the inclusion of known magnetocalorics like La(Fe,Si)<sub>13</sub>, Fe<sub>2</sub>P, and Ni<sub>2</sub>MnGa.

For materials undergoing magnetostructural transitions, an additional requirement is set: at least two structures for the compound must be found in the database. This criterion serves as a rudimentary filter and does not ensure the occurrence of a structural transition. Also, it is partially blind to isostructural transitions, as structural relaxation in the Materials Project database may obscure higher energy phases. Applying this filter results in 34 structures corresponding to 16 different compositions, forming the pool for subsequent calculations.

### 7.3 Preliminary results

Despite the relatively limited scope of structures covered, technical challenges inherent to HT calculations in magnetic systems were encountered [124, 132].



The introduction of magnetic order as a new degree of freedom can lead DFT calculations to local minima, a behaviour more likely in systems with multiple magnetic sub-lattices. This potential issue was accounted for in the workflow design, yet some systems demanded more meticulous approaches to accurately describe their magnetic properties. The discrepancies between calculated and experimental values of  $T_C$  can be seen in Table 7.1. A significant proportion of structures in the pool converged to non-collinear configurations during MC simulations, necessitating further analyses to ascertain whether these configurations are inherent to the structures or a consequence resulting from  $J_{ij}$  being calculated in a metastable configuration in DFT.

Another challenge relates to the data in the database. The structures presented do not always correspond to experimental observations, as compounds with a chemical disorder or vacancies are often modelled in ordered structures. A notable example is MnCoSb, for which the modulation of vacancies in a superstructure was required [139] to correctly determine the  $T_C$ , as shown in Figure 7.3.

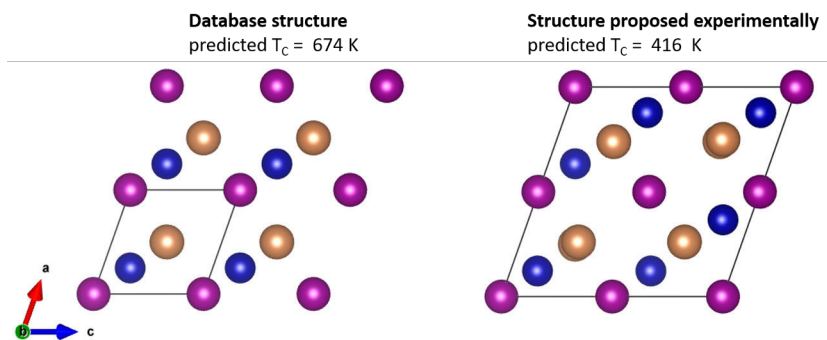


Figure 7.3. Comparison between the experimentally modelled structure for CoMnSb (right) and the idealized structure in the Materials Project database (left). Illustration prepared with VESTA code [119].

The magnetic entropy calculations in Table 7.1 reflect the pure magnetic response of the compounds under a 2T magnetic field application, analogous to calculations performed for Gd (Paper II). This approach excludes the potential for magnetostructural transition, often resulting in a more gradual variation of entropy, as seen in low  $\Delta S_{mag}$  calculated for  $\text{Co}_2\text{NiGa}$ , which in experiments displays high  $\Delta S$  from a sharp magnetic transition [140]. As demonstrated in Table 7.1, such an approach yields mixed results compared to experimental data. This demonstrates one of the primary challenges in high-throughput searches for magnetostructural transitions: many systems require sophisticated modelling to predict  $\Delta S_{mag}$ . However, most  $\Delta S_{mag}$  calculations are within a reasonable order of magnitude.

Classe	Compound	Structure	Magnetic order	$T_C$ (K)	Reported $T_C$ (K)	$\Delta S_{mag}$ (J/K/kg)	Reported $\Delta S_{total}$ (J/K/kg)
Heusler-like	Fe <sub>2</sub> CrAl	cubic	FiM	9	220 [141]	7.76	0.4 [141]
	Fe <sub>2</sub> MnGa	cubic	FiM	36	550 [142]	13.20	4.60 [142]
	Co <sub>2</sub> NiGa	tetragonal	FM	396	325 [140]	1.95	10.5 [140]
	Ni <sub>2</sub> FeGa	cubic	FM	225	430 [143]	2.47	3.7 [144]
	Ni <sub>2</sub> MnGa	cubic	FM	375	363 [145]	1.98	1.81 [146]
	Al <sub>2</sub> FeCo	cubic	FM	114	-	4.74	-
	MnCoSb	super structure	FM	416	474 [147]	2.04	2.06 [147]
	(Zr <sub>0.5</sub> Nb <sub>0.5</sub> )Fe <sub>2</sub>	cubic	FiM	361	PM	1.77	-
Others	LaMn <sub>0.75</sub> Sb <sub>2</sub>	tetragonal	AFM	116 (Néel)	-	0.21	-
	Co <sub>3</sub> Ni	hexagonal	FM	1056	-	0.50	-
	NbNi <sub>2</sub>	cubic	FM	50	-	3.14	-
	MnNi	cubic	FM	525	600 [148]	2.46	-

**Table 7.1.** Summary of results for the magnetic entropy with  $\Delta B=2T$  in magnetically ordered structures at  $T=1K$ .

## 7.4 Remarks and Outlook

Currently, efforts are underway to investigate and fix, where possible, the non-collinear configurations relaxed in MC simulations and discrepancies with experimental results. While some level of disagreement is anticipated in HT calculations within an automated workflow, halting this approach to examine each system in detail helps to optimize the workflow for future searches involving a larger pool of structures. This detailed examination also contributes to the development of more generalized models for calculating entropy in magnetostructural transitions.

Additionally, investigations are being conducted to determine whether the multiple structures identified for each compound are related by a structural transformation and, if so, to identify the low and high-temperature phases. The objective is to estimate  $\Delta S_{mag}$  associated with magnetostructural transitions, akin to the methodology used in Paper III.

Looking ahead, there is an interest in a moderate expansion of the search pool by including additional chemical species or incorporating orthorhombic structures, particularly those with lattice parameter ratios ( $b/a$  or  $c/a$ ) close to 1.0. This expansion aims to accommodate small deformations from tetragonal cells that may occur during structural relaxation, thereby broadening the scope of the search.

The consideration of an additional figure of merit for the MCE, namely  $\Delta T_{adi}$ , is of interest. When examining Equation 2.13, it is evident that calculating  $\Delta T_{adi}$  requires further computation of  $C_{mag}$  in varying magnetic fields<sup>2</sup>. The absence of a straightforward method to accurately compute  $C_{mag}$  across a broad temperature range likely hindered such interest. However, the mixed rescaling scheme introduced in Paper II aids in this effort, and it becomes pertinent to explore the viability of  $\Delta T_{adi}$  as HT screening parameter, and to assess the alignment of such calculations with experimental data. It is important to note that, while first-principle calculations assume isochoric conditions, experimental procedures often occur under isobaric conditions.

---

<sup>2</sup>This assumes the simplest case where  $C_{lat}$  and  $C_{ele}$  are independent of the magnetic field.

## 8. Conclusions

*[we see that] science is eminently perfectible, and that each theory has constantly to give way to a fresh one.*

---

Jules Verne, 'A Journey to the Center of the Earth'

In this thesis, the characterization of magnetocaloric materials is explored through first-principles calculations, with a specific emphasis on the entropy variation associated with the MCE. The focus on entropy arises from its potential as a key screening parameter in high-throughput calculations to search for novel magnetocaloric materials. Magnetocaloric materials of interest typically show a strong interplay between structural and magnetic properties. In light of this, the coupling was studied with different approaches and materials, with the aim of not only refining the theoretical framework of magnetocaloric materials but also deepening the understanding of their physical properties. Additionally, it was developed of a new renormalization scheme for magnetic Monte Carlo simulations. This advancement is noteworthy for enhancing the precision of these simulations over a wide temperature range.

The benchmarking of the calculations associated with the entropy contributions in the magnetocaloric effect involved analyses of two distinct systems: FeRh and Gd, as detailed in Papers I and II, respectively. FeRh undergoes a first-order metamagnetic antiferromagnetic-ferromagnetic (AFM-FM) transition, whereas Gd exhibits a conventional second-order ferromagnetic-paramagnetic (FM-PM) transition. In FeRh, the entropy change was calculated by comparing the entropies of the high-temperature and low-temperature phases, excluding the impact of the magnetic field. Conversely, the second-order transition in Gd necessitated a different approach. Here,  $\Delta S$  was determined through a gradual process that incorporated the effects of the magnetic field. The validity of these procedures is supported by their close alignment with experimental data. Additionally, a similar calculation of the first-order transition was applied to the  $\text{Mn}_{0.5}\text{Fe}_{0.5}\text{NiSi}_{0.95}\text{Al}_{0.05}$  system (discussed in Paper III). This analysis successfully predicted  $\Delta S_{mag}$  values that are in the same order of magnitude as the experimental observations.

The results of the tests presented in Papers I and II reveal distinct vibrational properties in the magnetic phases involved in the magnetic transition explored by the MCE. These properties significantly influence the lattice contribution to the entropy, as demonstrated in both studies. As a consequence, it becomes essential to calculate the vibrational properties of the various magnetic phases to accurately estimate the lattice contribution to the entropy change. Moreover, the effect of alterations of the structure on the magnetic properties was also investigated. Notably, Paper II explores this relationship in the

context of pressure-induced polymorphs in Gd. Similarly, Paper III examines  $\text{Mn}_{0.5}\text{Fe}_{0.5}\text{NiSi}_{0.95}\text{Al}_{0.05}$ , focusing on the interplay of coexistent structural phases. In the case of Gd, it was concluded that variations in magnetic ordering temperature under pressure could be explained through a model based on the formation and accumulation of stacking faults, describing a gradual transition between structures. For the  $\text{Mn}_{0.5}\text{Fe}_{0.5}\text{NiSi}_{0.95}\text{Al}_{0.05}$  system, the adoption of a magnetic composite model, in conjunction with experimental data, allowed to determine that the magnetostructural transition in these compounds is predominantly driven by the lattice subsystem. The observed collapse in magnetization is attributed not to a typical FM $\rightarrow$ PM transition but to a sharp phase transition between low and high-temperature phases, each exhibiting distinctly different magnetic properties.

The insight obtained from these projects led to the development of a systematic workflow for estimating entropy in a high-throughput manner. This workflow incorporates additional screening parameters designed to limit the pool of materials and reduce the computational effort. The initial results obtained from implementing this workflow have been mixed when compared with existing experimental data. This inconsistency suggests that certain systems may require a more careful approach. In response to these preliminary findings, current efforts are focused on investigating these specific cases. The aim is to refine the accuracy of the calculated quantities and to gain insights into further routines that need to be integrated into the workflow, to handle in a more systematic way complex systems.

The findings presented in this thesis allow us to affirm the feasibility of using first-principles estimates of the entropy change related to the MCE as an effective screening tool in high-throughput studies. This conclusion is supported by the close correlation observed between the calculated and experimental data for the studied systems. Note that these results were obtained using general methodologies that are readily adaptable across different systems. It is crucial to note, however, that while the employed models were not specifically tailored for each material, they were carefully selected to align with the characteristics of the magnetic(-structural) transitions being investigated. For instance, FeRh and  $\text{Mn}_{0.5}\text{Fe}_{0.5}\text{NiSi}_{0.95}\text{Al}_{0.05}$  were analyzed as first-order transitions, while Gd was treated as a second-order transition. This distinction underscores a potential limitation in high-throughput studies since the nature of a material's transition may not be known in advance. To address this challenge, two strategies emerge: either conducting estimates for both first-order and second-order transitions for each candidate material or narrowing the focus to a specific family of compounds. This latter approach assumes that these compounds share similar characteristics and can be effectively modelled using a systematic approach.

Finally, the scaling scheme introduced in Paper II presents a promising improvement for conventional Monte Carlo simulations. Since it effectively allows to capture the correct behaviour of equilibrium properties across two critical temperature limits: at temperatures approaching zero, where quantum statis-

tics governed by the Bose-Einstein distribution are dominant, and near the magnetic ordering temperature, where classical statistics, as dictated by the Boltzmann distribution, prevail. In its essence, the proposed scheme interpolates between these two statistical distributions using a mixing function, which, in Paper II, is represented as a linear function of temperature. It is important to highlight that the choice of this linear relationship was primarily for its simplicity and does not stem from underlying physical principles. In the future would be interesting to apply this scaling scheme to many other magnetic systems. Such exploration could potentially reveal whether a universal mixing function exists, one that could be also formally derived from theoretical principles. This would offer deeper insight into the underlying physics of the proposed scheme. Furthermore, extending this scaling scheme to spin-dynamics simulations and evaluating its efficacy there would also be an interesting endeavour.

# Popular Science Summary

Since the dawn of civilization, humans have harnessed the properties of materials found in nature like wood, stone, and wool to make their lives easier. We have not only utilized these natural resources for various purposes, but also developed new materials such as pottery, bronze, and steel. Today, our search for groundbreaking materials, particularly for energy-efficient technologies, is more intense than ever. A prime example of this innovation is in the realm of cooling and refrigeration technology.

In the pursuit of sustainable and efficient cooling methods, researchers are focusing on a novel class of materials called magnetocaloric materials. These materials demonstrate a significant and reversible thermal response when exposed to external magnetic fields. Their potential as a greener alternative for cooling technologies is particularly exciting.

The magnetocaloric effect is a phenomenon where a material's temperature changes in response to alterations in an external magnetic field. While typically subtle, this effect is markedly stronger in magnetocaloric materials near a phase transition, where their magnetic properties shift. This phenomenon is the basis for magnetic refrigeration, a technology leveraging the magnetocaloric effect in a thermodynamic cycle for cooling, offering an eco-friendly alternative to traditional vapour-compression methods. This technology is already used at cryogenic temperatures, but in the last two decades, there has been an increasing effort to apply it in room-temperature devices. Despite its promise of efficient (with a performance increase of 30% compared to traditional devices) cooling, adapting this technology for domestic use poses significant engineering challenges. Currently, this technology is being refined, with one of the main focuses in the search for the ideal magnetocaloric materials that are efficient, cost-effective, and environmentally benign for household applications. Ongoing research, including extensive large-scale computational studies, is key to advancing more efficient, affordable, and environmentally friendly cooling technologies. This exploration not only paves the way for integrating magnetic refrigeration into everyday life but also deepens our understanding of these unique materials.

This thesis explores the complex world of magnetocaloric materials, focusing on entropy variation linked to the magnetocaloric effect using ab-initio calculations. This approach has refined theoretical models for large-scale calculations and enhanced our understanding of the physical properties of these materials. The primary focus is on investigating the properties of FeRh and Gd, well-established magnetocaloric materials, and  $\text{Mn}_{0.5}\text{Fe}_{0.5}\text{NiSi}_{0.95}\text{Al}_{0.05}$ , an emerging candidate for room-temperature refrigeration applications.

The study closely analyzed FeRh and Gd, each exhibiting distinct magnetic transitions. FeRh shows a first-order transition with abrupt property changes, while Gd displays a second-order transition with a more gradual change. These

analyses provided vital insights into calculating entropy variation accurately and confirmed the strong coupling between magnetic and structural properties in these materials. This interplay was especially crucial in understanding the magnetocaloric effect in  $\text{Mn}_{0.5}\text{Fe}_{0.5}\text{NiSi}_{0.95}\text{Al}_{0.05}$ , where the magnetic characteristics are influenced by two coexistent structural phases with different magnetic properties.

Building on the findings from FeRh and Gd, the thesis developed a systematic workflow for high-throughput estimation of entropy changes. This method is essential for screening potential magnetocaloric materials, though ongoing studies indicate the need for more nuanced approaches in complex systems.

In parallel, the thesis presents a novel correction scheme for Monte Carlo simulations, a prominent method for simulating magnetic systems. In its conventional formulation, the method performs poorly for simulations at low temperatures. This correction builds up on top of similar corrections by rescaling the effective temperature in simulations to accurately reflect statistical distributions at low temperatures, where quantum behaviour dominates, and at high temperatures, governed by classical physics.

The research presented in this thesis highlights the potential of using ab-initio estimates of entropy change to identify promising magnetocaloric materials. As the global demand for environmentally friendly alternatives grows, the study of magnetocaloric materials becomes increasingly critical, holding the promise of a cooler, more sustainable future.



# Populärvetenskaplig sammanfattning

Sedan civilisationens gryning har människan utnyttjat egenskaperna hos material som finns i naturen, som trä, sten och ull, för att göra livet enklare. Vi har inte bara använt dessa naturresurser för olika ändamål utan också utvecklat nya material som keramik, brons och stål. Idag är vår jakt på banbrytande material, särskilt för energieffektiva teknologier, intensivare än någonsin. Ett viktigt exempel på denna innovation finns inom kyl- och värmeteknik.

I strävan efter hållbara och effektiva kylmetoder fokuserar forskare på en ny klass av material som kallas magnetokaloriska material. Dessa material uppvisar en betydande och reversibel termisk respons när de utsätts för yttre magnetfält. Deras potential som ett grönare alternativ för kylteknik är särskilt spännande.

Magnetokalorisk effekt är ett fenomen där ett materials temperatur ändras som svar på förändringar i ett yttre magnetfält. Även om effekten vanligtvis är liten, är den markant starkare i magnetokaloriska material nära en fasövergång, där deras magnetiska egenskaper förändras. Detta fenomen är grunden för magnetisk kylning, en teknik som utnyttjar magnetokalorisk effekt i en termodynamisk cykel för kylning, och erbjuder ett miljövänligt alternativ till traditionella vätska-gas-cykler. Magnetokalorisk teknik används redan vid kryogeniska temperaturer, men under de senaste två decennierna har ökade ansträngningar gjorts för att tillämpa den vid rumstemperatur. Trots att tekniken utlovar prestandaökningar på upp till 30% jämfört med traditionella enheter, finns betydande utmaningar då den ska anpassas för hushållsbruk. För närvarande är ett av huvudfokuset sökandet efter idealiska magnetokaloriska material som är effektiva, kostnadseffektiva och miljövänliga för hushållsapplikationer. Pågående forskning, inklusive omfattande storskaliga beräkningsstudier, är avgörande för att utveckla mer effektiva, prisvärda och miljövänliga kylteknologier. Detta banar inte bara väg för integration av magnetisk kylning i vardagslivet, utan fördjupar också vår förståelse av dessa fascinerande material.

Denna avhandling utforskar de magnetokaloriska materialens komplexa värld, med fokus på entropivariationen kopplad till den magnetokaloriska effekten med ab initio-beräkningar. Teoretiska modeller för storskaliga beräkningar har förfinats och förbättrat vår förståelse för de fysikaliska egenskaperna hos dessa material. Primärt undersöks egenskaperna hos FeRh och Gd, väl etablerade magnetokaloriska material, samt  $Mn_{0.5}Fe_{0.5}NiSi_{0.95}Al_{0.05}$ , en kandidat för kylning vid rumstemperatur.

Studien analyserade noggrant FeRh och Gd, som båda uppvisar distinkta magnetiska övergångar. FeRh har en första ordningens övergång med abrupta egenskapsförändringar, medan Gd har en andra ordningens övergång med mer gradvis förändring. Dessa analyser gav insikter i hur entropivariationen kan beräknas med större precision och bekräftade det starka sambandet mellan

magnetiska och strukturella egenskaper i dessa material. Denna växelverkan var särskilt avgörande för att förstå den magnetokaloriska effekten i  $\text{Mn}_{0.5}\text{Fe}_{0.5}\text{NiSi}_{0.95}\text{Al}_{0.05}$ , där de magnetiska egenskaperna påverkas av två samexisterande strukturella faser med olika magnetiska egenskaper.

Med utgångspunkt i fynden från FeRh och Gd utvecklar avhandlingen ett systematiskt arbetsflöde för högkapacitetsberäkning av entropiförändringar. Denna metod är avgörande för att screena potentiella magnetokaloriska material, även om pågående studier tyder på ett behov av mer nyanserade tillvägagångssätt i komplexa system.

Dessutom presenterar avhandlingen ett nytt korrigeringschema för Monte Carlo-simuleringar, en kraftfull metod för att simulera magnetiska system. I dess konventionella formulering presterar metoden dåligt för simuleringar vid låga temperaturer. Korrigeringen bygger på tidigare föreslagna skeman för att justera den effektiva temperaturen i simuleringarna för att korrekt återspegla den statistiska distributionen vid låga temperaturer, där kvantmekaniskt beteende dominerar, och vid höga temperaturer, som styrs av klassisk fysik.

Forskningen som presenteras i denna avhandling lyfter fram möjligheten att använda ab initio-uppskattningar av entropiförändring för att identifiera lovande magnetokaloriska material. I takt med att den globala efterfrågan på miljövänliga alternativ växer, blir studiet av magnetokaloriska material allt viktigare, med löften om en svalare, mer hållbar framtid.

# Acknowledgments

*While it is always best to believe in oneself, a little help from others can be a great blessing*

---

Uncle Iroh, 'Avatar: The Last Airbender'

During this journey till and during my PhD and thesis, I had the support, on scientific and a personal level, of many wonderful people. Here I would like to extend my heartfelt thanks to them!

The calculation of entropy contributions can become somehow chaotic. Making sense of this disorder would have been hopeless without the guidance of my supervisors Heike, Olle and Torbjörn. I am tremendously grateful for their help, availability, encouragement, and infinite patience in this process. Whether discussing science or more casual topics, our conversations were often inspiring and fruitful. I believe I improved as a person under your mentoring.

I would like to give a special thanks to Heike, who guided me under her wing throughout the whole PhD, and so many times had to translate my words (written and spoken) into something clear to the rest of the world. Thank you for your efforts to keep me with my feet on the ground; without them, I would probably take a lifetime to finish the PhD. Whenever calculations went wrong, and they did a lot, I could always count on your expertise to figure it out and solve it. Also, I would like to thank you very much, Olle, for your inspired ideas, for your uplifting optimism and for giving me the opportunity to extend my PhD. Despite your busy agenda, you were always available to discuss. Certainly not least, thank you, Torbjörn, for guiding me through the Finnish system (somehow I always got lost in the Åbo Akademi procedures). Your enthusiasm for exploring new methods is contagious! Thank you very much for reassuring me during the stressful last weeks of the thesis preparation.

A shout-out to ma'am Alena, your constant teasing certainly renovates each week's conversation. A big thank you for your kin-like friendship, all the help, and all the chocolates!

Thank you, Henrik, for trusting me as a mentor for your master's thesis, and for all the nice explanations and tips on Finnish culture - although I will disagree promptly about what are good pancakes.

In this work, a fair amount of different methods and software were used in the calculations performed. Thanks to the precious help of the local experts, Yaroslav ( $J_{ij}$ ), Anders (UppASD code), Erna (EMTO code), Vladislav ( $J_{ij}$  and generalized susceptibility), Patrik (RSPT code), Chin (Quantum Espresso), and Diana (RSPT and UppASD) who patiently provided the resources and/or the know-how. Thanks to you it was easier to learn how to do these calculations.

I extend my gratitude to my collaborators Anders, Erna, and Sergei for the insightful scientific discussions, their dedication to our joint efforts, and their

skill in reasoning complex concepts in a pedagogical way. Their expertise was integral to the development of this research. Similarly, the expertise of my experimental collaborators, Peter Svedlindh, Sagar, Vitalii, Martin, Ridha, Lei, Peter Lazor, and Mahmoud, was equally vital. I am deeply appreciative of their contributions in offering diverse perspectives on our research challenges and for their assistance in helping me interpret experimental results - physics only happens when experiments and theory walk side by side. I wish to express my appreciation for Ondřej, whose passion for science and inherent kindness were truly inspiring. His ability to explain the complexities of the SPR-KKR method so didactically was invaluable to my understanding. His passing has left a profound impact, and his absence is deeply felt.

Thanks to Olga, Duo, and Ángel for the friendly environment in the office and also for the fun and interesting discussions. Also, I am grateful for the exchanged treats/snacks - you expanded my gastronomical knowledge! Duo, Ángel, more than office mates you are great friends. Thank you for your kindness, for lightening the mood, and for all the coffee/tea breaks!

During these five years, I had the opportunity to meet so many wonderful people in the Material Theory division in Uppsala and the physics division in Åbo. No matter the season, there was always a friendly face around. I want to thank you all for the laughs, and the exciting discussions. I would like to thank Ivan and Ralph for the great suggestions of trying different functions for the mixing factor on Mixed Monte Carlo. Some of you were already mentioned, so I will just quickly shout-out to Raquel, Fabian, Misha, Pablo, Felix, Madhura, Rodrigo, and Renan. Thank you!

In the cold of the winter or in the brightness of the summer, I could always count on the smile and support of Miora, Philipp, Zahra, Reza, Nacho, Nastya, Pier and Fernand. Thank you for always being there, and for the wonderful memories.

It is very hard to imagine my journey in physics, or even life, without my 'Sexy Bitches' and my 'Brohs'. I'm forever indebted for your friendship. Your company and support are the most precious to me, and I am immensely thankful to you for all the time we spend together. Let more stories be made with you! A big thanks to Isabel, Carolina and Ana; we started this journey together and we kept going across seas and borders. You were always there for me! Thank you so much, little brohs Leandro and Paul - champions of the rift, first of their names! You taught me so much, and your enthusiasm is contagious! Go Go Go!

Paraphrasing my favourite musical: 'There is life outside of Academia! I know that is hard to conceive'. Thus, I would like to thank my friends outside academia, who keep me sane and in the real world. Thank you (Sla)Vanda(la) and Wuyihan for your friendship and patience. Your laugh fills the world with joy.

I would also like to extend my heartfelt thanks to David and André, my foster 'cousins' in metropolitan Stockholm. You made Sweden feel like home

for me, and I consider you as my expat family. Your kindness and support have been invaluable.

Last but not least, in Sweden, I would like to give my deepest thanks to Matías, my 'sambo', for filling my life with happiness and providing unwavering support and patience! These past months have been challenging, but knowing that you are there to offer a comforting embrace when things get tough has been my rock. I am profoundly grateful for everything you do for me.

Moving country, I would like to thank my dear friends Joana, Sofia, Jé, Ana Isabel, Jessica, Nuno, and Kita. I always look forward to visiting you or for your visit! Your friendship means the world to me.

Lastly, I would like to thank my family for your support; it is thanks to you I have reached so far. Thank you for your patience and understanding, especially in light of my prolonged absences. Your support has been the cornerstone of this journey.

This work was supported by the Swedish Foundation for Strategic Research, within the project Magnetic Materials for Green Energy Technology (ref. EM16-0039), StandUp, eSENCE, Vetenskapsrådet, and Energimyndigheten, the Magnus Ehrnrooth Foundation, the Swedish Research Council (VR), Liljewalch's travel scholarship, and Anna Maria Lundin's scholarship from Smålands nation. The computations performed in this work were enabled by resources provided by the CSC – IT Center for Science, Finland, and by the Swedish National Infrastructure for Computing (SNIC) at NSC and PDC centres.

# Bibliography

- [1] BMWK, “Gesamtausgabe der energiedaten,” tech. rep., Berlin, 2022.
- [2] EIA, “Residential energy consumption survey,” tech. rep., Washington, DC, 2020.
- [3] EMSD, “Hong kong energy end-use data,” tech. rep., Hong Kong, 2021.
- [4] IEA, “The future of cooling,” tech. rep., Paris, May 2018. License: CC BY 4.0.
- [5] O. Gutfleisch, M. A. Willard, E. Brück, C. H. Chen, S. G. Sankar, and J. P. Liu, “Magnetic Materials and Devices for the 21st Century: Stronger, Lighter, and More Energy Efficient,” *Advanced Materials*, vol. 23, pp. 821–842, 2 2011.
- [6] K. A. Gschneidner and V. K. Pecharsky, “Magnetocaloric Materials,” *Annual Review of Materials Science*, vol. 30, pp. 387–429, 8 2000.
- [7] A. Smith, “Who discovered the magnetocaloric effect?,” *Eur. Phys. J. H*, vol. 38, pp. 507–517, 9 2013.
- [8] P. Weiss and A. Piccard, “Le phénomène magnétocalorique,” *J. Phys. Theor. Appl.*, vol. 7, no. 1, pp. 103–109, 1917.
- [9] V. Franco, J. S. Blázquez, J. J. Ipus, J. Y. Law, L. M. Moreno-Ramírez, and A. Conde, “Magnetocaloric effect: From materials research to refrigeration devices,” *Progress in Materials Science*, vol. 93, pp. 112–232, 4 2018.
- [10] F. Cugini and M. Solzi, “On the direct measurement of the adiabatic temperature change of magnetocaloric materials,” *Journal of Applied Physics*, vol. 127, p. 123901, 3 2020.
- [11] A. Chirkova, K. Skokov, L. Schultz, N. Baranov, O. Gutfleisch, and T. Woodcock, “Giant adiabatic temperature change in FeRh alloys evidenced by direct measurements under cyclic conditions,” *Acta Materialia*, vol. 106, pp. 15–21, 3 2016.
- [12] A. Kitanovski and A. Kitanovski, “Energy Applications of Magnetocaloric Materials,” *Advanced Energy Materials*, vol. 10, p. 1903741, 3 2020.
- [13] M. M. Cruz, L. P. Ferreira, A. F. Alves, S. G. Mendo, P. Ferreira, M. Godinho, and M. D. Carvalho, “Chapter 19 - nanoparticles for magnetic hyperthermia,” in *Nanostructures for Cancer Therapy* (A. Ficaí and A. M. Grumezescu, eds.), Micro and Nano Technologies, pp. 485–511, Elsevier, 2017.
- [14] N. A. Zarkevich and V. I. Zverev, “Viable Materials with a Giant Magnetocaloric Effect,” *Crystals*, vol. 10, p. 815, 9 2020.
- [15] R. A. Kishore and S. Priya, “A review on design and performance of thermomagnetic devices,” *Renewable and Sustainable Energy Reviews*, vol. 81, pp. 33–44, 1 2018.
- [16] J. Romero Gómez, R. Ferreira Garcia, A. De Miguel Catoira, and M. Romero Gómez, “Magnetocaloric effect: A review of the thermodynamic cycles in magnetic refrigeration,” *Renewable and Sustainable Energy Reviews*, vol. 17, pp. 74–82, 1 2013.
- [17] E. Brück, “Chapter Four Magnetocaloric Refrigeration at Ambient Temperature,” in *Handbook of Magnetic Materials*, vol. 17, pp. 235–291, Elsevier, 1 2007.
- [18] B. Yu, Q. Gao, B. Zhang, X. Meng, and Z. Chen, “Review on research of room temperature magnetic refrigeration,” *International Journal of Refrigeration*, vol. 26, pp. 622–636, 9 2003.

- [19] W. J. De Haas, E. C. Wiersma, and H. A. Kramers, “Experiments on adiabatic cooling of paramagnetic salts in magnetic fields,” *Physica*, vol. 1, pp. 1–13, 1 1934.
- [20] P. Debye, “Einige Bemerkungen zur Magnetisierung bei tiefer Temperatur,” *Annalen der Physik*, vol. 386, pp. 1154–1160, 1 1926.
- [21] W. F. Giauque, “A thermodynamic treatment of certain magnetic effects. A proposed method of producing temperatures considerably below 1° absolute,” *Journal of the American Chemical Society*, vol. 49, pp. 1864–1870, 8 1927.
- [22] G. V. Brown, “Magnetic heat pumping near room temperature,” *Journal of Applied Physics*, vol. 47, pp. 3673–3680, 8 1976.
- [23] V. K. Pecharsky and K. A. Gschneidner, “Giant magnetocaloric effect in Gd<sub>5</sub>(Si<sub>2</sub>Ge<sub>2</sub>),” *Physical Review Letters*, vol. 78, pp. 4494–4497, 6 1997.
- [24] K. Gschneidner and V. Pecharsky, “Thirty years of near room temperature magnetic cooling: Where we are today and future prospects,” *International Journal of Refrigeration*, vol. 31, pp. 945–961, 9 2008.
- [25] F. Scheibel, T. Gottschall, A. Taubel, M. Fries, K. P. Skokov, A. Terwey, W. Keune, K. Ollefs, H. Wende, M. Farle, M. Acet, O. Gutfleisch, and M. E. Gruner, “Hysteresis Design of Magnetocaloric Materials—From Basic Mechanisms to Applications,” *Energy Technology*, vol. 6, pp. 1397–1428, 8 2018.
- [26] K. G. Sandeman, “Magnetocaloric materials: The search for new systems,” *Scripta Materialia*, vol. 67, pp. 566–571, 9 2012.
- [27] T. Gottschall, K. P. Skokov, M. Fries, A. Taubel, I. Radulov, F. Scheibel, D. Benke, S. Riegg, and O. Gutfleisch, “Making a Cool Choice: The Materials Library of Magnetic Refrigeration,” *Advanced Energy Materials*, vol. 9, p. 1901322, 9 2019.
- [28] N. A. Zarkevich and D. D. Johnson, “Reliable thermodynamic estimators for screening caloric materials,” *Journal of Alloys and Compounds*, vol. 802, pp. 712–722, 9 2019.
- [29] V. Franco, J. Blázquez, B. Ingale, and A. Conde, “The Magnetocaloric Effect and Magnetic Refrigeration Near Room Temperature: Materials and Models,” *Annual Review of Materials Research*, vol. 42, no. 1, pp. 305–342, 2012.
- [30] J. Y. Law, □. Díaz-García, L. M. Moreno-Ramírez, and V. Franco, “Increased magnetocaloric response of FeMnNiGeSi high-entropy alloys,” *Acta Materialia*, vol. 212, p. 116931, 6 2021.
- [31] Y. Yuan, Y. Wu, X. Tong, H. Zhang, H. Wang, X. J. Liu, L. Ma, H. L. Suo, and Z. P. Lu, “Rare-earth high-entropy alloys with giant magnetocaloric effect,” *Acta Materialia*, vol. 125, pp. 481–489, 2 2017.
- [32] J. Y. Law, V. Franco, L. M. Moreno-Ramírez, A. Conde, D. Y. Karpenkov, I. Radulov, K. P. Skokov, and O. Gutfleisch, “A quantitative criterion for determining the order of magnetic phase transitions using the magnetocaloric effect,” *Nature Communications*, vol. 9, pp. 1–9, 12 2018.
- [33] O. Gutfleisch, T. Gottschall, M. Fries, D. Benke, I. Radulov, K. P. Skokov, H. Wende, M. Gruner, M. Acet, P. Entel, and M. Farle, “Mastering hysteresis in magnetocaloric materials,” *Philosophical Transactions of the Royal Society A: Mathematical, Physical and Engineering Sciences*, vol. 374, 8 2016.
- [34] T. Gottschall, A. Gràcia-Condal, M. Fries, A. Taubel, L. Pfeuffer, L. Mañosa, A. Planes, K. P. Skokov, and O. Gutfleisch, “A multicaloric cooling cycle that

- exploits thermal hysteresis,” *Nature Materials*, vol. 17, pp. 929–934, 9 2018.
- [35] D. Y. Karpenkov, A. Y. Karpenkov, K. P. Skokov, I. A. Radulov, M. Zheleznyi, T. Fasse, and O. Gutfleisch, “Pressure Dependence of Magnetic Properties in  $\text{La}(\text{Fe}, \text{Si})_{13}$ : Multistimulus Responsiveness of Caloric Effects by Modeling and Experiment,” *Physical Review Applied*, vol. 13, p. 034014, 3 2020.
- [36] S. J. Blundell and K. M. Blundell, *Concepts in Thermal Physics*, vol. 9780199562. Oxford University Press Oxford, 10 2010.
- [37] J. Lyubina, “Magnetocaloric Materials,” in *Springer Series in Materials Science*, vol. 231, pp. 115–186, 2016.
- [38] V. K. Pecharsky, K. A. Gschneidner, A. O. Pecharsky, and A. M. Tishin, “Thermodynamics of the magnetocaloric effect,” *Physical Review B*, vol. 64, p. 144406, 9 2001.
- [39] A. M. Tishin and Y. I. Spichkin, *The Magnetocaloric Effect and its Applications*. IOP Publishing Ltd, 2003.
- [40] E. J. Woll and W. Kohn, “Images of the Fermi Surface in Phonon Spectra of Metals,” *Physical Review*, vol. 126, pp. 1693–1697, 6 1962.
- [41] B. Fultz, “Vibrational thermodynamics of materials,” *Progress in Materials Science*, vol. 55, pp. 247–352, 5 2010.
- [42] G. Grimvall, *Thermophysical properties of materials*. Elsevier, 1999.
- [43] P. J. v. Ranke, N. A. de Oliveira, C. Mello, A. M. G. Carvalho, S. Gama, P. J. Von Ranke, N. A. de Oliveira, C. Mello, A. M. G. Carvalho, and S. Gama, “Analytical model to understand the colossal magnetocaloric effect,” *Physical Review B*, vol. 71, p. 054410, 2 2005.
- [44] L. Jia, G. J. Liu, J. R. Sun, H. W. Zhang, F. X. Hu, C. Dong, G. H. Rao, and B. G. Shen, “Entropy changes associated with the first-order magnetic transition in  $\text{LaFe}_{13-x}\text{Si}_x$ ,” *Journal of Applied Physics*, vol. 100, p. 123904, 12 2006.
- [45] A. Lichtenstein, “Magnetism: From Stoner to Hubbard,” *Emergent Phenomena in Correlated Matter*, 2013.
- [46] P. Mohn, *Magnetism in the Solid State*, vol. 134 of *Solid-State Sciences*. Berlin/Heidelberg: Springer-Verlag, 2006.
- [47] R. McMichael, R. Shull, L. Swartzendruber, L. Bennett, and R. Watson, “Magnetocaloric effect in superparamagnets,” *Journal of Magnetism and Magnetic Materials*, vol. 111, pp. 29–33, 6 1992.
- [48] P. Hohenberg and W. Kohn, “Inhomogeneous electron gas,” *Physical Review*, vol. 136, p. B864, 11 1964.
- [49] R. M. Martin, *Electronic Structure*. Cambridge University Press, 4 2004.
- [50] J. M. Wills, O. Eriksson, P. Andersson, A. Delin, O. Grechnev, and M. Alouani, *Full-Potential Electronic Structure Method*, vol. 167 of *Springer Series in Solid-State Sciences*. Berlin, Heidelberg: Springer Berlin Heidelberg, 2010.
- [51] W. Kohn and L. J. Sham, “Self-consistent equations including exchange and correlation effects,” *Physical Review*, vol. 140, p. A1133, 11 1965.
- [52] O. K. Andersen, P. M. Marcus, J. F. Janak, and A. R. Williams, *Computational Methods in Band Theory*. Boston, MA: Springer US, 1971.
- [53] O. K. Andersen, “Linear methods in band theory,” *Physical Review B*, vol. 12, pp. 3060–3083, 10 1975.
- [54] J. Korringa, “On the calculation of the energy of a Bloch wave in a metal,”



- Physica*, vol. 13, pp. 392–400, 8 1947.
- [55] W. Kohn and N. Rostoker, “Solution of the Schrödinger Equation in Periodic Lattices with an Application to Metallic Lithium,” *Physical Review*, vol. 94, p. 1111, 6 1954.
- [56] D. Sébilleau, K. Hatada, and H. Ebert, *Multiple Scattering Theory for Spectroscopies*, vol. 204 of *Springer Proceedings in Physics*. Cham: Springer International Publishing, 2018.
- [57] H. Ebert, D. Ködderitzsch, and J. Minár, “Calculating condensed matter properties using the KKR-Green’s function method - Recent developments and applications,” 9 2011.
- [58] P. E. Blöchl, “Projector augmented-wave method,” *Physical Review B*, vol. 50, pp. 17953–17979, 12 1994.
- [59] G. Kresse and J. Hafner, “Norm-conserving and ultrasoft pseudopotentials for first-row and transition elements,” *Journal of Physics: Condensed Matter*, vol. 6, pp. 8245–8257, 10 1994.
- [60] G. Kresse and J. Hafner, “Ab initio molecular-dynamics simulation of the liquid-metal–amorphous-semiconductor transition in germanium,” *Physical Review B*, vol. 49, pp. 14251–14269, 5 1994.
- [61] G. Kresse and J. Furthmüller, “Efficiency of ab-initio total energy calculations for metals and semiconductors using a plane-wave basis set,” *Computational Materials Science*, vol. 6, pp. 15–50, 7 1996.
- [62] L. Nordheim, “Zur Elektronentheorie der Metalle. I,” *Annalen der Physik*, vol. 401, pp. 607–640, 1 1931.
- [63] L. Bellaïche and D. Vanderbilt, “Virtual crystal approximation revisited: Application to dielectric and piezoelectric properties of perovskites,” *Physical Review B*, vol. 61, p. 7877, 3 2000.
- [64] H. R. Seyf, L. Yates, T. L. Bougher, S. Graham, B. A. Cola, T. Detchprohm, M.-H. Ji, J. Kim, R. Dupuis, W. Lv, and A. Henry, “Rethinking phonons: The issue of disorder,” *npj Computational Materials* 2017 3:1, vol. 3, pp. 1–8, 11 2017.
- [65] P. Soven, “Coherent-Potential Model of Substitutional Disordered Alloys,” *Physical Review*, vol. 156, p. 809, 4 1967.
- [66] G. M. Stocks, W. M. Temmerman, and B. L. Gyorffy, “Complete Solution of the Korringa-Kohn-Rostoker Coherent-Potential-Approximation Equations: Cu-Ni Alloys,” *Physical Review Letters*, vol. 41, p. 339, 7 1978.
- [67] A. Zunger, S.-H. Wei, L. G. Ferreira, and J. E. Bernard, “Special quasirandom structures,” *Physical Review Letters*, vol. 65, pp. 353–356, 7 1990.
- [68] A. Van De Walle, P. Tiwary, M. De Jong, D. L. Olmsted, M. Asta, A. Dick, D. Shin, Y. Wang, L. Q. Chen, and Z. K. Liu, “Efficient stochastic generation of special quasirandom structures,” *Calphad*, vol. 42, pp. 13–18, 9 2013.
- [69] S. Huang, F. Tian, and L. Vitos, “Elasticity of high-entropy alloys from ab initio theory,” *Journal of Materials Research* 2018 33:19, vol. 33, pp. 2938–2953, 10 2018.
- [70] S. Wang, J. Xiong, D. Li, Q. Zeng, M. Xiong, and X. Chai, “Comparison of two calculation models for high entropy alloys: Virtual crystal approximation and special quasi-random structure,” *Materials Letters*, vol. 282, p. 128754, 1 2021.
- [71] E. R. Ylvisaker, W. E. Pickett, and K. Koepf, “Anisotropy and magnetism in the LSDA + U method,” *Physical Review B*, vol. 79, p. 035103, 1 2009.

- [72] H. Kronmüller, *Handbook of Magnetism and Advanced Magnetic Materials*. John Wiley & Sons, 2007.
- [73] G. P. Srivastava, “The Physics of Phonons,” *The Physics of Phonons*, 9 2022.
- [74] A. Togo and I. Tanaka, “First principles phonon calculations in materials science,” *Scripta Materialia*, vol. 108, pp. 1–5, 11 2015.
- [75] P. Ravindran, A. Kjekshus, H. Fjellvåg, A. Delin, and O. Eriksson, “Ground-state and excited-state properties of LaMnO<sub>3</sub> from full-potential calculations,” *Physical Review B - Condensed Matter and Materials Physics*, vol. 65, pp. 644451–6444519, 2 2002.
- [76] O. L. Anderson, “A simplified method for calculating the debye temperature from elastic constants,” *Journal of Physics and Chemistry of Solids*, vol. 24, pp. 909–917, 7 1963.
- [77] A. Szilva, Y. Kvashnin, E. A. Stepanov, L. Nordström, O. Eriksson, A. I. Lichtenstein, and M. I. Katsnelson, “Quantitative theory of magnetic interactions in solids,” *Reviews of Modern Physics*, vol. 95, p. 035004, 9 2023.
- [78] A. Lichtenstein, M. Katsnelson, V. Antropov, and V. Gubanov, “Local spin density functional approach to the theory of exchange interactions in ferromagnetic metals and alloys,” *Journal of Magnetism and Magnetic Materials*, vol. 67, pp. 65–74, 5 1987.
- [79] Y. O. Kvashnin, O. Grånäs, I. Di Marco, M. I. Katsnelson, A. I. Lichtenstein, and O. Eriksson, “Exchange parameters of strongly correlated materials: Extraction from spin-polarized density functional theory plus dynamical mean-field theory,” *Physical Review B - Condensed Matter and Materials Physics*, vol. 91, pp. 1–10, 3 2015.
- [80] L. Bergqvist and A. Bergman, “Realistic finite temperature simulations of magnetic systems using quantum statistics,” *Physical Review Materials*, vol. 2, p. 013802, 1 2018.
- [81] N. Metropolis, A. W. Rosenbluth, M. N. Rosenbluth, A. H. Teller, and E. Teller, “Equation of State Calculations by Fast Computing Machines,” *The Journal of Chemical Physics*, vol. 21, pp. 1087–1092, 6 1953.
- [82] K. Binder and D. W. Heermann, “Monte Carlo Simulation in Statistical Physics,” 2019.
- [83] R. F. L. Evans, U. Atxitia, and R. W. Chantrell, “Quantitative simulation of temperature-dependent magnetization dynamics and equilibrium properties of elemental ferromagnets,” *Physical Review B*, vol. 91, p. 144425, 4 2015.
- [84] F. Körmann, A. Dick, T. Hickel, and J. Neugebauer, “Rescaled Monte Carlo approach for magnetic systems: Ab initio thermodynamics of bcc iron,” *Physical Review B*, vol. 81, p. 134425, 4 2010.
- [85] H. E. Nigh, S. Legvold, and F. H. Spedding, “Magnetization and electrical resistivity of gadolinium single crystals,” *Physical Review*, vol. 132, pp. 1092–1097, 11 1963.
- [86] C. H. Woo, H. Wen, A. A. Semenov, S. L. Dudarev, and P.-W. Ma, “Quantum heat bath for spin-lattice dynamics,” *Physical Review B*, vol. 91, p. 104306, 3 2015.
- [87] M. D. Kuz'min and A. M. Tishin, “Magnetocaloric effect. Part 1: An introduction to various aspects of theory and practice,” *Cryogenics*, vol. 32, pp. 545–558, 1 1992.
- [88] E. Grüneisen, “Theorie des festen Zustandes einatomiger Elemente,” *Annalen*

- der Physik*, 1912.
- [89] D. W. Cooke, F. Hellman, C. Baldasseroni, C. Bordel, S. Moyerman, and E. E. Fullerton, “Thermodynamic Measurements of Fe-Rh Alloys,” *Physical Review Letters*, vol. 109, p. 255901, 12 2012.
- [90] M. E. Gruner, E. Hoffmann, and P. Entel, “Instability of the rhodium magnetic moment as the origin of the metamagnetic phase transition in  $\alpha$  - FeRh,” *Physical Review B*, vol. 67, p. 064415, 2 2003.
- [91] S. Polesya, S. Mankovsky, D. Ködderitzsch, J. Minár, and H. Ebert, “Finite-temperature magnetism of FeRh compounds,” *Physical Review B*, vol. 93, p. 024423, 1 2016.
- [92] P. M. Derlet, “Landau-Heisenberg Hamiltonian model for FeRh,” *Physical Review B*, vol. 85, p. 174431, 5 2012.
- [93] R. Y. Gu and V. P. Antropov, “Dominance of the spin-wave contribution to the magnetic phase transition in FeRh,” *Physical Review B*, vol. 72, p. 012403, 7 2005.
- [94] M. Wolloch, M. E. Gruner, W. Keune, P. Mohn, J. Redinger, F. Hofer, D. Suess, R. Podloucky, J. Landers, S. Salamon, F. Scheibel, D. Spoddig, R. Witte, B. Roldan Cuenya, O. Gutfleisch, M. Y. Hu, J. Zhao, T. Toellner, E. E. Alp, M. Siewert, P. Entel, R. Pentcheva, and H. Wende, “Impact of lattice dynamics on the phase stability of metamagnetic FeRh: Bulk and thin films,” *Physical Review B*, vol. 94, p. 174435, 11 2016.
- [95] J. B. Staunton, R. Banerjee, M. d. S. Dias, A. Deak, and L. Szunyogh, “Fluctuating local moments, itinerant electrons, and the magnetocaloric effect: Compositional hypersensitivity of FeRh,” *Physical Review B*, vol. 89, p. 054427, 2 2014.
- [96] H. Söderblom, “Comparison of Methods for Characterization of Magnetocaloric Materials,” 2022.
- [97] R. Essajai, N. Ennassiri, M. Balli, M. Zidane, E. Salmani, O. Mounkachi, M. Rouchdi, A. Abbassi, H. Ez-Zahraouy, A. Mzerd, and N. Hassanain, “Revisiting the magnetic and magnetocaloric properties of bulk gadolinium: A combined DFT and Monte Carlo simulations,” *Physica Scripta*, vol. 96, p. 015808, 11 2020.
- [98] S. B. Palmer, E. W. Lee, and M. N. Islam, “The Elastic Constants of Gadolinium, Terbium and Erbium,” *Proceedings of the Royal Society of London. Series A, Mathematical and Physical Sciences*, vol. 338, pp. 341–357, 10 1974.
- [99] I. P. Miranda, “Personal communication,” 2023.
- [100] F. Körmann, A. Dick, B. Grabowski, T. Hickel, and J. Neugebauer, “Atomic forces at finite magnetic temperatures: Phonons in paramagnetic iron,” *Physical Review B - Condensed Matter and Materials Physics*, vol. 85, p. 125104, 3 2012.
- [101] Y. Ikeda, A. Seko, A. Togo, and I. Tanaka, “Phonon softening in paramagnetic bcc Fe and its relationship to the pressure-induced phase transition,” *Physical Review B - Condensed Matter and Materials Physics*, vol. 90, p. 134106, 10 2014.
- [102] R. C. Wayne, “Pressure dependence of the magnetic transitions in Fe-Rh alloys,” *Physical Review*, vol. 170, pp. 523–527, 6 1968.
- [103] Y.-m. Zhou, X. Gao, and D.-s. Wang, “Exchange interaction and magnetic

- phase transition in FeRh alloy,” *Journal of Magnetism and Magnetic Materials*, vol. 226-230, pp. 1042–1044, 5 2001.
- [104] L. M. Sandratskii and P. Mavropoulos, “Magnetic excitations and femtomagnetism of FeRh: A first-principles study,” *Physical Review B*, vol. 83, p. 174408, 5 2011.
- [105] N. Golosova, D. Kozlenko, E. Lukin, S. Kichanov, and B. Savenko, “High pressure effects on the crystal and magnetic structure of 160Gd metal,” *Journal of Magnetism and Magnetic Materials*, vol. 540, p. 168485, 12 2021.
- [106] M. Mito, Y. Kimura, K. Yamakata, M. Ohkuma, H. Chayamichi, T. Tajiri, H. Deguchi, and M. Ishizuka, “Relationship of magnetic ordering and crystal structure in the lanthanide ferromagnets Gd, Tb, Dy, and Ho at high pressures,” *PHYSICAL REVIEW B*, vol. 103, p. 24444, 2021.
- [107] T. Iwamoto, M. Mito, M. Hidaka, T. Kawae, and K. Takeda, “Magnetic measurement of rare earth ferromagnet gadolinium under high pressure,” *Physica B: Condensed Matter*, vol. 329-333, pp. 667–668, 5 2003.
- [108] Q. Li, H. Ehteshami, K. Munro, M. Marqués, M. I. McMahon, S. G. Macleod, and G. J. Ackland, “Nonexistence of the  $\text{f}$  volume-collapse transition in solid gadolinium at pressure,” *PHYSICAL REVIEW B*, vol. 104, p. 144108, 2021.
- [109] M. Tokita, K. Zenmyo, H. Kubo, K. Takeda, M. Mito, and T. Iwamoto, “RKKY interaction in metallic Gd in GPa pressure regions,” *Journal of Magnetism and Magnetic Materials*, vol. 272-276, pp. 593–594, 5 2004.
- [110] M. Mito, K. Matsumoto, Y. Komorida, H. Deguchi, S. Takagi, T. Tajiri, T. Iwamoto, T. Kawae, M. Tokita, and K. Takeda, “Volume shrinkage dependence of ferromagnetic moment in lanthanide ferromagnets gadolinium, terbium, dysprosium, and holmium,” *Journal of Physics and Chemistry of Solids*, vol. 70, pp. 1290–1296, 9 2009.
- [111] B. R. Coles, “Transformation effects, stacking faults and magnetism in the light rare earths,” *Journal of Magnetism and Magnetic Materials*, vol. 15-18, pp. 1225–1226, 1 1980.
- [112] O. Beckman, L. Lundgren, P. Nordblad, P. Svedlindh, A. Törne, Y. Andersson, and S. Rundqvist, “Specific Heat of the Ferromagnet Fe 2 P,” *Physica Scripta*, vol. 25, pp. 679–681, 6 1982.
- [113] R. Duraj, R. Zach, and A. Szytuła, “Magnetic phase transitions in NiMnSi<sub>n</sub>Ge<sub>1-n</sub> and NiMn<sub>1-t</sub>Ti<sub>t</sub>Ge systems under pressure,” *Journal of Magnetism and Magnetic Materials*, vol. 73, pp. 69–78, 5 1988.
- [114] A. Biswas, A. K. Pathak, N. A. Zarkevich, X. Liu, Y. Mudryk, V. Balema, D. D. Johnson, and V. K. Pecharsky, “Designed materials with the giant magnetocaloric effect near room temperature,” *Acta Materialia*, vol. 180, pp. 341–348, 2019.
- [115] S. Ghosh, P. Sen, and K. Mandal, “Magnetostructural transition and large magnetocaloric effect in (Mn<sub>0.6</sub>Fe<sub>0.4</sub>)NiSi<sub>1-x</sub>Al<sub>x</sub> (x = 0.06–0.08) alloys,” *Journal of Magnetism and Magnetic Materials*, vol. 500, p. 166345, 4 2020.
- [116] B. Eggert, J. Belo, J. Araújo, B. Hauback, and C. Frommen, “Structural transitions and magnetocaloric properties of low-cost MnNiSi-based intermetallics,” *Intermetallics*, vol. 154, p. 107823, 3 2023.
- [117] C. L. Zhang, D. H. Wang, Z. D. Han, B. Qian, H. F. Shi, C. Zhu, J. Chen, and T. Z. Wang, “The tunable magnetostructural transition in MnNiSi-FeNiGe

- system,” *Applied Physics Letters*, vol. 103, p. 132411, 9 2013.
- [118] R. Skomski and D. Sellmyer, “Curie temperature of multiphase nanostructures,” *David Sellmyer Publications*, 5 2000.
- [119] K. Momma and F. Izumi, “VESTA3 for three-dimensional visualization of crystal, volumetric and morphology data,” *Journal of Applied Crystallography*, vol. 44, pp. 1272–1276, 12 2011.
- [120] T. Gottschall, K. P. Skokov, D. Benke, M. E. Gruner, and O. Gutfleisch, “Contradictory role of the magnetic contribution in inverse magnetocaloric Heusler materials,” *Physical Review B*, vol. 93, p. 184431, 5 2016.
- [121] C. Ortiz, O. Eriksson, and M. Klintonberg, “Data mining and accelerated electronic structure theory as a tool in the search for new functional materials,” *Computational Materials Science*, vol. 44, pp. 1042–1049, 2 2009.
- [122] N. Mounet, M. Gibertini, P. Schwaller, D. Campi, A. Merkys, A. Marrazzo, T. Sohier, I. E. Castelli, A. Cepellotti, G. Pizzi, and N. Marzari, “Two-dimensional materials from high-throughput computational exfoliation of experimentally known compounds,” *Nature Nanotechnology*, vol. 13, no. 3, pp. 246–252, 2018.
- [123] O. Eriksson, “Searching for materials with reduced dimension,” *Nature Nanotechnology 2018 13:3*, vol. 13, pp. 180–181, 2 2018.
- [124] A. Vishina, O. Y. Vekilova, T. Björkman, A. Bergman, H. C. Herper, and O. Eriksson, “High-throughput and data-mining approach to predict new rare-earth free permanent magnets,” *Physical Review B*, vol. 101, 3 2020.
- [125] A. Vishina, D. Hedlund, V. Shtender, E. K. Delczeg-Czirjak, S. R. Larsen, O. Y. Vekilova, S. Huang, L. Vitos, P. Svedlindh, M. Sahlberg, O. Eriksson, and H. C. Herper, “Data-driven design of a new class of rare-earth free permanent magnets,” *Acta Materialia*, vol. 212, 6 2021.
- [126] A. Vishina, O. Eriksson, and H. C. Herper, “Fe<sub>2</sub>C- and Mn<sub>2</sub>(W/Mo)B<sub>4</sub>-based rare-earth-free permanent magnets as a result of the high-throughput and data-mining search,” *Materials Research Letters*, vol. 11, no. 1, pp. 76–83, 2023.
- [127] A. Vishina, O. Eriksson, and H. C. Herper, “Stable and metastable rare-earth-free permanent magnets from a database of predicted crystal structures,” *Acta Materialia*, vol. 261, 12 2023.
- [128] M. Marathe and H. C. Herper, “Exploration of all- 3d Heusler alloys for permanent magnets: An ab initio based high-throughput study,” *Physical Review B*, vol. 107, p. 174402, 5 2023.
- [129] H. Zhou, S. Yan, L. Wu, X. Wan, and D. Wang, “High-throughput search for potential permanent magnet materials,” *Physical Review Materials*, vol. 7, p. 044405, 4 2023.
- [130] J. D. Bocarsly, E. E. Levin, C. A. Garcia, K. Schwennicke, S. D. Wilson, and R. Seshadri, “A Simple Computational Proxy for Screening Magnetocaloric Compounds,” *Chemistry of Materials*, vol. 29, pp. 1613–1622, 2 2017.
- [131] C. A. Garcia, J. D. Bocarsly, and R. Seshadri, “Computational screening of magnetocaloric alloys,” *Physical Review Materials*, vol. 4, p. 024402, 2 2020.
- [132] N. M. Fortunato, A. Taubel, A. Marmodoro, L. Pfeuffer, I. Ophale, H. Ebert, O. Gutfleisch, H. Zhang, N. M. Fortunato, I. Ophale, H. Zhang, A. Taubel, L. Pfeuffer, O. Gutfleisch, A. Marmodoro, and H. Ebert, “High-Throughput Design of Magnetocaloric Materials for Energy Applications: MM’X alloys,”

- Advanced Science*, p. 2206772, 4 2023.
- [133] I. Batashev, G. A. de Wijs, and E. Brück, “Computational screening of the magnetocaloric materials,” in *Handbook of Magnetic Materials*, vol. 30, pp. 1–39, Elsevier, 1 2021.
- [134] N. A. Zarkevich, D. D. Johnson, and V. K. Pecharsky, “High-throughput search for caloric materials: the CaloriCool approach,” *Journal of Physics D: Applied Physics*, vol. 51, p. 024002, 1 2018.
- [135] A. Tantillo, “Optimization of Materials for Magnetic Refrigeration and Thermomagnetic Power Generation,” *Dissertations, Theses, and Capstone Projects*, 6 2021.
- [136] H. Yamada and T. Goto, “Itinerant-electron metamagnetism and giant magnetocaloric effect,” *Physical Review B*, vol. 68, p. 184417, 11 2003.
- [137] A. Jain, S. P. Ong, G. Hautier, W. Chen, W. D. Richards, S. Dacek, S. Cholia, D. Gunter, D. Skinner, G. Ceder, and K. A. Persson, “Commentary: The materials project: A materials genome approach to accelerating materials innovation,” *APL Materials*, vol. 1, p. 11002, 7 2013.
- [138] E. K. Delczeg-Czirjak, Z. Gercsi, L. Bergqvist, O. Eriksson, L. Szunyogh, P. Nordblad, B. Johansson, and L. Vitos, “Magnetic exchange interactions in B-, Si-, and As-doped Fe 2P from first-principles theory,” *Physical Review B - Condensed Matter and Materials Physics*, vol. 85, no. 22, pp. 1–7, 2012.
- [139] V. Ksenofontov, G. Melnyk, M. Wojcik, S. Wurmehl, K. Kroth, S. Reiman, P. Blaha, and C. Felser, “Structure and properties of comnsb in the context of half-metallic ferromagnetism,” *Phys. Rev. B*, vol. 74, p. 134426, Oct 2006.
- [140] H. Fu, H. J. Yu, B. H. Teng, X. Y. Zhang, and X. T. Zu, “Magnetic properties and magnetic entropy change of Co<sub>50</sub>Ni<sub>22</sub>Ga<sub>28</sub> alloy,” *Journal of Alloys and Compounds*, vol. 474, pp. 595–597, 4 2009.
- [141] V. Sharma, S. Pattanaik, H. Parmar, and R. V. Ramanujan, “Magnetocaloric properties and magnetic cooling performance of low-cost Fe<sub>75-x</sub>Cr<sub>x</sub>Al<sub>25</sub> alloys,” *MRS Communications*, vol. 8, pp. 988–994, 9 2018.
- [142] E. Martinez Teran and E. M. Teran, *Near Room Temperature Magnetocaloric Materials for Magnetic Refrigeration*. PhD thesis, University of Texas at El Paso, 1 2019.
- [143] Z. H. Liu, M. Zhang, Y. T. Cui, Y. Q. Zhou, W. H. Wang, G. H. Wu, X. X. Zhang, and G. Xiao, “Martensitic transformation and shape memory effect in ferromagnetic Heusler alloy Ni<sub>2</sub>FeGa,” *Applied Physics Letters*, vol. 82, p. 424, 1 2003.
- [144] D. Pal and K. Mandal, “Magnetocaloric effect and magnetoresistance of Ni–Fe–Ga alloys,” *Journal of Physics D: Applied Physics*, vol. 43, p. 455002, 10 2010.
- [145] H. Nishihara, K. Komiyama, I. Oguro, T. Kanomata, and V. Chernenko, “Magnetization processes near the Curie temperatures of the itinerant ferromagnets, Ni<sub>2</sub>MnGa and pure nickel,” *Journal of Alloys and Compounds*, vol. 442, pp. 191–193, 9 2007.
- [146] A. Planes, L. Mañosa, X. Moya, T. Krenke, M. Acet, and E. F. Wassermann, “Magnetocaloric effect in Heusler shape-memory alloys,” *Journal of Magnetism and Magnetic Materials*, vol. 310, pp. 2767–2769, 3 2007.
- [147] S. Li, M. Liu, Z. Huang, F. Xu, W. Zou, F. Zhang, and Y. Du, “CoMnSb: A magnetocaloric material with a large low-field magnetic entropy change at

intermediate temperature,” *Journal of Applied Physics*, vol. 99, p. 63901, 3 2006.

- [148] R. Pacurariu, V. Rednic, M. Coldea, D. Benea, V. Pop, O. Isnard, and M. Neumann, “Effects of substitution of Ni by Sb in MnNi,” *physica status solidi (b)*, vol. 246, pp. 50–55, 1 2009.





## Original publications



**High-throughput compatible approach for entropy estimation in magnetocaloric materials: FeRh as a test case**

Rafael Martinho Vieira, Olle Eriksson, Anders Bergman, Heike C. Herper

*J. Alloys Compd.* 857, 157811 (2021)





# High-throughput compatible approach for entropy estimation in magnetocaloric materials: FeRh as a test case



R. Martinho Vieira <sup>a,\*</sup>, O. Eriksson <sup>a,b</sup>, A. Bergman <sup>a</sup>, H.C. Herper <sup>a</sup>

<sup>a</sup> Department of Physics and Astronomy, Uppsala University, Box 516, SE-75120, Uppsala, Sweden

<sup>b</sup> School of Science and Technology, Örebro University, SE-701 82, Örebro, Sweden

## ARTICLE INFO

### Article history:

Received 30 June 2020

Received in revised form

30 October 2020

Accepted 2 November 2020

Available online 11 November 2020

### Keywords:

FeRh

Magnetocalorics

Entropy

Phase transition

DFT

## ABSTRACT

Aiming to predict new materials for magnetic refrigeration from high-throughput calculations asks for an accurate, transferable, and resource-wise balanced approach. Here, we analyze the influence of various approximations on the calculation of key properties of magnetocaloric materials, while revisiting the well-known FeRh system for benchmarking our approach. We focus on the entropy change and its contributions from the electronic, lattice, and magnetic degrees of freedom. All approximations considered are based on first-principles methods and have been tested, and compared for FeRh. In particular, we find that in this context, the Debye approximation for the lattice entropy fails, due to the presence of soft phonon modes in the AFM phase. This approximation is frequently used in the literature as a simple alternative to full phonon calculations. Since soft modes are likely to occur also among promising magnetocaloric materials where structural transformations are common, the use of the Debye approximation should be discarded for these systems treatment. This leaves the calculations of the lattice contribution the most demanding task from the computational point of view, while the remaining contributions can be approximated using more efficient approaches. The entropy change  $\Delta S$  shows a peak around 370 K, for which the total entropy change is given by  $24.8 \text{ JK}^{-1}\text{kg}^{-1}$  ( $\Delta S_{\text{ele}} = 7.38$ ,  $\Delta S_{\text{lat}} = 7.05$ ,  $\Delta S_{\text{mag}} = 10.36 \text{ JK}^{-1}\text{kg}^{-1}$ ) in good agreement with previous theoretical and experimental findings.

© 2020 The Authors. Published by Elsevier B.V. This is an open access article under the CC BY license (<http://creativecommons.org/licenses/by/4.0/>).

## 1. Introduction

The idea of replacing convectional room temperature cooling devices by solid-state magnetic devices, which have the potential for better energy efficiency without producing harmful greenhouse gases, has promoted the interest in magnetocaloric materials. The search for new materials with a more attractive performance/cost ratio or tuning of known compounds is crucial in order to use such devices in mass production and everyday applications [1–5].

First principles high-throughput calculations can be a powerful approach to identify suitable candidates with desired properties by screening a large body of data. To be able to do that, large databases and screening parameters, which are carefully selected to achieve a balance between the accuracy and the cost of the computation are required [6,7].

The performance of materials used in a magnetocaloric cycle can

be characterized by the refrigerant capacity,  $RC = \Delta S_{\text{iso}} \Delta T_{\text{adi}}$ , where  $\Delta S_{\text{iso}}$  is the isothermal entropy variation and  $\Delta T_{\text{adi}}$  is the adiabatic temperature change. None of these parameters can be easily estimated from first principles electronic structure calculations, instead, a more tailored approach is necessary to take into account the finite temperature effects. Analogous to Ref. [8], we propose the use of the entropy variation between the involved magnetic phases ( $\Delta S$ ) as an approximation of  $\Delta S_{\text{iso}}$ . In this way, the transition itself and the field contribution are not included on the description, simplifying considerably the calculation. The magnetocaloric effect is in general small unless it is operated at temperatures in the vicinity of a phase transition, whereas it is strongly enhanced by the entropy variation of a transition, which justifies our approach [2,9].

In a simplified model, entropy can be described by the sum of three independent contributions: the electronic entropy, the magnetic entropy and the lattice entropy:  $S = S_{\text{ele}} + S_{\text{mag}} + S_{\text{lat}}$ . This is a simplification of the real processes, since most of the magnetocaloric materials show magnetostructural or magnetoelastic transitions indicating strong coupling between lattice and magnetic degrees of freedom. A consequence of neglecting these

\* Corresponding author.

E-mail address: [rafael.vieira@physics.uu.se](mailto:rafael.vieira@physics.uu.se) (R.M. Vieira).

coupling terms (or taking them as constants) is that, their contribution are “double-counted” when summing the three contributions. However, as shown here, the simplified approach still provides a reliable estimation for  $\Delta S$  without overburdening the calculations [1,10].

By using  $\Delta S$  as a screening parameter, we are likely limiting our search to materials with first order transitions, since they have enhanced entropy variation [2,4,10]. These materials show better magnetocaloric performance but can also be more challenging to operate in practice, due to hysteresis losses. As pointed out in Ref. [4], first order transitions have hysteresis that can reduce drastically the performance in multi-cycle processes and thus make the materials less attractive for real cooling devices applications. However, even with the above-mentioned limitations in mind,  $\Delta S$  is a natural choice for screening potential magnetocaloric materials, when attempting high-throughput approaches.

In order to be used in high-throughput calculations we need to explore the degree of complexity needed to get reliable estimations for the different contributions for  $\Delta S$ . Therefore, FeRh, a well-known magnetocaloric system, is used as a test case keeping in mind that the approach should be as general as possible in order to be transferable to other systems. Starting from simple models, the different conventional approaches are compared relatively to their performance and applicability for high-throughput calculations. We would like to stress that the focus of our study is on the methodology used for first-principles entropy estimations and not on the test material, FeRh, itself that was chosen by thorough studies available in the literature [8,11–22].

Over the years, the unusual metamagnetic first-order transition of ordered FeRh alloys with CsCl structure has caught huge attention, which is reflected, in a larger number of experimental and theoretical studies [11–13,18,23–31]. An isostructural transition from a low-temperature antiferromagnetic (AFM) phase to a high-temperature ferromagnetic (FM) phase occurs near room temperature (around 340K), accompanied by a volume increase of about 1%. The transition is also characterized by the considerable gain of the magnetic moment of the Rh atoms ( $\approx 1 \mu_B$ ) from a nonmagnetic state in the AFM phase (type G), which stabilizes the FM phase [13].

Early attempts to determine the origin of the transition e.g. using the exchange-inversion model of Kittel [32,33] were incompatible with the large entropy variation observed in FeRh. Based on the measured electronic contribution to the entropy variation Tu et al. proposed that the transition might be driven by changes in the electronic structure [23], however this explanation did not compare to previous results for Ir doped FeRh [34]. Later, it was proposed by Gruner et al. that the transition is driven by magnetic fluctuations [13], and the same conclusion was obtained by Gu et al. [18] and Staunton et al. [16] using different approaches.

Nowadays, there is a renewed interest in these compounds due to their magneto- and barocaloric properties. Examples of such studies are e.g. the performance of the magnetocaloric effect (MCE) under cyclic conditions [29] and the variation of the magnetocaloric response between FeRh based ternary compounds [35]. Very recently, the existence of an orthorhombic low-temperature phase of FeRh has been predicted from first-principles calculations [12,14,36] as well as a martensitic transformation under strain [14,15,37].

The existence of such broad knowledge and detailed information in the literature together with the complex metamagnetic behaviour that demands a careful treatment makes FeRh an ideal test system for our purpose to identify a method that can be applied in a high-throughput study for finding new magnetocaloric materials.

The discussion in the present work is divided in two parts. In the first part, we discuss thoroughly the single entropy contribution in

terms of electronic, lattice and magnetic components. This is done for FeRh using different approximations, albeit without considering thermal effects on the structure. In the second part, we include volume expansion/contraction from thermal effects and compare with the previous results, using the approximations we found to be adequate to describe the system. From this we are able to conclude which is the most viable approach to be applied in high-throughput calculations.

## 2. Computational details

The structural properties as well as structure relaxations were performed using the VASP (PAW) code [38–40] with PAW potentials [41,42] while the PHONOPY [43] code was used to obtain the vibrational density of states and the phonon spectra. Magnetic and electronic properties needed for entropy calculations were derived from a full-potential linear muffin-tin orbital method (FP-LMTO) using the RSPt code [44], and respective temperature dependent quantities such as the adiabatic magnon density of states or the Curie temperature were computed using the UppASD code [45]. In all the DFT calculations, the functional GGA-PBE [46] was used, since it shows in general a good performance in transition metals and compounds, which represents the substantial part of the future database to screen.

Both FM and AFM phases were relaxed on cubic cells of 16 atoms (8 f.u.) taking 4s, 4p, and 3d for Fe as well as 5s, 5p and 4d orbitals for Rh as valence states. A kinetic energy cutoff of 500 eV, roughly 2 times bigger than the default value, was used. For sampling the Brillouin zone we used a k-mesh  $12 \times 12 \times 12$  generated with the Monkhorst-pack scheme in combination with a smearing of 0.05 eV according to the Methfessel-Paxton scheme (2<sup>nd</sup> order). Tests with the inclusion of the Fe 3p and Rh 4p semi-core states in the valence, as well the usage of a higher cutoff energy (750 eV) revealed that the calculations are converged with respect to these parameters. The relaxed lattice parameters of 2.99 Å (AFM) and 3.01 Å (FM) are in good agreement with previous calculations, e.g. 2.99 (3.01) Å [12], 3.00 (3.01) Å [8] for the AFM (FM) phase. They are also in good agreement with experimental measurements, 3.00 Å [47], and 2.98 (3.00) [48] for the AFM (FM) phase. For these volumes, the magnetic moments obtained from these calculations are  $m_{Fe} = 3.21 \mu_B$  and  $m_{Rh} = 1.05 \mu_B$  in the FM phase, and  $m_{Fe} = 3.12 \mu_B$  and  $m_{Rh} = 0.0 \mu_B$  in the AFM phase. These results are close to the experimentally measured values of an alloy with 48% Rh in the FM phase,  $m_{Fe} = 3.2 \mu_B$  and  $m_{Rh} = 0.9 \mu_B$  [49,50], as well as to the measurements for the AFM phase of a stoichiometric compound,  $m_{Fe} = 3.3 \mu_B$  [50]. The obtained results are also in close agreement with previous calculations: e.g.  $m_{Fe} = 3.18 \mu_B$  [12],  $3.15 \mu_B$  [11] and  $m_{Rh} = 1.06 \mu_B$  [12],  $1.02 \mu_B$  [11] for the FM phase and  $m_{Fe} = 3.12 \mu_B$  [12],  $2.98 \mu_B$  [11] in the AFM phase. At T = 0K, the AFM phase is lower with 26.9 meV/atom (VASP calculation<sup>1</sup>) compared to the metastable FM phase.

The phonon calculations were performed within the harmonic approximation employing the finite displacement method in a similar setup as used on the structural relaxation. We used displacements of 0.01 Å for these calculations. A  $2 \times 2 \times 2$  supercell from the relaxed structures with 128 atoms (64 f.u.) was employed. For this supercell we used a coarser k-mesh  $6 \times 6 \times 6$ . No improvement was observed by increasing the cutoff energy to 750 eV and neither a significant change of the phonon spectrum with the inclusion of 3p (Fe) and 4p (Rh) orbitals in convergence tests performed for cells of 16 atoms. To make it easier to compare results with previous calculations [8,12], we employed also a similar setup, with a cutoff of 500 eV and the inclusion of the semi-

<sup>1</sup> 29.6 meV in the analogous RSPt calculation.

core states in all phonon calculations.

For calculations performed with the RSPT code, we used fcc-like structures of 4 atoms (2 f.u.), with the previously relaxed lattice parameter on a  $36 \times 36 \times 36$  k-mesh with related integrated quantities broadened by Fermi smearing of 1 mRy. The exchange parameters  $J_{ij}$  were calculated using the Liechtenstein method [51,52], implemented in the RSPT code, as described in Ref. [53]. The Curie temperature ( $T_C$ ) calculated via mean field theory according to the obtained values of  $J_{ij}$  for the FM phase is of 804 K, which is comparable to the experimentally measured value of 675 K [33,47]. This agreement is good, given the fact that mean-field theory tends to overestimate  $T_C$  about  $\sim 20\%$  (as discussed e.g. in Ref. [45]). For analysis of the long range behaviour with distance, the exchange parameters were calculated on a denser k-mesh of  $64 \times 64 \times 64$  to assure convergence of the results.

### 3. Results

As initial approach, anharmonic effects raised by thermal expansion were neglected and we consider only the DFT ground-state volumes for both magnetic phases. We extend the use of this terminology for elastic/structural properties for this approach to distinguish clearly that the volumes were fixed. The assumption of purely harmonic forces between atoms is insufficient to describe the thermal expansion or contraction of a material, and it may be important to consider anharmonic effects, for accurate calculations of phase stability and entropy estimates. To compare improvements obtained by this description, relatively to the previous "Harmonic" approach, we used the quasiharmonic approximation (QHA) to include the effects of thermal expansion on the entropy estimates (see more details further) [54].

#### 3.1. Electronic structure, and its contribution to the entropy

The density of states (DOS) of FeRh is shown in Fig. 1a, for the FM and AFM configuration. Note that for the AFM configuration we show the spin-polarized DOS of only one Fe atom.

The figure shows the atom with more spin-down electrons occupied, representing a Fe atom with a negative atomic moment. The Fe atom with positive moment has exactly the same DOS, although with opposite spin-projection to that shown in Fig. 1. In agreement with previous findings in the literature, a strong hybridization between iron and rhodium orbitals is observed [17]. In particular, a strong hybridization between Fe  $t_{2g}$  and Rh  $e_g$  orbitals near the Fermi energy ( $E_F - E = 2$  meV) occurs in the AFM phase, where it also can be assumed some hybridization between Fe  $e_g$  and Rh  $t_{2g}$  orbitals in the peak around  $E_F - E = 2$  meV, see Fig. 1a. For the FM state the hybridization seems to weaken, and be confined on the minority spin channel, mainly observed between  $t_{2g}$  orbitals of Fe and Rh near the Fermi energy. This observation may emphasize the picture of quenched Rh magnetic moments due to the competing influence of neighbouring iron atoms on the AFM phase. The hybridization that is diminished between Fe–Rh on the FM phase can be directly ascribed to the lifting of the anti-parallel alignment of the surrounding iron atoms. On the other hand, it can also be related to the increased volume, which can reduce orbital superposition or a combination of both effects.

In the FM phase (Fig. 1b), it is possible to distinguish a significant difference between  $t_{2g}$  and  $e_g$  orbitals of Fe at Fermi level which can be an indication of different magnetic behaviour of these orbitals similar as observed for bcc-Fe in Ref. [55]. There it was found that  $t_{2g}$  orbitals, with likewise bigger contribution for the electronic density of states  $DOS(\epsilon_F)$ , were related to the long-range Ruderman–Kittel–Kasuya–Yosida (RKKY) interactions while the  $e_g$  were associated with direct exchange with nearest neighbours. The

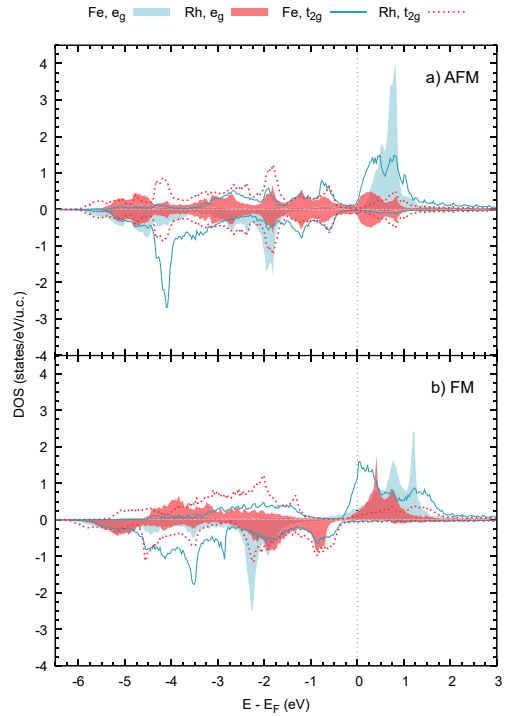


**Fig. 1.** Electronic DOS for FeRh in the AFM (a) and FM (b) phase. The DOS is projected onto Fe 3d states, with  $e_g$  and  $t_{2g}$  symmetry, and Rh 4d states, with  $e_g$  and  $t_{2g}$  symmetry. The density of the minority states is displayed on the negative axis. For interpretation of the references to color in this figure legend, the reader is referred to the Web version of this article.

similarities, observed in the projected Fe DOS, might hint for the existence of some similarities between magnetic behaviour of Fe atoms of both compounds.

The contribution of electronic excitations to the entropy is given by the mixing entropy of occupied and unoccupied states:

$$S_{ele} = -k_B \int D(\epsilon) ([1 - f(\epsilon, T)] \ln(1 - f(\epsilon, T)) + f(\epsilon, T) \ln(f(\epsilon, T))) \quad (1)$$

where  $D(\epsilon)$  is the density of states and  $f = [\exp((\epsilon - \mu)/(k_B T)) + 1]^{-1}$  is the Fermi-Dirac distribution. Furthermore,  $k_B$  is the Boltzmann constant and  $\mu$  is the temperature dependent chemical potential. For temperatures considerably below the Fermi temperature, it is reasonable to approximate  $\mu$  with the Fermi energy,  $E_F$ . Then the electronic entropy can be estimated from the Sommerfeld approximation [56].

$$S_{ele} = \frac{\pi^2}{3} k_B^2 T D(\epsilon_F). \quad (2)$$

In Fig. 2, the results obtained from both models are compared, showing a good agreement for temperatures till 300K. Outside this range the results differ, resulting in a small deviation observed for

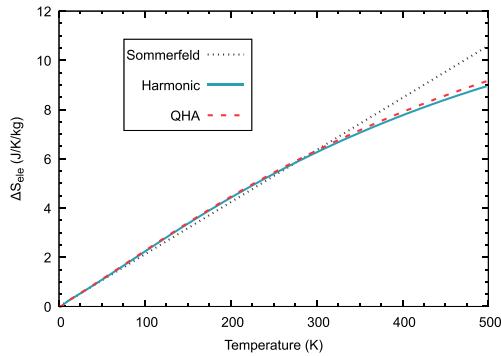


**Fig. 2.** Electronic contribution to the entropy variation  $\Delta S = S_{FM} - S_{AFM}$  according the Sommerfeld approximation (black dotted line) and the mixing entropy in the harmonic (blue solid line) and the quasi-harmonic (red dashed line) approaches. For interpretation of the references to color in this figure legend, the reader is referred to the Web version of this article.

temperatures close to the transition temperature for the transition from antiferromagnetism to ferromagnetism. The deviations arise from the AFM phase and can be explained by the absence of peak structures in DOS at the Fermi energy (Fig. 1) as the Sommerfeld approximation assumes. Nevertheless, the deviation between the discussed models for  $S_{elec}$  estimation, in the range of the transition, is small being the obtained difference of  $1.84 \text{ J K}^{-1} \text{ kg}^{-1}$  for  $\Delta S_{elec}$ , and 26 K for the transition temperature (discussed in further sections). Although there is not significant loss of accuracy estimating  $S_{elec}$  using Eq. (2), using the definition of mixing entropy does not imply extra computational effort. Thus to avoid eventual inaccuracies that may arise by using Sommerfeld approximation, we use the definition in Eq. (1) as the standard method for calculating the electronic entropy.

### 3.2. Magnetic contribution to the entropy

For materials with order-disorder magnetic transitions, the maximum magnetic entropy variation between phases can be roughly estimated from  $\Delta S_{mag} = Nk_B \ln[2S+1]$  (in a quantum description) with  $N$  being the number of magnetic atoms [24]. This comes about since very few microstates are available for highly ordered states, and the entropy of this configuration can be neglected in the limiting case  $T \rightarrow 0$ . In contrast, for the disordered configuration we have  $(2S+1)^N$  arrangements for the spins for  $T \rightarrow \infty$ , which results in the entropy change across the order-disorder transition as described above.

According to the analysis above, it is expected that order-order transitions at finite temperature have a considerably smaller entropy change from the magnetic subsystem.

Based on this and the argument that considering the itinerant nature of magnetism of FeRh, the magnetic contribution to  $\Delta S$  is already included in the electronic entropy computed from the DOS, some reports argue that the magnetic contribution of the entropy does not need to be considered separately [8]. To some extent, it is possible that some magnetic contribution is captured by  $\Delta S_{elec}$ , since some coupling between the degrees of freedom is expected. However, taking into consideration the increase of the Rh magnetic moment from 0 (AFM) to  $\approx 1\mu_B$  (FM), it seems that the magnetic entropy for this transition must be considered specifically. A good reason for that are the new two-site interactions between Fe and Rh

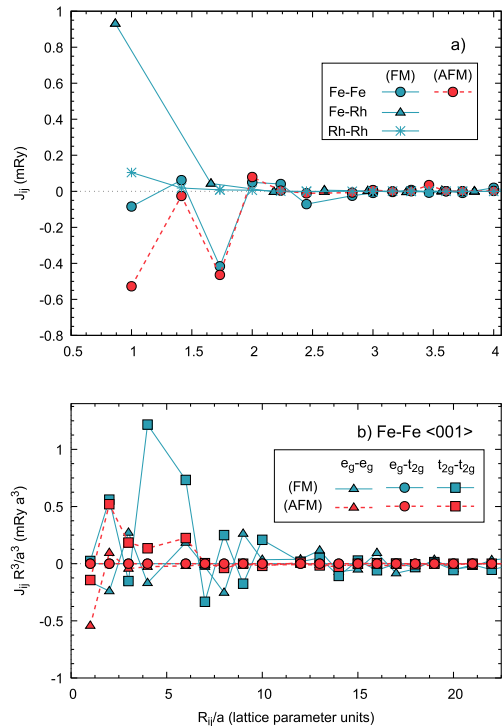


**Fig. 3.** Calculated exchange parameters ( $J_{ij}$ ) calculated for FeRh, decomposed according the involved atoms type a), and crystal field symmetry b). In b) are only plotted the exchange interactions between iron atoms along the  $\langle 001 \rangle$  direction. For interpretation of the references to color in this figure legend, the reader is referred to the Web version of this article.

atoms of the ferromagnetic phase, described e.g. by the Heisenberg Hamiltonian, which should be considered for a proper system description (see Fig. 3a). Interestingly, Fig. 3a shows that the close range of the Fe–Fe exchange is quite similar for the AFM and FM configurations. The nearest neighbour interaction is antiferromagnetic in both phases, although the strength is larger for the AFM configuration. In addition, the general trend of the Fe–Fe interaction is quite similar for both configurations. The interaction that stabilizes the FM phase is hence not found in the Fe–Fe Heisenberg exchange. Instead, as Fig. 3a shows, the strong ferromagnetic Fe–Rh interaction is what makes the FM configuration stable at all. This represents an interesting boot-strapping effect, when the FM configuration is what allows for a sizeable Rh moment, and the sizeable Rh moment is what ensures a large Fe–Rh exchange interaction that makes the FM (meta-)stable [13].

To estimate the magnetic entropy variation we started by using a simple approximation analogous to the one used in Ref. [57] for  $\text{LaFe}_{13-x}\text{Si}_x$  alloys. From the fundamental thermodynamic relation  $dU = TdS - PdV$  one can, for isochoric processes, approximate the entropy as  $\Delta S = \Delta U/T$ . Although crude, this approximation should give an acceptable estimate for the entropy variation in first-order transitions where the entropy varies discontinuously at the transition temperature. Using this and describing the magnetic energy of the system by the classic Heisenberg Hamiltonian:



$$H = \sum_{i < j} J_{ij} \vec{S}_i \cdot \vec{S}_j \tag{3}$$

a good starting point for  $\Delta S_{mag}$  estimation can, in principle, be obtained, since energy differences between different magnetic configurations are available from Eq. (3). For FeRh this results in  $\Delta S_{mag} = -26.78 \text{ JK}^{-1} \text{ kg}^{-1}$  (at  $T = 340 \text{ K}$ ), which has the wrong sign from what is expected, a consequence of the use of a simplified Heisenberg Hamiltonian, for which the FM phase is obtained as the ground-state configuration. However, it was shown in Refs. [13,25,58,59] that an extension of the Heisenberg exchange model can be made, using e.g. higher-order interactions, to obtain a proper magnetic description of the system with very satisfactory results on Monte Carlo simulations. Here we took a different route to avoid the use of a tailored model and evaluated the magnetic entropy from spin-wave fluctuations, similar to the work in Refs. [18]. This approach is possible since the AFM-FM transition happens at considerable lower temperatures ( $\approx 340 \text{ K}$ ) than the Curie temperature of the FM phase and the spin fluctuations can still be considered to be relatively small [12]. It is also necessary to guarantee, in order to use this approach that Stoner excitations are not dominating, as was shown in Refs. [17,18].

For this reason, we calculated the magnon density of states (MDOS) from the adiabatic magnon spectrum. This calculation relied on Heisenberg exchange parameters,  $J_{ij}$ , estimated from DFT calculations. Due to the bosonic nature, the entropy of the magnons is given by:

$$S_{mag} = k_B \int_0^\infty g(\epsilon) [(1 + n(\epsilon, T)) \ln(1 + n(\epsilon, T)) - n(\epsilon, T) \ln(n(\epsilon, T))] \times |d\epsilon, \tag{4}$$

where  $g(\epsilon)$  is the MDOS and  $n = [\exp(\epsilon/k_B T) - 1]^{-1}$  is the Bose-Einstein distribution. For these calculations a perfectly aligned configuration was assumed for the spin moments when calculating the magnon dispersion ( $\vec{m} \parallel \vec{m}_z$ ). Analogous calculations performed for a thermally relaxed (at 300K) magnetic configuration do not deviate significantly from these results.

In contrast to the observation of the electronic entropy contribution, a magnetic entropy maximum ( $10.92 \text{ JK}^{-1} \text{ kg}^{-1}$ ) is obtained at around 315 K, as it can be seen in Fig. 4. This peak is of major importance since it hints to the existence of the phase transition. At least, it shows that the magnetic entropy will favour the ferromagnetic phase. Also, the lack of similar peaked behaviour around the transition temperature in the other entropy contributions (see discussion of lattice contributions, below) suggests that the transition is triggered by the magnetic features of the system. Thus, based on the applied magnetic model (spin-wave fluctuations) and the obtained MDOS for the AFM phase, we suggest that at low temperatures the Rh atoms are magnetically suppressed by the anti-parallel alignment of the surrounding Fe atoms configuration. This generates a vanishing local Weiss field on the Rh atom, that at the transition temperature has its symmetry broken by the spin fluctuations, which allow Rh to become magnetically polarized and thus stabilizes the FM configuration. A similar picture of a transition driven by small magnetic fluctuations, as the one described above, is concluded in other works, both with similar methods [18] as well as from different approaches [13,16,18,58].

It was already pointed out in the previous section, that iron atoms in FeRh might possess some features that are similar to the features they have in elemental form (bcc Fe). For instance, the

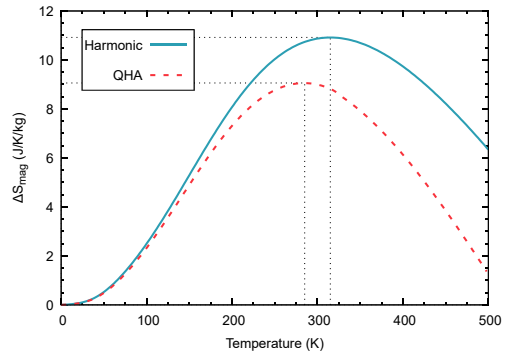


Fig. 4. Comparison of the magnetic entropy variation between the FM and AFM phase,  $\Delta S = S_{FM} - S_{AFM}$ , for the harmonic approximation (blue solid line) at fixed volume and the quasi-harmonic approximation (red dashed line) with volume variation. For interpretation of the references to color in this figure legend, the reader is referred to the Web version of this article.

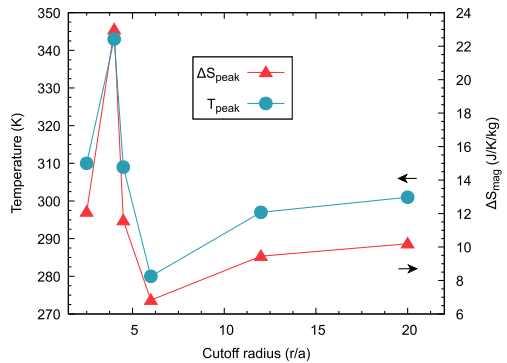


Fig. 5. Variation of the magnetic entropy peak parameters for the "Harmonic" approach with the cutoff radii for included exchange interactions in the FM phase. At the right axis, the estimated values for the magnetic entropy variation peak (red triangles) are plotted, while the left axis denotes the temperature at which the entropy variation peak occurs (blue circles). Results calculated for the FM (AFM) phase with  $a = 3.014 \text{ \AA}$  ( $a = 2.998 \text{ \AA}$ ). For interpretation of the references to color in this figure legend, the reader is referred to the Web version of this article.

existence of oscillating long-range interactions, must be taken into consideration when calculating the MDOS and thermodynamic properties from it. In Fig. 5, it is shown how the entropy peak varies with the range of magnetic couplings  $J_{ij}$  included in the calculation of the MDOS<sup>2</sup>.  $\Delta S_{mag}$  and the peak temperature show a significant dependence on the cutoff radius for the  $J_{ij}$  such that a considerable long range of interactions must be included to a fairly converged estimation. This is a consequence of long-range magnetic interactions of  $J_{Fe-Fe}$ , visible on Fig. 3b) that oscillate significantly till a range of 10 primitive cells approximately. Based on these observations we included interactions up to 12 lattice parameters in our calculations.

<sup>2</sup> More details on the MDOS variation can be found on the Supplementary materials.

The fact that the sensitivity with respect to the range of the interactions, is mainly due to interactions in the FM phase, reflect that long-range oscillating interactions are stronger on this phase (see Fig. 3b), and more significant on  $t_{2g}$  orbitals, underpins the similarity between bcc Fe and the FM phase of FeRh (see results for bcc Fe in Ref. [55]), when it comes to understanding the Heisenberg exchange. We point out that the sensitivity on the cutoff of the Heisenberg interactions is important for many prospective magnetocaloric materials, since many of them are metallic and have Fe as a key element, and the long-range magnetic interaction between Fe atoms seems to be of particular importance.

Our results of the magnetic entropy change across the AFM - FM transition are in agreement with previous calculations, see Table 1. The quite large difference between our entropy calculation and the results obtained by Gu et al., who used a similar computational approach [18], are most likely caused by the shorter range of exchange interactions considered in their work. This might also partly explain the small deviation between our results and the ones from the models used in Refs. [13,58]. Relative to the transition temperature, the higher result obtained by Staunton et al. stands out from the remaining values [16]. Such deviation might be related with the method itself - finite temperature spin density functional theory is implemented in the disordered local moment approach - which differs significantly from the other approaches. The calculations of Ref. [16] were done from an electronic structure theory that allows a random distribution of spin-orientations, and therefore neglects short-range correlations. This approach is well established and is argued [16] to describe better the electronic structure at finite temperatures.

### 3.3. Lattice contribution

The calculation of properties related to the crystal lattice can become very demanding regarding computational resources. In order to calculate such properties in an efficient way, it is imperative to minimize the numeric effort by using expedient models, without compromising significantly the accuracy. To verify which approximation is appropriate to estimate the lattice entropy, we compare the results of models of various accuracy and complexity. As contribution for the lattice entropy, only the vibrational entropy was considered.

#### 3.3.1. Debye model

In the Debye model the phonon dispersion relation is treated as linear,  $\omega = v_s|k|$ , where  $v_s$  is the speed of sound in the material. Therefore, the vibrational density of states (VDOS) is given by:

$$g(\omega) = \frac{3\omega^2}{2v_s^3\pi^2} \quad (5)$$

**Table 1**

Comparison of calculated/measured magnetic contributions for the entropy variation ( $\Delta S_{mag}$ ) and respective transition temperature ( $T_{tr}$ ). For our results the temperature for the entropy peak is used for comparison since it hints for the magnetic transition.

	This work	References			
	( $T_{peak}$ )	[18]	[13]	[58]	[16]
$\Delta S_{mag}$ [J K <sup>-1</sup> kg <sup>-1</sup> ]	10.9	15.4	5.2	15 <sup>a</sup> (8.2) <sup>b</sup>	13 <sup>c</sup>
$T_{tr}$ [K]	316	353	268	300	495

<sup>a</sup> Result obtained from specific heat analysis, at presented  $T_{tr}$ .

<sup>b</sup> Result obtained by  $\Delta E(T)/T$  at  $T = 350$ K.

<sup>c</sup> Result under a 2T magnetic field.

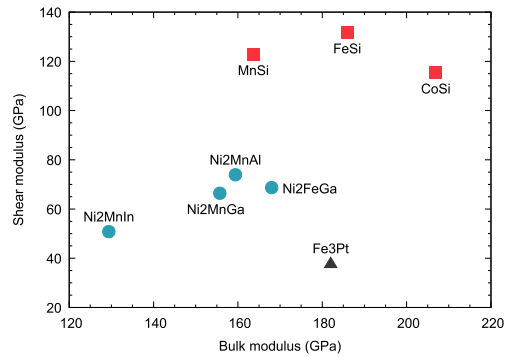


**Fig. 6.** Relation between bulk modulus and shear modulus for different magnetic materials with structural transitions. Values found in literature [61–65] for cubic phases where compounds within a given crystal structure type have the same color. Blue circles represent Heusler structures, red squares refer to the FeSi structure type and the black triangle to the Cu<sub>3</sub>Au structure type. For interpretation of the references to color in this figure legend, the reader is referred to the Web version of this article.

up to the cutoff Debye's frequency. The entropy then becomes [54]:

$$S_{lat} = k_B \left[ -3 \ln(1 - \exp(-\Theta/T)) + 12 \left( \frac{T}{\Theta} \right)^3 \int_0^{\Theta/T} \frac{x^3}{\exp(x) - 1} dx \right] \quad (6)$$

where  $\Theta$  is the Debye temperature. An important consequence of this model is that at a fixed temperature the variation of the Debye temperatures between phases ( $\Delta\Theta$ ) has opposite sign to the respective variation of lattice entropy,  $\Delta\Theta/|\Delta\Theta| = -\Delta S_{lat}/|\Delta S_{lat}|$ , this can be used to understand the nature of the lattice entropy, i.e., if it is collaborative (has same sign) or detrimental (opposite sign) relative to all other entropy contributions. The Debye temperature can be computed as  $\Theta = \hbar(6\pi^2n)^{1/3}v_s/k_B$  with the atomic density  $n$  and  $v_s$  being the average velocity of sound in the crystal. For isotropic crystals, the later is approximated as the average value of the shear and longitudinal sound velocity. It is generally expressed in terms of the bulk modulus (B), the density ( $\rho$ ), and a correction parameter<sup>3</sup>  $\xi$ , i.e.,  $v_s = \xi\sqrt{B/\rho}$ .

The correction parameter  $\xi$  depends on the elastic properties of the system. However, in Ref. [60] it was proposed that for a given class of materials  $\xi$  might be universal and can be derived from elastic constants. To verify if this approximation could be used in calculations of magnetocaloric materials we extracted the shear and bulk moduli, from data found in literature [61–65], for magnetic materials with structural transitions (expected to be present in an important class of interesting candidate materials for magneto caloric applications). Fig. 6 shows that any possible linear trend as obtained in Refs. [60] is not reasonable if compounds with different structure types are compared. This makes the approach of Ref. [60] less appropriate for high-throughput calculations and data-mining algorithms. For FeRh, in particular, this approach is specially unappealing considering the only materials with similar structure and properties are alloys very close to the stoichiometric

<sup>3</sup> Necessary for expressing  $v_s$  in terms of isotropic elastic parameter B, which can be obtained from a fitting of the equation of state.

compound.

We conclude that however inconvenient it is, the elastic properties have to be calculated for each material that one includes in any data set for high-throughput calculations, when searching for new magnetocaloric materials. For FeRh this exercise leads to a very interesting result when comparing the two magnetic phases (AFM and FM). Since the two phases have the same crystal structure, one might naively assume very similar elastic properties for both phases. However, this assumption leads to a lattice entropy contribution of  $7.9 \text{ JK}^{-1}\text{kg}^{-1}$  at 328 K, which deviates from a more accurate calculation that takes into account the difference in elasticity of the two systems (discussed more in detail below) that yield a value of  $-30.1 \text{ JK}^{-1}\text{kg}^{-1}$  at the same temperature. This later approach gets closer to the extracted from calorimetric measurements  $\approx -33 \text{ JK}^{-1}\text{kg}^{-1}$  (328K) using the same model [66].

In order to describe accurately the difference in elasticity of the two phases of FeRh, we evaluated the elastic constants using the RSPt software, for both phases. We used the stress-energy response as described in Ref. [67,68]. The values of  $C_{11} = 194.9$  (257.1)  $C_{12} = 194.9$  (165.2) and  $C_{44} = 135.3$  (115.6) GPa were estimated for the AFM (FM) phase, with qualitative agreement with previous calculations [15].

Comparing the Debye temperatures derived by using the same Poisson ratio ( $\nu$ ) for both phases and from the calculation with the different ratios for the AFM and FM phase, demonstrates the sensitivity of this model for lattice entropy to small deviations ( $\Delta\nu = 0.05$ ) of the elastic properties. Taking into account the differences in the elastic behaviour of the AFM and FM phase, the change in the Debye temperature  $\Delta\Theta$  is in good agreement with the experimental results, see Table 2.

### 3.3.2. The Debye-Grüneisen model

Taking a more sophisticated approach to estimate the lattice entropy, by use of full phonon calculations [8,12], leads different values of  $\Delta S_{lat}$ , compared to the findings from the Debye model. This is discussed in detail in the following subsection. To investigate whether a simplified approach can be improved, we first extended the Debye model to the Debye-Grüneisen model, where effects of volume variation are taken into consideration for the lattice properties. The Grüneisen parameter, needed for this model, is calculated from

$$\gamma = -g + \frac{1}{2}(1 + B'), \quad (7)$$

where  $B'$  is the volume derivative of the bulk modulus. The parameter  $g$  is an additive factor, usually taken as  $g = 1$  for low temperatures and  $g = 2/3$  for high temperatures [60,69]. Considering the volume expansion,  $V_{AFM} \rightarrow V_{FM}$ , an increase is obtained for  $|\Delta\Theta|$  which implies an increase in the magnitude of the lattice

**Table 2**

Comparison of different treatments for Debye temperature estimation and respective difference between phases,  $\Delta\Theta = \Theta_{FM} - \Theta_{AFM}$ , with experimental measurements. For the case with equal elastic properties assumed for both phases, the calculated Poisson ratio  $\nu_{FM} = 0.32$  of the FM phase was considered. For the remaining cases the  $\nu_{AFM} = 0.36$  was used.

[K]	$\Theta_{AFM}$	$\Theta_{FM}$	$\Delta\Theta$
$\nu_{AFM} = \nu_{FM}$	412	401	-11
$\nu_{AFM} \neq \nu_{FM}$	362	401	39
Expt [66]	340	393	53
Thermal effects <sup>a</sup>	352	417	65

<sup>a</sup> High temperature correction considered,  $g = 2/3$ , very similar result is obtained if the low temperature correction is taken. The volume of the FM (AFM) phase was considered as altered volume for the AFM (FM) phase.

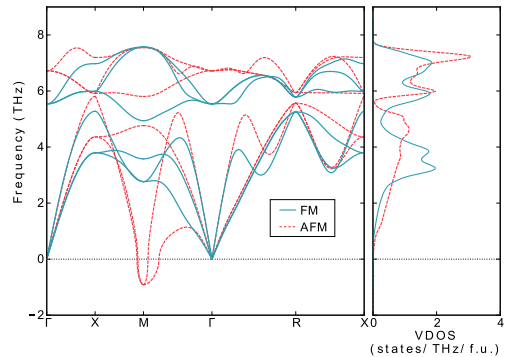


**Fig. 7.** Calculated phonon dispersion (projected on the simple cubic lattice, left) and respective density of states (VDOS, right) for the AFM (dashed red line) and FM (solid blue line) phases. For interpretation of the references to color in this figure legend, the reader is referred to the Web version of this article.

entropy variation comparatively to the previous estimate, and does not lead to theoretical values closer to the observed data.

The Debye model is known to be accurate in the limits  $T \ll \Theta$  and  $T \gg \Theta^4$ . Outside this temperature interval it is less reliable. It is for such temperatures that the magnetic transition for FeRh happens, which partly explains the difference obtained for  $S_{lat}$  using full phonon calculations. As the discussion in the next section shows, the existence of soft vibration modes has a major role in explaining these contradictory results between the simple Debye model and the results from full phonon calculations.

### 3.3.3. Entropy from full phonon calculations

The presence of soft phonon modes, reaching imaginary frequency, leads to a structural transition, which leads to enhancement of  $\Delta S_{lat}$ . Even if these soft phonon modes do not reach imaginary frequency (indicating structural instability) they may provide a hint for possible transition. It is reasonable to expect that a fair amount of magnetocaloric candidates will show this behaviour. Soft modes of the acoustic branch can give raise to energy peak structures in the vibrational density of states at low energies that are not captured by the Debye model and lead to inaccuracies even at low temperatures. Since the Debye model fails to describe the thermodynamic properties of such materials, full phonon calculations must at least be tried in order to compare with more approximate methods, and to assess if more efficient avenues exist for the calculation of the lattice entropy.

The calculated phonon dispersion, displayed in Fig. 7, shows that for most of the reciprocal space, the acoustic modes of FeRh behave quite similarly in both the FM and AFM phase. However, the AFM phase has conspicuous soft modes that even become imaginary as in previous calculations [8,12], which also showed imaginary frequencies around the  $M$  point. Such behaviour points to a dynamical instability [8,12].

This result was thoroughly discussed for FeRh in Ref. [12] and a competing low temperature monoclinic structure was proposed. Nevertheless, near the experimental transition temperature between the AFM and FM phase, the structure is known to be cubic,

<sup>4</sup> If anharmonic effects are relatively small and the equipartition of energy is a good approximation. The high temperature limit of Debye model predicts the specific heat consistently with the empirical Dulong-Petit rule [54].

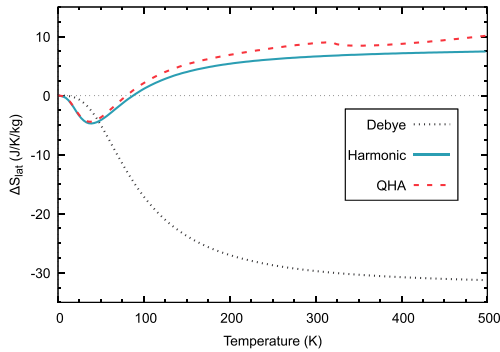


**Fig. 8.** Comparison of the lattice entropy variation between FM and AFM phases using different approaches: Debye model (black dotted line), harmonic phonon calculations (blue solid line) and quasi-harmonic approximation (red dashed line). For details of calculations, see text. For interpretation of the references to color in this figure legend, the reader is referred to the Web version of this article.

possibly caused by an entropy driven stabilization of the cubic phase, e.g. as discussed in Ref. [70]. Since the part of reciprocal space that contains imaginary frequencies is very small, as observed by their minor contributions to the VDOS in Fig. 7, its influence on thermodynamic properties is expected to be negligible [12]. We therefore neglected this contribution, to the estimation of thermal properties to avoid numerical complications.

The entropy variation derived from the VDOS (using the same expression as Eq. (4) but with  $g(\epsilon)$  as the VDOS) is shown in Fig. 8. It has the same sign and order of magnitude as the electronic contribution. To be precise the difference in calculated lattice entropy is  $7.05 \text{ J K}^{-1} \text{ kg}^{-1}$  at  $T = 373 \text{ K}$ <sup>5</sup>.

Comparing the estimates in Fig. 8 it is interesting to note that the trends for  $\Delta S_{\text{mag}}$  between Debye model and the full-phonon calculations start to differ around 40 K, when the result for the later approach displays a small entropy peak. Tracing this to Fig. 7 we can relate it to the flattening of the phonon spectra around 0.8 THz for the AFM phase, which explains the small entropy peak obtained for the full-phonons approach as the excitation of the soft phonon branches [12]. The indicated observation also underlines the role of the presence of the soft mode to the failure of the Debye model application in this material.

The difference between entropy results for phonon calculations and for Debye model in this material is as remarkable as surprising, especially when considering that it is an isostructural transition we consider. *A priori* there are no indications pointing to the need of a more complex approach, and it is clear from the calculations discussed here for the lattice entropy, that the applicability of any simplified method, such as the Debye model, should be carefully verified for lattice contributions of the entropy variation. This shortcoming of simplified models, should be taken into consideration when estimating entropy variations of any material.

### 3.4. Total entropy variation

The sum of all hitherto discussed contributions to the entropy, defines the total entropy variation between FM and AFM phases, according to our model. In Fig. 9 (solid line) it is clear that the total entropy difference between the FM and AFM phase has a

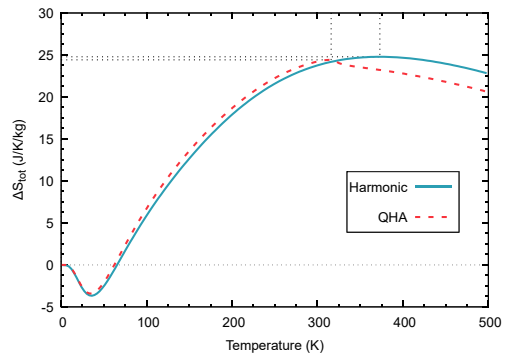


**Fig. 9.** Variation of the total entropy change between FM and AFM configuration, according to the harmonic treatment (without thermal expansion, blue solid line) and the quasi-harmonic approximation (red dashed line). For interpretation of the references to color in this figure legend, the reader is referred to the Web version of this article.

pronounced temperature dependence. In addition, the figure shows a major, broader peak around  $\sim 370 \text{ K}$  with maximum entropy difference,  $\Delta S_{\text{max}}$ , of  $24.8 \text{ J K}^{-1} \text{ kg}^{-1}$ .

In Table 3 we list all calculated contributions to the entropy change between the FM and AF phase, at  $T = 350 \text{ K}$ . It may be seen from the table that all contributions are collaborative and comparable in magnitude [12].

In the taken approach, both the type of phase transition and stoichiometry of the compound are described without the existence of losses, associated to the transition (e.g. coexistence of phases) and without defects of the material, and with this in mind, it is not unexpected that theory overestimates somewhat the entropy contributions and therefore, in this case, the total entropy change. Besides, it is important to note that experimentally is very difficult to achieve the equiatomic concentration and very close alloys are measured instead, for which the entropy variation varies slightly [35]. Nevertheless, the comparison between the here calculated value of  $\Delta S$  and experimental results is quite satisfactory [26,29,34,48,66,71–73] being of the same sign and order of magnitude. Thus, if one has the ambition to make theoretical screening approaches in combination with first principles high-throughput calculations, the level of approximation employed here seems to be the simplest way that is capable of a fairly accurate prediction while maintaining computational efficiency.

Experimentally it is not straight forward (or accurate [8]) to disentangle the entropy contributions. In Table 3 the entropy contributions of the present calculations are listed, together with the ones extracted from calorimetric measurements of Ref. [66]. Cooke et al. [66] extracted the lattice entropy by naively fitting the low-temperature data to the Debye model. This approach fails for FeRh, as discussed above, and consequently, the estimated huge magnetic entropy contribution, calculated from  $S_{\text{mag}} = S_{\text{rot}} - S_{\text{ele}} - S_{\text{lat}}$ , is not seen as a realistic contribution. Both the extracted  $\Delta S_{\text{lat}}$  and  $\Delta S_{\text{mag}}$  are unusually high in magnitude, compared to the usual total entropy values [4]. These values are also unexpectedly high, given the isostructural nature of the volume expansion and the order-order nature of the magnetic transition. Taking into account these considerations, it is more plausible that the high magnetic entropy variation listed as an experimental values in Table 3, is really due a collaborative sum of all entropy contributions [10].

To associate with certain the peak entropy of Fig. 9 to the AFM

<sup>5</sup> Temperature for which the entropy peak happens to be in  $\Delta S_{\text{mag}}$

**Table 3**

Comparison of estimated entropy contributions at  $T \approx 350$  K for the harmonic and quasi-harmonic approaches with previous calculations in literature and experimental measurements. It is also indicated for the "Harmonic" (QHA) approach, estimated values at the temperature for which the entropy variation has a peak -  $T = 373$  (316) K.

[JK <sup>-1</sup> kg <sup>-1</sup> ]	Debye model	Harmonic		QHA		Other Calc.	Expt. <sup>a</sup>
		T = 350K	T = 373K	T = 350K	T = 316K		
$\Delta S_{ele}$	—	7.05	7.38	7.16	6.60	11.7 <sup>b</sup> , 11.9 <sup>c</sup>	8 ± 1
$\Delta S_{lat}$	-38.3	6.94	7.05	8.45	9.01	—	-33 ± 9
$\Delta S_{mag}$	—	10.70	10.36	7.93	8.81	14.5 (15.4) <sup>d</sup>	43 ± 9
$\Delta S$	—	24.69	24.78	23.53	24.42	≈ 26.3	17 ± 3

<sup>a</sup> From Ref. [66] at  $T = 328$  K.

<sup>b</sup> From Ref. [12]. Value estimated in a QHA calculation.

<sup>c</sup> From Ref. [8].

<sup>d</sup> From Ref. [18]. In parentheses value at estimated transition temperature,  $T = 371$  K.

→ FM phase transition, we compared the free energies of both phases. However, we did not obtain an intersection of the free energies, at least not in the considered range of temperatures (0–500K). This is in agreement with results of Ref. [12], but in disagreement with the data of Ref. [18]. Theoretically, our results imply that no phase transition can be associated to the discussed entropy peak, making it as pertinent and interesting as the minor entropy dip around 40K. To our knowledge, the latter does not indicate any known transition and most likely reflects the soft phonons of the AFM phase. A comparison between our results and calculations in Ref. [8,12] as well as [18] reveal that the later reference achieves a significantly smaller energy difference between FM and AFM states, around 2.80 meV/atom in comparison to our value; 27 meV/atom. This energy is 35.4 meV/atom in Ref. [12] and 29.1 meV/atom in Ref. [8] for similar calculations. When compared to experiments, the value of Ref. [18] is clearly closer to experimental estimates, which lie around 2.7 meV/atom [26,66]. This improvement of the energy difference estimation between magnetic phases seems to be due to the unique exchange and correlation functional used in Ref. [18]. The authors of this work employed the Langreth-Mehl-Hu functional [74,75], which appears to have as a feature the reduction of energy between phases [76], and suppression of the magnetic moment [77]. Although this functional provides reasonable results for FeRh, it is a less tested functional for general investigations that involve a large group of compounds. In absence of a firm test, this functional is difficult to apply in a predictive study. Another possibility for the too large energy difference between the AFM and FM phase could be due to dynamical correlations of the electronic structure.

If the estimated  $\Delta E_0$  from DFT is used to estimate the entropy variation as  $\Delta S = \Delta U/T$  (as attempted for  $\Delta S_{mag}$ ) we obtain a value of 87.99 JK<sup>-1</sup>kg<sup>-1</sup>. This strong disagreement with experimental measurements also underlines that  $\Delta E_0$  is not properly estimated by DFT.

An important point from this discussion is the difficulty to predict with certainty the temperature for the AFM → FM phase transition. Instead of comparing the free energies of the phases, it is of interest to take a simpler approach and consider the transition to be caused by thermal energy from  $T = \Delta E_0/k_B$ . Using this approach, an estimate of 346 K was obtained in Ref. [8] and 350 K in Refs. [58]. Although this value is within the experimental value, applying the same approach using data from the total energy calculations presented here, or from other calculations [11–13], reveals that this simplified method is very sensitive to the details of the calculations, meaning that its use introduces a non-negligible degree of uncertainty while not describing necessarily the physical picture.

### 3.5. Quasiharmonic approximation

To account for anharmonic interactions we use the QHA, which

minimizes at each temperature the volume-dependent Gibbs free energy:

$$G(V, T) = \min_V [F(V, T) + PV]. \quad (8)$$

In our approach we consider magnetic, electronic and lattice contributions to the free energy  $F(T, V) = E_0(V) + F_{mag}(V, T) + F_{lat}(V, T) + F_{ele}(V, T)$ . Contributions to the lattice and magnetic energy were obtained at constant volume via a calculation of the respective density of states ( $g(\epsilon)_{mag/lat}$ ) and Bose-Einstein distribution function ( $n(\epsilon, T)$ ):

$$F_{mag/lat} = \int \epsilon g(\epsilon)_{mag/lat} n(\epsilon, T) d\epsilon - TS_{mag/lat}. \quad (9)$$

Note that we added the entropy contribution also to this term. These contributions were evaluated, following the same procedure as before, for a series of volumes, and then fitted by cubic splines. For each phase, 9 volumes were considered, including the relaxed volume, ranging the lattice parameter between 2.98 Å (3.00 Å) and 3.00 Å (3.03 Å) for the AFM (FM) phase.  $F_{ele}(V, T)$  was calculated similarly, using instead the Fermi-Dirac distribution function, which includes the temperature dependence of the energy.  $F_{ele}(V, 0)$  was used as reference level for the electronic free energy since the DFT ground state energies are already included in  $E_0(V)$ . The later energies were fitted by the Murnaghan equation of state [78] for the internal energy.

The linear thermal expansion (LTE) obtained from the QHA is shown in Fig. 10. It may be noticed that there is decent agreement with experimental measurements [47] and theory. Similar to the experimental data, there is in our calculations a jump in the LTE at the magnetic phase transition.

We found that contrary to the electronic and lattice contributions, the magnetic contribution to the free energy opposes the volume expansion. Nevertheless, the lattice is the dominant contribution in the considered temperature range and dictates the thermal expansion, and the observed behaviour arises dominantly from the vibrational properties.

The LTE coefficient  $\alpha_l$  can be estimated from a linear fit ( $\Delta l/l = \alpha_l T$ ) in the same temperature range as for the experimental data. From the theory, we obtain a slope of the  $\Delta l/l$  curve that for both the FM and AFM phase is similar to the experimental data. The main difference between theory and experiment is the size of the volume expansion at the magnetic phase transition that is smaller in theory compared to the experimental values [47]. This disagreement is not surprising given the simplicity of the model used and how similar are the values between the magnetic phases.

The volume and temperature dependent free energies of the AFM and FM phases allow for the most accurate estimate of the phase stability and entropy, among the calculations presented in the paper. We compare the QHA and Harmonic results in Table 3,

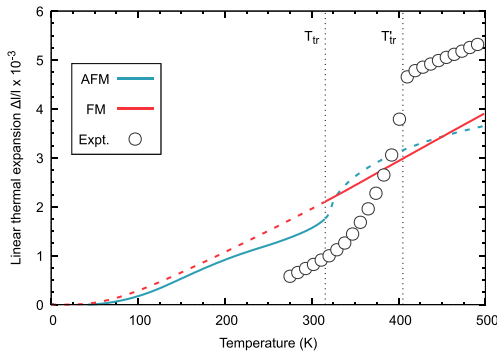


**Fig. 10.** Variation of the linear thermal expansion with temperature for AFM phase (blue line) and FM phase (orange line) obtained within the quasi-harmonic approximation along with experimental measurements (purple circles) [47].  $T_{tr}$  and  $T_{tr}$  indicate respectively the estimated and the measured transition temperature. For interpretation of the references to color in this figure legend, the reader is referred to the Web version of this article.

together with previously reported data. It may be seen that the total entropy change of the AFM  $\rightarrow$  FM phase transition is almost insensitive to the level of approximation, while for the individual contributions there is a more significant difference between the QHA and Harmonic approximations.

We find that there is compensation of  $\Delta S_{lat}$  and  $\Delta S_{mag}$ , which vary similarly but in opposite direction, as can be seen by comparing the entropy contributions on Table 3. This is caused by variation of  $|J_{ij}|$  parameters with volume, which decreases for bigger volumes. As reported also in Ref. [19], we also observe that couplings between iron moments are significantly more sensitive to this variation than couplings between iron and rhodium magnetic moments (data not shown).

The predicted volume variation in the AFM is responsible for the loss of the monotonous behaviour of  $\Delta S_{lat}$  in the transition range. Since the linear thermal expansion behaves as experimentally measured, and the entropy peak reassembles more the discontinuity expected for first order transitions, we consider that there is a qualitative improvement of the physical description. Besides becoming sharper, the broader entropy peak shifts from 373K to 316K when using the QHA, as seen in Fig. 9.

Our results are close to previous, similar first-principles calculations, combining the QHA results of Ref. [12] (or the ones from Ref. [8]) for  $\Delta S_{ele} + \Delta S_{lat}$  with the results of Ref. [18]. Although there is a small deviation, it is accurate enough to be used in high-throughput calculations, keeping in mind that a more accurate result would need a more tailored and computationally expensive method. Also, we treated entropy contributions as independent, which is a simplification of the problem.

#### 4. Conclusions

The aim of this paper is to derive a reliable approach based on first principles calculations to determine the entropy change in materials with first order phase transition that can be used in high throughput studies. Thus we have to balance between computational effort and accuracy and a detailed study, concerning estimates for electronic, lattice and magnetic entropy contributions according to different models, was performed using the well-known MCE system FeRh as test material. Based on the assumption that we can treat the entropy as a sum of three independent parts, i.e. handle the electronic, lattice, and magnetic contributions

to the entropy separately, we tested different approximations for each entropy contribution. It turned out that the entropy, or the entropy change, in our test case, FeRh, is very sensitive to approximations made, e.g., even small alterations on elastic properties between the two magnetic phases need to be taken into account for a reliable estimation of the entropy. This means that the Debye model is not adequate and it should not be considered for the high-throughput applications. Although the simplicity of the Debye model is appealing in terms of computational efficiency, it fails to estimate the vibrational entropy in the presence of soft phonon modes. We believe that this sensitivity regarding the vibrational properties is not exclusive to FeRh. Rather, we expect that many of the magnetocaloric candidates will show similar behaviour, which means that accurate phonon calculations are necessary for a reliable description of the entropy.

From the results of the magnetic properties, we conclude that it is necessary to consider an appropriate cutoff for the exchange interactions when using a spin-wave description due to the possibility of long-range interactions, which can have a considerable influence. However, this aspect should be less relevant in case of order-disorder magnetic transitions where spin-flip like excitations are dominant and the Heisenberg model can be used in combination with Monte Carlo simulations to estimate the magnetic entropy.

We observe an entropy peak around the expected transition temperature raised solely from the magnetic contribution, which allows us to support the picture of a magnetism driven transition as discussed in previous works using different approaches [13,16,18,58].

Although a  $\Delta S$  peak is regularly observed in phase transitions, it is necessary to compare the free energies of the phases to associate a  $\Delta S$  peak to a phase transition. For FeRh, it was not possible to establish this association due to the overestimation of the energy difference between magnetic phases by traditional DFT. Such difficulty raised our awareness of this limitation in our first-principles approach. Nevertheless, beyond DFT methods offer tools for circumventing this problem, and can be used to improve  $\Delta E_0$  estimation to verify the transition occurrence, if needed.

Adopting the QHA approach allows for a more complete description of the systems and a qualitative improvement of the entropy variation is obtained, by the sharpening of the  $\Delta S$  peak as expected for a first-order transition. Despite this, no quantitative improvement of the entropy variation is obtained that justifies the significant increase of computational effort required for this treatment.

Therefore, it can be stated that the ‘‘Harmonic’’ approach balances in a very satisfactory way the accuracy and the computational effort. The obtained results  $\Delta S_{ele} = 7.38 \text{ JK}^{-1}\text{kg}^{-1}$ ,  $\Delta S_{lat} = 7.05 \text{ JK}^{-1}\text{kg}^{-1}$ , and  $\Delta S_{mag} = 10.36 \text{ JK}^{-1}\text{kg}^{-1}$  are in good agreement with previous calculations and the total entropy variation  $\Delta S = 24.78 \text{ JK}^{-1}\text{kg}^{-1}$  is close to the experimental range. This establishes the cornerstones for a reliable entropy estimation at high-throughput scale computations, while allowing for reasonable computational effort that allows to avoid possible pitfalls of the calculations.

#### CRediT authorship contribution statement

**R. Martinho Vieira:** Conceptualization, Investigation, Formal analysis, Writing - original draft, Visualization. **O. Eriksson:** Supervision, Writing - review & editing, Project administration, Funding acquisition. **A. Bergman:** Software, Writing - review & editing. **H.C. Herper:** Supervision, Conceptualization, Resources, Writing - review & editing.

## Declaration of competing interest

The authors declare that they have no known competing financial interests or personal relationships that could have appeared to influence the work reported in this paper.

## Acknowledgments

The authors would like to thank Yaroslav Kvashnin for the fruitful discussions regarding magnetic simulations and estimation of the exchange parameters. We are also grateful for the helpful comments from the reviewers which allowed for a clearer and more complete text. The computations were enabled by resources provided by the Swedish National Infrastructure for Computing (SNIC) at UPPMAX, NSC and HPC2N partially funded by the Swedish Research Council through grant agreement no. 2016–07213. This work was supported by the Swedish Foundation for Strategic Research, within the project Magnetic Materials for Green Energy Technology (ref. EM16-0039), StandUPP, eSENCE, the Swedish Energy Agency (Energimyndigheten) as well as Vetenskapsrådet.

## Appendix A. Supplementary data

Supplementary data to this article can be found online at <https://doi.org/10.1016/j.jallcom.2020.157811>.

## References

- A.M. Tishin, Y.I. Spichkin, The Magnetocaloric Effect and its Applications, IOP Publishing Ltd, 2003.
- K.G. Sandeman, *Scripta Mater.* 67 (2012) 566–571.
- N.A. Zarkevich, D.D. Johnson, V.K. Pecharsky, *J. Phys. Appl. Phys.* 51 (2018), 024002.
- T. Gottschall, K.P. Skokov, M. Fries, A. Taubel, I. Radulov, F. Scheibel, D. Benke, S. Riegg, O. Gutfleisch, *Advanced Energy Materials* 9 (2019).
- N.A. Zarkevich, V.I. Zverev, *Crystals* 10 (2020) 815.
- S. Curtarolo, G.L. Hart, M.B. Nardelli, N. Mingo, S. Sanvito, O. Levy, *Nat. Mater.* 12 (2013) 191–201.
- C. Ortiz, O. Eriksson, M. Klüntenberg, *Comput. Mater. Sci.* 44 (2009) 1042–1049.
- N.A. Zarkevich, D.D. Johnson, *J. Alloys Compd.* 802 (2019) 712–722.
- E. Brück, *J. Phys. Appl. Phys.* 38 (2005) R381–R391.
- F. Scheibel, T. Gottschall, A. Taubel, M. Fries, K.P. Skokov, A. Terwey, W. Keune, K. Ollefs, H. Wende, M. Farle, M. Acet, O. Gutfleisch, *M.E. Gruner, Energy Technol.* 6 (2018) 1397–1428.
- V.L. Moruzzi, P.M. Marcus, *Phys. Rev. B* 46 (1992) 2864–2873.
- M. Wolloch, M.E. Gruner, W. Keune, P. Mohn, J. Redinger, F. Hofer, D. Suess, R. Podloucky, J. Landers, S. Salamon, F. Scheibel, D. Spoddig, R. Witte, B. Roldan Cuena, O. Gutfleisch, M.Y. Hu, J. Zhao, T. Toellner, E.E. Alp, M. Siewert, P. Entel, R. Pentcheva, H. Wende, *Phys. Rev. B* 94 (2016), 174435.
- M.E. Gruner, E. Hoffmann, P. Entel, *Phys. Rev. B* 67 (2003), 064415.
- N.A. Zarkevich, D.D. Johnson, *Phys. Rev. B* 97 (2018), 014202.
- U. Aschauer, R. Braddell, S.A. Brechbühl, P.M. Derlet, N.A. Spaldin, *Phys. Rev. B* 94 (2016), 014109.
- J.B. Staunton, R. Banerjee, M.d.S. Dias, A. Deak, L. Szunyogh, *Phys. Rev. B* 89 (2014), 054427.
- L.M. Sandratskii, P. Mavroupos, *Phys. Rev. B* 83 (2011), 174408.
- R.Y. Gu, V.P. Antropov, *Phys. Rev. B* 72 (2005), 012403.
- J. Kudrnovský, V. Dřchal, I. Turek, *Phys. Rev. B* 91 (2015), 014435.
- A. Szajek, J.A. Morkowski, *Physica B: Phys. Condens. Matter* 193 (1994) 81–91.
- M. Pugacheva, J.A. Morkowski, A. Jezierski, A. Szajek, *Solid State Commun.* 92 (1994) 731–734.
- Y.-m. Zhou, X. Gao, D.-s. Wang, *J. Magn. Magn. Mater.* 226–230 (2001) 1042–1044.
- P. Tu, A.J. Heeger, J.S. Kouvel, J.B. Comly, *J. Appl. Phys.* 40 (1969) 1368–1369.
- C. Koenig, *J. Phys. F Met. Phys.* 12 (1982) 1123–1137.
- S. Polesya, S. Mankovsky, D. Ködderitzsch, J. Minár, H. Ebert, *Phys. Rev. B* 93 (2016), 024423.
- B.K. Ponomarev, *Sov. Phys. JETP* 36 (1973) 105–107.
- A. Castets, D. Tocchio, H. Hennion, *Phys. B+C* 86–88 (1977) 353–355.
- L.H. Lewis, C.H. Marrows, S. Langridge, *J. Phys. Appl. Phys.* 49 (2016) 323002.
- A. Chirkova, K. Skokov, L. Schultz, N. Baranov, O. Gutfleisch, T. Woodcock, *Acta Mater.* 106 (2016) 15–21.
- E. Valiev, R. Gimaev, V. Zverev, K. Kamilov, A. Pyatakov, B. Kovalev, A. Tishin, *Intermetallics* 108 (2019) 81–86.
- C. Sánchez-Valdés, R. Gimaev, M. López-Cruz, J. Sánchez Llamazares, V. Zverev, A. Tishin, A. Carvalho, D. Aguiar, Y. Mudryk, V. Pecharsky, *J. Magn. Magn. Mater.* 498 (2020), 166130.
- C. Kittel, *Phys. Rev.* 120 (1960) 335–342.
- J.S. Kouvel, C.C. Hartelius, *J. Appl. Phys.* 33 (1962) 1343–1344.
- J.S. Kouvel, *J. Appl. Phys.* 37 (1966) 1257–1258.
- R. Barua, F. Jiménez-Villacorta, L.H. Lewis, *J. Appl. Phys.* 115 (2014) 17A903.
- M.J. Jiménez, A.B. Schvval, G.F. Cabeza, *Comput. Mater. Sci.* 172 (2020), 109385.
- J. Kim, R. Ramesh, N. Kioussi, *Phys. Rev. B* 94 (2016) 180407.
- G. Kresse, J. Hafner, *J. Phys. Condens. Matter* 6 (1994) 8245–8257.
- G. Kresse, J. Hafner, *Phys. Rev. B* 49 (1994) 14251–14269.
- G. Kresse, J. Furthmüller, *Comput. Mater. Sci.* 6 (1996) 15–50.
- P.E. Blöchl, *Phys. Rev. B* 50 (1994) 17953–17979.
- G. Kresse, D. Joubert, *Phys. Rev. B* 59 (1999) 1758–1775.
- A. Togo, I. Tanaka, *Scripta Mater.* 108 (2015) 1–5.
- J.M. Wills, O. Eriksson, P. Andersson, A. Delin, O. Grechnev, M. Alouani, *Full-Potential Electronic Structure Method, Volume 167 of Springer Series in Solid-State Sciences*, Springer Berlin Heidelberg, Berlin, Heidelberg, 2010.
- O. Eriksson, A. Bergman, L. Bergqvist, J. Hellsvik, *Atomistic Spin Dynamics*, vol. 1, Oxford University Press, Oxford, 2017.
- J.P. Perdew, K. Burke, M. Ernzerhof, *Phys. Rev. Lett.* 77 (1996) 3865–3868.
- M.R. Ibarra, P.A. Algarabel, *Phys. Rev. B* 50 (1994) 4196–4199.
- A.I. Zakharov, A.M. Kadomtseva, R.Z. Levitin, E.G. Ponyatovskii, *Sov. Phys. JETP* 19 (1964) 1348–1353.
- G. Shirane, C.W. Chen, P.A. Flinn, R. Nathans, *J. Appl. Phys.* 34 (1963) 1044–1045.
- G. Shirane, R. Nathans, C.W. Chen, *Phys. Rev.* 134 (1964) A1547.
- A. Liechtenstein, M. Katsnelson, V. Antropov, V. Gubanov, *J. Magn. Magn. Mater.* 67 (1987) 65–74.
- M.I. Katsnelson, A.I. Liechtenstein, *Phys. Rev. B* 61 (2000) 8906–8912.
- Y.O. Kvashnin, O. Grånäs, I. Di Marco, M.I. Katsnelson, A.I. Liechtenstein, O. Eriksson, *Phys. Rev. B Condens. Matter* 91 (2015) 1–10.
- G. Grimvall, *Thermophysical Properties of Materials*, Elsevier, 1999.
- Y.O. Kvashnin, R. Cardias, A. Szilva, I. Di Marco, M.I. Katsnelson, A.I. Liechtenstein, L. Nordström, A.B. Klautau, O. Eriksson, *Phys. Rev. Lett.* 116 (2015) 217202.
- A. Sommerfeld, *Z. Phys.* 47 (1928) 1–32.
- L. Jia, G.J. Liu, J.R. Sun, H.W. Zhang, F.X. Hu, C. Dong, G.H. Rao, B.G. Shen, *J. Appl. Phys.* 100 (2006), 123904.
- P.M. Derlet, *Phys. Rev. B* 85 (2012), 174431.
- J. Barker, R.W. Chantrell, *Phys. Rev. B* 92 (2015), 094402.
- V.L. Moruzzi, J.F. Janak, K. Schwarz, *Phys. Rev. B* 37 (1988) 790–799.
- A.E. Petrova, V.N. Krasnorussky, A.A. Shikov, W.M. Yuhasz, T.A. Lograsso, J.C. Lashley, S.M. Stishov, *Phys. Rev. B* 82 (2010), 155124.
- R. Stern, S. Willoughby, A. Ramirez, J. MacLaren, J. Cui, Q. Pan, R.D. James, *J. Appl. Phys.* 91 (2002) 7818–7820.
- S.O. Kart, T. Çağın, *J. Alloys Compd.* 508 (2010) 177–183.
- H. Rached, D. Rached, R. Khenata, A.H. Reshak, M. Rabah, *Phys. Status Solidi* 246 (2009) 1580–1586.
- C. Soykan, S.O. Kart, C. Sevik, T. Çağın, *J. Alloys Compd.* 611 (2014) 225–234.
- D.W. Cooke, F. Hellman, C. Baldasseroni, C. Bordel, S. Moyerman, E.E. Fullerton, *Phys. Rev. Lett.* 109 (2012), 255901.
- P. Ravindran, L. Fast, P.A. Korzhavyi, B. Johansson, J. Wills, O. Eriksson, *J. Appl. Phys.* 84 (1998) 4891–4904.
- P. Söderlind, O. Eriksson, J.M. Wills, A.M. Boring, *Phys. Rev. B* 48 (1993) 5844–5851.
- H.C. Herper, E. Hoffmann, P. Entel, *Phys. Rev. B* 60 (1999) 3839–3848.
- P. Souvatzis, O. Eriksson, M. Katsnelson, S. Rudin, *Phys. Rev. Lett.* 100 (2008), 095901.
- M.P. Annaorazov, K.A. Asatryan, G. Myalikgulyev, S.A. Nikitin, A.M. Tishin, A.L. Tyurin, *Cryogenics* 32 (1992) 867–872.
- E. Stern-Taulats, A. Planes, P. Lloveras, M. Barrio, J.L. Tamarit, S. Pramanick, S. Majumdar, C. Frontera, L. Mañosa, *Phys. Rev. B Condens. Matter* 89 (2014), 214105.
- M.J. Richardson, D. Melville, J.A. Ricodeau, *Phys. Lett.* 46 (1973) 153–154.
- D.C. Langreth, M. Mehl, *Phys. Rev. B* 28 (1983) 1809.
- C. Hu, D.C. Langreth, *Phys. Scripta* 32 (1985) 391.
- D.J. Singh, J. Ashkenazi, *Phys. Rev. B* 46 (1992) 11570–11577.
- F. Amalou, H. Bouzar, M. Benakki, A. Mokrani, C. Demangeat, G. Moraitis, *Comput. Mater. Sci.* 10 (1998) 273–277 (Computational Modelling of Issues in Materials Science).
- F.D. Murnaghan, *Proc. Natl. Acad. Sci. Unit. States Am.* 30 (1944) 244. LP – 247.

# Supplementary Material: High-throughput compatible approach for entropy estimation in magnetocaloric materials: FeRh as a test case

R. Martinho Vieira<sup>1,\*</sup>, O. Eriksson<sup>1,2</sup>, A. Bergman<sup>1</sup>, H. C. Herper<sup>1</sup>

<sup>1</sup>Department of Physics and Astronomy, Uppsala University, Box 516, SE-75120 Uppsala, Sweden

<sup>2</sup>School of Science and Technology, Örebro University, SE-701 82 Örebro, Sweden

## 1 MDOS variation

From the data in Figure S1 one can trace back the sensitivity of the magnetic entropy peak (Fig. 4 on the article) to changes on the magnon density of states (MDOS) of the ferromagnetic phase (FM). For the anti-ferromagnetic phase (AFM), the inclusion of magnetic exchange interactions with sites within a radius of 6.0 lattice parameters seems to be already enough to have a converged MDOS, comparatively to the result with a cutoff of 12.0  $a$ . The same behaviour is not found for the FM phase, where we can observe higher sensitivity of MDOS to the cutoff of included exchange interactions, especially in the lower energy region ( $< 150$  meV). Besides the existence of small shifts on the MDOS, there are significant alterations on the two first peaks, becoming the first peak sharper at the cost of the second as more exchange interactions are taken in consideration. We can justify such behaviour as a consequence of the increase of weaker interactions included in the calculations which will allow more magnon modes at low energies and therefore an increase of the first peak.

This initial peak in the FM phase might be closely associated to the mechanism which drives the meta-magnetic transition, since it occurs around 257 K (22.15 meV), very close to the temperature of the estimated magnetic entropy peak (316 K). While a more detailed analysis and careful calculations are necessary to verify this association, it would be a strong argument in favour of the current paradigm that small magnetic fluctuations are responsible by the stabilization of the ferromagnetic phase of FeRh.



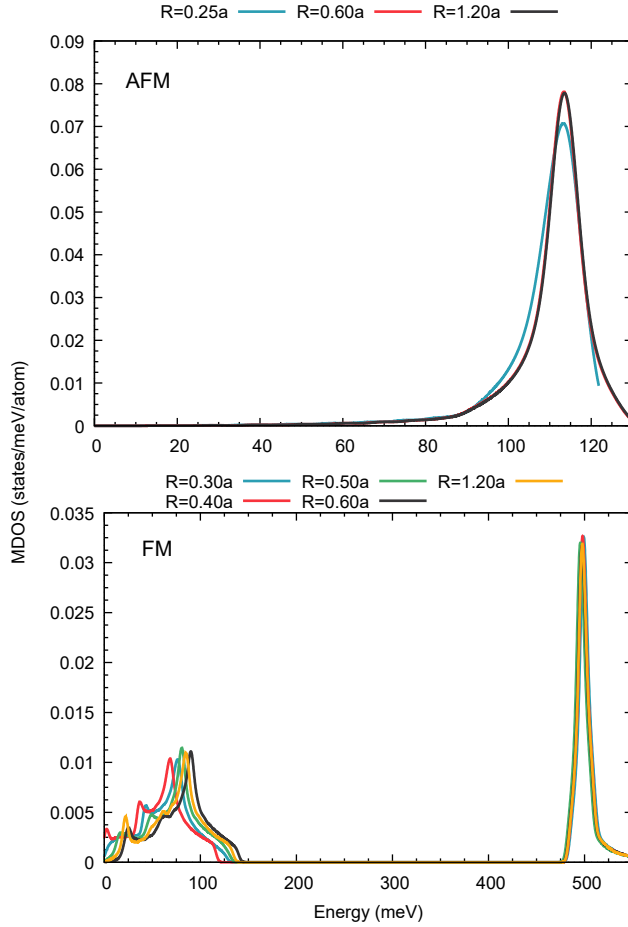


Figure S1: Variation of the magnon density of states according with the cutoff radius of included interactions (in lattice parameter units). Results calculated for the FM (AFM) phase with  $a = 3.014\text{\AA}$  ( $a = 2.998\text{\AA}$ )



**Realistic first-principles calculations of the magnetocaloric effect:  
applications to hcp Gd**

Rafael Martinho Vieira, Olle Eriksson, Torbjörn Björkman, Anders  
Bergman, Heike C. Herper

*Mater. Res. Lett.* 10, 156–162 (2022)



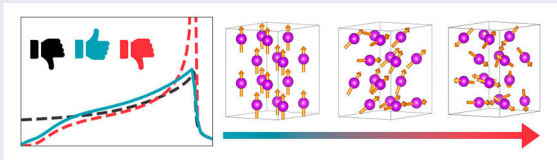
# Realistic first-principles calculations of the magnetocaloric effect: applications to hcp Gd

R. Martinho Vieira <sup>a,b</sup>, O. Eriksson <sup>a,c</sup>, T. Björkman <sup>b</sup>, A. Bergman <sup>a</sup> and H. C. Herper <sup>a</sup>

<sup>a</sup>Department of Physics and Astronomy, Uppsala University, Uppsala, Sweden; <sup>b</sup>Physics, Faculty of Science and Engineering, Åbo Akademi University, Turku, Finland; <sup>c</sup>School of Science and Technology, Örebro University, Örebro, Sweden

## ABSTRACT

We present an efficient computational approach to evaluate field-dependent entropy of magnetocaloric materials from *ab-initio* methods. The temperature dependence is reported for the entropy change, specific heat and magnetization for hcp Gd. To obtain optimal accuracy in the calculations, a mixed-scheme for magnetic Monte Carlo simulations is proposed and found to be superior to using pure quantum or classic statistics. It is demonstrated that lattice and magnetic contributions play a role in the entropy change and that the dominating contribution comes from the magnetic contribution. The total calculated entropy change agrees with measurements at room temperature.



## IMPACT STATEMENT

Demonstration of the accuracy of *ab-initio* theory, coupled to statistical methods, for accurate calculations of the total entropy variation associated with the magnetic transition of Gd. Reproduction of experimental data of entropy change.

## ARTICLE HISTORY

Received 19 November 2021

## KEYWORDS

Magnetocaloric; Gd; entropy; Monte Carlo; mixed statistics

## 1. Introduction

Historically, Gd-based compounds were in the center of the development of magnetic refrigeration devices operating at room temperature. In fact, metallic Gd was the magnetic refrigerant of the first magnetic refrigerator device, a choice motivated by its Curie temperature ( $T_C \approx 290$  K) close to room temperature and a great magnetocaloric response [1]. Another important mark of this field is the observation in 1997 of a giant magnetocaloric effect (MCE) in  $Gd_5(Si_2Ge_2)$  by Pecharsky and Gschneidner [2], which captured the attention of the scientific community for the magnetic cooling technology and pushed the field forward. Due to these landmark results, and the availability of multiple studies in the literature, the magnetocaloric community takes bulk Gd as a reference for comparing the performance of the MCE in materials [3–6]. The entropy variation ( $\Delta S$ ) is the most important parameter to characterize the MCE and the

performance of magnetic materials in magnetic cooling devices.

The MCE is a response of an applied field, and the magnetic contribution to the entropy change ( $S_{\text{mag}}$ ) is expected to be the dominant term, although it is established that the lattice ( $S_{\text{lat}}$ ) and electronic ( $S_{\text{ele}}$ ) contributions are also relevant [7–9]. For this reason, the entropy can be accurately described as the sum of three different contributions viewed as independent terms:  $\Delta S = \Delta S_{\text{ele}} + \Delta S_{\text{mag}} + \Delta S_{\text{lat}}$ . However, note that for simplicity, couplings between the system's degrees of freedom are not included in this approach, despite their relevance for magnetocalorics.

In this work, we study the MCE in the hexagonal closed packed form (hcp) of Gd, focusing on the calculation of  $\Delta S$  from first-principles calculations and Monte Carlo (MC) simulations. Along with these calculations, we introduce and test the performance of a new scheme

**CONTACT** R. Martinho Vieira rafael.vieira@physics.uu.se Department of Physics and Astronomy, Uppsala University, Box 516, SE-75120 Uppsala, Sweden Physics, Faculty of Science and Engineering, Åbo Akademi University, FI-20500 Turku, Finland

Supplemental data for this article can be accessed here. <https://doi.org/10.1080/21663831.2022.2033866>

© 2022 The Author(s). Published by Informa UK Limited, trading as Taylor & Francis Group  
This is an Open Access article distributed under the terms of the Creative Commons Attribution License (<http://creativecommons.org/licenses/by/4.0/>), which permits unrestricted use, distribution, and reproduction in any medium, provided the original work is properly cited.

for MC simulations, which combines quantum and classic statistics to obtain an improved description over a wide temperature range.

## 2. Materials and methods

### 2.1. Mixed-statistics Monte Carlo method

Traditionally, magnetic MC simulations use the Boltzmann distribution to emulate and regulate the thermal fluctuations at finite temperatures. While this approach is suitable to simulate order-disorder transitions, it neglects quantum effects on the fluctuations, thus becoming less accurate for lower temperatures. A well-known example of such failure is the resulting heat capacity of

$1 k_B$  in the limit  $T \rightarrow 0$  (see Figure 1(a)), which is in accordance with the classical equipartition theorem<sup>1</sup>, but in disagreement with experimental observations. At low temperatures, quantum effects become relevant and must be included in fluctuations of any appropriate approach.

With that intent, previous works have developed methods to capture the correct behavior at low temperatures. For example, in Ref. [10], a quantum scaling factor of the probability density at temperature  $T$  is introduced so the transition probability between MC states is driven by quantum statistics. Effectively [11,12], this approach corresponds to an effective rescaling of the simulation temperature ( $T$ ) defined from the average energy of the magnons ( $E_{\text{mag}}$ ), calculated using the density of states of

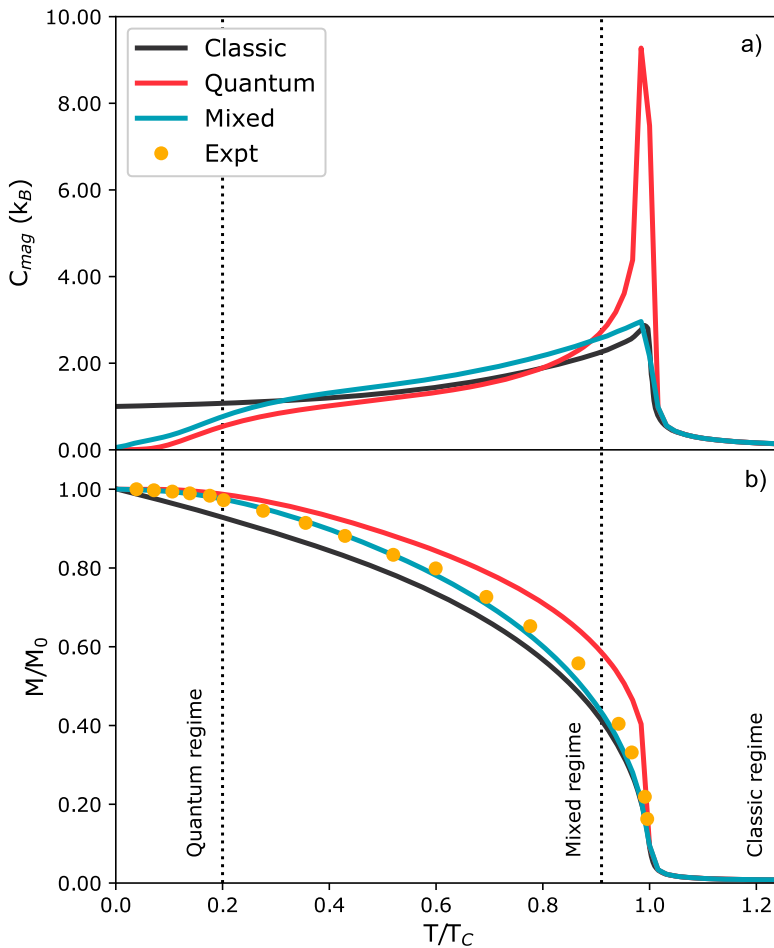


**Figure 1.** Temperature-dependent magnetization derived from MC simulations of hcp Gd using different statistical approaches. Temperature is normalized according to  $T_C$  of the experimental (293 K) and calculated (315 K) data. Experimental data extracted from Ref. [25].

the magnons (MDOS) and Bose–Einstein statistics at a certain  $T$ , as:  $T_{\text{qt}} = \langle E_{\text{mag}} \rangle(T)/k_B$ .

Despite a significant improvement at low temperatures (shown in Figure 1), this quantum treatment sharpens the systems behavior around  $T_C$ , as is evident in the resulting magnetization (Figure 1(b)) and heat capacity peak (Figure 1(a)). Such effect is not exclusive of Gd as similar results were obtained in analogous calculations [10,11,13]. An explanation for these results might come from the use of a quasi-harmonic approximation (see more details in Refs. [10,11]) to calculate a temperature-dependent MDOS from the adiabatic magnon spectra. This approximation should only be valid at low temperatures, while not being accurate close to  $T_C$  [11].

Comparing the methods based on classic and quantum statistics, we note that they are suitable in the  $T \rightarrow T_C$  and  $T \rightarrow 0$  limits, respectively. However, both have reduced accuracy when used outside these regions. These limitations constitute a problem for simulations over a wide temperature range. In particular, for quantities derived from integration over the whole temperature range, such as the entropy:

$$S_{\text{mag}}(T) = \int_0^T \frac{C_{\text{mag}}}{T} dT. \quad (1)$$

To tackle this issue, we propose a simulation scheme that combines quantum and classic statistics to improve the practical issues observed.

Generally, in MC simulations, the sampling of magnetic configurations is performed using the transition probability between MC states ( $W$ ). This probability depends on the sampling method. Commonly in MC simulations, the Metropolis algorithm is considered, where the state transition probability between configurations is defined as:

$$W = \begin{cases} \exp\left(-\frac{\Delta E}{k_B T}\right), & \text{if } \Delta E > 0 \\ 1, & \text{otherwise} \end{cases} \quad (2)$$

with  $\Delta E$  as the energy difference between states.

In the mixed method used here, we combine the transition probability calculated in the quantum scheme,  $W(\Delta E, T_{\text{qt}})$ , with the transition probability calculated in the classical approach  $W(\Delta E, T)$  as a weighted average:

$$W_{\text{mix}}(\Delta E, T) = \alpha W(\Delta E, T_{\text{qt}}) + (1 - \alpha) W(\Delta E, T) \quad (3)$$

where  $\alpha$  is the weight factor. This weight factor should be temperature-dependent so that at low temperatures, the  $W(\Delta E, T_{\text{qt}})$  quantum contribution is dominant, and near  $T_C$  the  $W(\Delta E, T)$  classic contribution becomes dominant. Furthermore,  $\alpha$  should be defined by a smooth

function to avoid a sharp transition between the two statistics schemes. With this in mind, we propose an  $\alpha$  with the following temperature behavior:

$$\alpha = \begin{cases} 1 - \frac{T}{T_C}, & T \leq T_C \\ 0, & T \geq T_C \end{cases} \quad (4)$$

This choice is the most straightforward function that satisfies the necessary conditions with the advantage of not needing additional free parameters than  $T_C$ , which is also required for the quantum simulations and can be calculated using classic MC simulations. The factor  $\alpha$  also enters in the rescaling of the MDOS used for the pure quantum statistics method [11].

## 2.2. Computational details

The half-filled  $4f$  shell of Gd is responsible for its large magnetic moment and strongly correlated electronic structure. However, since these orbitals are highly localized, the overlap between neighboring atomic sites is negligible, being the magnetic interactions ruled by the  $6s$ ,  $6p$  and  $5d$  states [14]. Despite the high localization of the  $4f$  states, the correct treatment of these orbitals, in first-principles calculations, is a topic of discussion since standard calculations for the ferromagnetic configuration (FM) predict a non-physical hybridization of these states with the remaining valence states near the Fermi energy. Some of the most efficient approaches in the literature are treating the  $f$ -states as spin-polarized core states or using the LDA+U correction [14,15].

In the paramagnetic configuration (PM), the magnetization averages to zero while retaining the local magnetic moment. Non-spin-polarized calculations fail to reproduce this picture since they constrain the degree of freedom of the spin. Usually, more sophisticated approaches as the disordered local moments (DLM) approximation are necessary to describe this magnetic state. However, for Gd, it is reasonable to assume that a calculation with the  $f$ -states treated as non-spin-polarized core states is a good approximation since the dispersing valence electron states are treated without a polarizing field generated by the highly localized  $f$ -states, which is consistent with the zero averaged magnetization of the PM state. Comparison of the density of states (DOS) calculated in this setup against a DLM calculation supports the validity of this approach (see Supplement).

Additionally, we know from the results of similar calculations [15] that in Gd the electronic and magnetic properties are better described by LDA exchange-correlation potentials. In contrast, the structural properties benefit from the use of GGA.

The structural and magnetic properties of hcp Gd were determined from first-principles calculations of the electronic structure using the VASP package [16–19] and RSPt software [20]. The PHONOPY [21] package was utilized to compute the vibrational density of the states. For calculating the electronic structure of disordered magnetic phases, we considered the DLM method by utilizing the SPR-KKR code [22]. From the DFT calculations, the magnetic moments and the  $J_{ij}$  exchange couplings (within the Lichtenstein–Katsnelson–Antropov–Gubanov formalism [23]) were determined and used as input for the MC simulations. We performed the magnetic MC simulations using an atomistic Heisenberg Hamiltonian:

$$\mathcal{H} = - \sum_{i \neq j} J_{ij} \mathbf{m}_i \cdot \mathbf{m}_j - \sum_i \mathbf{H} \cdot \mathbf{m}_i \quad (5)$$

in the UppASD code [24]. The Hamiltonian in Equation (5) describes the pair exchange interactions between atomic magnetic moments ( $\mathbf{m}$ ) in different sites and the interaction of the magnetic moments with the magnetic field ( $\mathbf{H}$ ), respectively. In the Supplement, we provide more complete details on the setup of the calculations.

### 3. Results and discussion

#### 3.1. Monte Carlo simulations

The proposed mixed scheme captures the behavior of the quantum scheme at low temperatures and it correctly describes the classical limit showing the same behavior as the classical approach at  $T \rightarrow T_C$  as can be seen from the MC simulation of the temperature-dependent magnetism, see Figure 1. Such convergence of results from the mixed to the quantum scheme at  $T \rightarrow 0$  and convergence to the classic scheme at  $T \rightarrow T_C$  is guaranteed by the mixing weight choice (see Equation (4)).

The success of the mixed method becomes clear by comparing the magnetization curves (Figure 1(b)) with experimental results. In particular, it should be noted that at intermediate temperatures the mixed-scheme calculations are very close to the experimental measurements [25].

Comparing the magnetization obtained from simulations with the experimental data allows to determine the temperature ranges in which the quantum and classic descriptions are more adequate, see Figure 1. From this figure, the existence of an intermediate regime in which the actual magnetization lies between the classic and quantum regimes can be seen. This implies that in this region the origin of the magnetic fluctuations is different, and possibly that both quantum and classic excitations co-exist. The success of the mixed-statistics

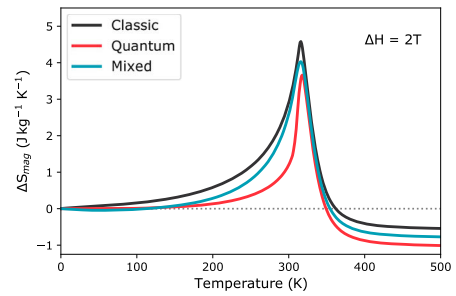


**Figure 2.** Temperature-dependent magnetic entropy variation from MC simulations using different statistics schemes. For a detailed description of the mixed scheme, see text.

scheme suggests that it is the latter case, or at least that the experimental observations can be more satisfactorily be reproduced by this description.

Since the primary goal of this study is to calculate the entropy change of hcp Gd when an applied magnetic field is present, it is worth discussing how the proposed scheme compares with the conventional classic statistics (see Figure 2). We calculated the variation of the entropy of the MCE from the heat capacity difference between a simulation without an applied magnetic field and a simulation with an applied field of 2T:

$$\Delta S_{\text{mag}}(H, T) = \int_0^T \frac{C_{\text{mag}}(H, T) - C_{\text{mag}}(0, T)}{T} dT \quad (6)$$

As Figure 2 shows there is in all three methods a peak of  $\Delta S_{\text{mag}}$  at the ordering temperature. This property is of primary interest to this investigation. Although the different approaches used here give different results of the  $M(T)$  curves and the specific heat (see Figure 1) we note that the observed variations of the entropy change (Figure 2) are small. This suggests no significant reasons to adopt the mixed scheme described above, over the conventional MC simulations. Nevertheless, it is important to note the existence of substantial changes in the entropy at  $T < T_C$ , in the quantum and mixed regimes, which can be crucial to consider in the study of phase stability in more complex materials.

#### 3.2. Electronic and lattice entropy contributions

Based on the conclusions from a previous study [26], the electronic entropy,  $S_{\text{ele}}$ , was calculated from the Sommerfeld approximation while the lattice entropy,  $S_{\text{lat}}$ , was obtained from full phonon calculations using the ground state properties of each magnetic phase.

It is necessary to consider all intermediate states between the fully ordered and fully disordered magnetic



configurations to describe the entropy variation accurately. To achieve this, we determined the magnetization dependence of  $S_{\text{ele}}$  and  $S_{\text{lat}}$  such that these quantities could be related to the magnetization-temperature curves from the MC simulations (Figure 1). For this purpose, we calculated the Sommerfeld coefficient for intermediate magnetic configurations, by adjusting the net spin moments of DLM calculations to coincide with the data of Figure 1. Doing this, we obtained a continuous value of the Sommerfeld coefficient, as a function of the magnetization, allowing us to calculate  $S_{\text{ele}}(M)$ , and from there  $S_{\text{ele}}(T)$ . To avoid the appearance of numerical artifacts in  $S_{\text{ele}}$ , we applied a trend-conserving smoothing filter on the original data, see more details in the Supplement.

We performed a similar treatment for  $S_{\text{lat}}$ , but in this case, for practical reasons of treating magnetic configurations of intermediate disorder, we made use of the virtual crystal approximation. This approximation is often used to calculate phonon properties in alloys since it simplifies the calculation of the properties of the alloy to compositionally weighted averages of the properties of the pure systems [27]. Similarly to chemically disordered alloys, the intermediate magnetic configurations between the PM and FM phases can be treated as mixing of these phases ( $\text{FM}_x + \text{PM}_{1-x}$ ). Within this picture, we determine  $S_{\text{lat}}$  as:

$$S_{\text{lat}}(M, T) = \frac{M(T)}{M_0} S_{\text{FM}}(T) + \left(1 - \frac{M(T)}{M_0}\right) S_{\text{PM}}(T) \quad (7)$$

where  $S_{\text{FM}}$  and  $S_{\text{PM}}$  were calculated from phonon density of states of the ferromagnetic spin-polarized and the unpolarized DFT calculations, respectively. Having derived a formalism for the  $S_{\text{ele}}(M)$  and  $S_{\text{lat}}(M)$ , we computed the entropy variation using the simulated magnetization curves for the  $H=0$  and  $H=2$  T cases:  $\Delta S = S(H=2) - S(H=0)$ . The results are shown in Figure 3. While the electronic contribution now becomes negligible in agreement with the expectations, the lattice contribution is still surprisingly large for a 2nd order transition without structural changes.

### 3.3. Total entropy variation

Comparison between the distinct entropy contributions, see Figure 4, reveals that the magnetic term is dominant, followed by a lattice contribution that is almost as large. Together with the small electronic contribution, they add up to the total entropy, that has a peak at the transition temperature. When comparing to experimental data, we note a decent agreement: theory gives a value of 7.56 J/kg/K at the ordering temperature (which is  $\sim 320$  K in the present calculations) while the measured

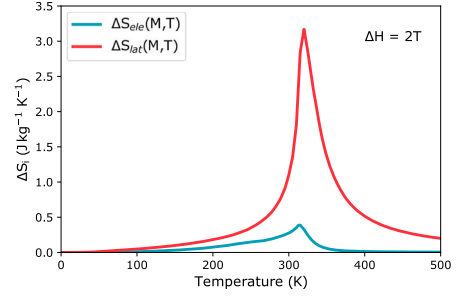


**Figure 3.** Temperature-dependent electronic and lattice contributions for the entropy variation.

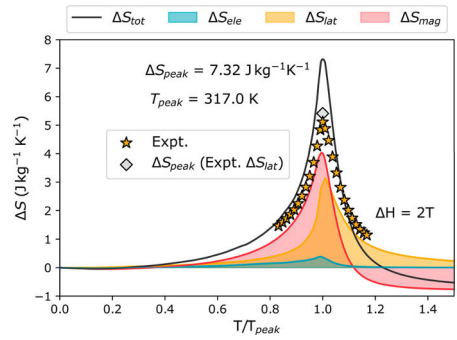


**Figure 4.** Variation of the total entropy change between the PM and FM configuration at a magnetic field change of 2 T. Temperature is normalized according to the entropy peak temperature of the experimental (291 K) and calculated (317 K) data. Experimental data from Ref. [6].

value is 5.2 J/kg/K, at the experimental Curie temperature (292 K) [6].

A surprising result of these calculations is the large lattice contribution, and it is tempting to associate the overestimate of the total entropy change, when comparing to observations, to a theory that results in a too large value of  $\Delta S_{\text{lat}}$ . One can relate this overestimation of  $\Delta S_{\text{lat}}$  to the consequence of calculating the entropy from lattice properties at  $T = 0$  K. In Ref. [28], measurements of the elastic constants for Gd from 0 to 360 K for the cases  $H = 0$  T and  $H = 2.5$  T, allow us to examine the importance of finite temperature effects on the elastic properties of the FM phase, and therefore also to estimate  $\Delta S_{\text{lat}}$ .

Applying the Debye model with the experimental data of elastic constants as input, with and without an applied field and at 300 K [28], we estimate a value of  $\Delta S_{\text{lat}} = 0.986$  J/kg/K, at the Curie temperature (for a more detailed comparison between our values and experimental estimates, see the Supplement). When added to the calculated electronic and magnetic contributions to

the entropy change (gray diamond in Figure 4), we obtain a  $S_{\text{peak}}$  of 5.41 J/kg/K nearly perfect agreement with the observed experimental value. This close agreement highlights the importance of including all the entropy contributions for calculations of the magnetocaloric effect under the risk of underestimating  $\Delta S$  [29] the performance of the material.

Despite some controversy in its calculation and use, the relative cooling power (RCP) is a widely used magnetocaloric materials performance parameter [6]. It can be calculated from the refrigerant capacity ( $q$ ) [30]:

$$q = \int_{T_{\text{cold}}}^{T_{\text{hot}}} \Delta S(T) dT \quad (8)$$

with  $T_{\text{hot}}$  and  $T_{\text{cold}}$  approximated by the temperatures for full width at half maximum of  $\Delta S(T)$  [4,31]. Using this definition on the calculated entropy with experimental elastic constants, we estimate an RCP of approximately 219 J/kg in close agreement with experimental calculations (226.9 J/kg [6]), attesting to the accuracy of the calculated  $\Delta S$  curve.

#### 4. Conclusions

We propose a new scheme for magnetic MC simulations that reproduce the experimental measurements of magnetism of hcp Gd, in a wide temperature range. The success obtained stresses the importance of including quantum and classic fluctuations to describe the magnetic state correctly in temperatures between limits  $T \rightarrow 0$  and  $T \rightarrow T_C$ , and from there an appropriate value of the magnetic entropy change. Furthermore, based on the simulated temperature-dependence of the magnetization we calculate the entropy of the electronic and lattice subsystems. Calculations of all entropy contributions, in the absence and presence of an external magnetic field, allow to estimate the magnetocaloric effect of Gd, with encouraging agreement with experiments.

Note, that first-principles calculations of the  $\Delta S$  contributions are not a trivial task since lifting approximations imply a drastic increase in required computational resources. In addition, it is not always obvious which finite temperature mechanisms are relevant. For example, finite temperature effects could be included in the lattice entropy calculation through the quasi-harmonic approximation. However, other phenomena like phonon-phonon interactions might be needed for an accurate description. Moreover, there are hysteresis losses in experimental measurements, which one cannot account for in a first-principles approach dealing with ideal systems.

Despite methodological and numerical challenges and the need to introduce approximations, the present

work establishes a realistic procedure to calculate from first-principles theory coupled to methods of statistical physics, the entropy variation associated with the magnetocaloric effect. The method is applied to hcp Gd and is demonstrated to accurately reproduce observations.

#### Note

1. At low temperatures, the magnetic fluctuations can only happen in the directions transverse to the magnetization, i.e. the system has 2 degrees of freedom.






#### Disclosure statement

No potential conflict of interest was reported by the author(s).

#### Funding

This work was supported by the Swedish Foundation for Strategic Research, within the project Magnetic Materials for Green Energy Technology (ref. EM16-0039), STandUPP, eSENCE, the Swedish Energy Agency (Energimyndigheten) as well as Vetenskapsrådet. The computations performed in this work were enabled by resources provided by the CSC – IT Center for Science, Finland, for computational resources and by the Swedish National Infrastructure for Computing (SNIC) at NSC and PDC centers, partially funded by the Swedish Research Council through grant agreement no. 2018-05973.

#### ORCID

- R. Martinho Vieira  <https://orcid.org/0000-0003-2778-029X>  
 O. Eriksson  <https://orcid.org/0000-0001-5111-1374>  
 T. Björkman  <https://orcid.org/0000-0002-1154-9846>  
 A. Bergman  <https://orcid.org/0000-0002-5134-1978>  
 H. C. Herper  <https://orcid.org/0000-0001-6159-1244>

#### References

- [1] GV Brown. Magnetic heat pumping near room temperature. *J Appl Phys.* 1976 Aug;47(8):3673–3680. <http://aip.scitation.org/doi/10.1063/1.323176>.
- [2] Pecharsky VK, Gschneidner KA. Giant magnetocaloric effect in Gd<sub>5</sub>(Si<sub>2</sub>Ge<sub>2</sub>). *Phys Rev Lett.* 1997 Jun;78(23):4494–4497. <https://journals.aps.org/prl/abstract/10.1103/PhysRevLett.78.4494>.
- [3] Brück E. Developments in magnetocaloric refrigeration. *J Phys D: Appl Phys.* 2005;38(23):R381. <https://iopscience.iop.org/article/10.1088/0022-3727/38/23/R01/meta>.
- [4] Gschneidner KA, Pecharsky VK. Magnetocaloric materials. *Ann Rev Materials Sci.* 2000 8;30(1):387–429. <http://www.annualreviews.org/doi/10.1146/annurev.mat.sci.30.1.387>.
- [5] Lyubina J. Magnetocaloric materials for energy efficient cooling. *J Phys D: Appl Phys.* 2017 Feb;50(5):053002. <http://stacks.iop.org/0022-3727/50/i=5/a=053002?key=crossref.dfb84d1b7d0ad20592a3a2082e3755f2>.

- [6] Gottschall T, Skokov KP, Fries M, et al. Making a cool choice: the materials library of magnetic refrigeration. *Adv Energy Mater.* 2019 Sep;9(34):1901322. <https://doi.org/10.1002/aenm.201901322>.
- [7] Scheibel F, Gottschall T, Taubel A, et al. Hysteresis design of magnetocaloric materials-from basic mechanisms to applications. *Energy Technol.* 2018 Aug;6(8):1397–1428. <http://doi.wiley.com/10.1002/ente.201800264>.
- [8] Tishin AM, Spichkin YI. *The magnetocaloric effect and its applications*. Bristol: IOP Publishing Ltd; 2003.
- [9] Terwey A, Gruner ME, Keune W, et al. Influence of hydrogenation on the vibrational density of states of magnetocaloric LaFe<sub>1.4</sub>Si<sub>1.6</sub>H<sub>1.6</sub>. *Phys Rev B.* 2020 Feb;101(6):064415. <https://journals.aps.org/prb/abstract/10.1103/PhysRevB.101.064415>.
- [10] Woo CH, Wen H, Semenov AA, et al. Quantum heat bath for spin-lattice dynamics. *Phys. Rev. B.* 2015 Mar;91(10):104306. <https://journals.aps.org/prb/abstract/10.1103/PhysRevB.91.104306>.
- [11] Bergqvist L, Bergman A. Realistic finite temperature simulations of magnetic systems using quantum statistics. *Phys Rev Materials.* 2018 Jan;2(1):013802. <https://link.aps.org/doi/10.1103/PhysRevMaterials.2.013802>.
- [12] Evans RFL, Atxitia U, Chantrell RW. Quantitative simulation of temperature-dependent magnetization dynamics and equilibrium properties of elemental ferromagnets. *Phys Rev B.* 2015;91:144425.
- [13] Sandberg A. Quantum statistics and the magnetocaloric effect. 2020. <http://urn.kb.se/resolve?urn=urn:nbn:se:uu:diva-415830>.
- [14] Kurz P, Bihlmayer G, Blügel S. Magnetism and electronic structure of hcp Gd and the Gd(0001) surface. *J Phys: Condensed Matter.* 2002 Jul;14(25):305. <https://iopscience.iop.org/article/10.1088/0953-8984/14/25/305>.
- [15] Locht IL, Kvashnin YO, Rodrigues DC, et al. Standard model of the rare earths analyzed from the Hubbard *i* approximation. *Phys Rev B.* 2016 Aug;94(8):085137. <https://journals.aps.org/prb/abstract/10.1103/PhysRevB.94.085137>.
- [16] Kresse G, Hafner J. Ab initio molecular-dynamics simulation of the liquid-metal–amorphous-semiconductor transition in germanium. *Phys Rev B.* 1994 May;49(20):14251–14269. <https://link.aps.org/doi/10.1103/PhysRevB.49.14251>.
- [17] Kresse G, Furthmüller J. Efficiency of ab-initio total energy calculations for metals and semiconductors using a plane-wave basis set. *Comput Materials Sci.* 1996 Jul;6(1):15–50. <https://linkinghub.elsevier.com/retrieve/pii/0927025696000080>.
- [18] Kresse G, Furthmüller J. Efficient iterative schemes for ab initio total-energy calculations using a plane-wave basis set. *Phys Rev B.* 1996 Oct;54(16):11169–11186. <https://link.aps.org/doi/10.1103/PhysRevB.54.11169>.
- [19] Blöchl PE. Projector augmented-wave method. *Phys Rev B.* 1994 Dec;50(24):17953–17979. <https://link.aps.org/doi/10.1103/PhysRevB.50.17953>.
- [20] Wills JM, Eriksson O, Andersson P, et al. *Full-potential electronic structure method*. Berlin, Heidelberg: Springer Berlin Heidelberg; 2010. (Springer Series in Solid-State Sciences; vol. 167).
- [21] Togo A, Tanaka I. First principles phonon calculations in materials science. *Scr Mater.* 2015 Nov;108:1–5. <https://www.sciencedirect.com/science/article/pii/S135-9646215003127>.
- [22] Ebert H, Ködderitzsch D, Minár J. Calculating condensed matter properties using the KKR-Green's function method—recent developments and applications. *Rep Progress Phys.* 2011;74(9):096501. <https://iopscience.iop.org/article/10.1088/0034-4885/74/9/096501>.
- [23] Liechtenstein A, Katsnelson M, Antropov V, et al. Local spin density functional approach to the theory of exchange interactions in ferromagnetic metals and alloys. *J Magn Magn Mater.* 1987 5;67(1):65–74. <https://www.sciencedirect.com/science/article/pii/0304-885387907219>.
- [24] UppASD – Department of Physics and Astronomy – Uppsala University, Sweden, 2021. Last accessed 2021-11-10. <https://physics.uu.se/uppasd>.
- [25] Nigh HE, Legvold S, Spedding FH. Magnetization and electrical resistivity of gadolinium single crystals. *Phys Rev.* 1963 Nov;132(3):1092–1097. <https://journals.aps.org/pr/abstract/10.1103/PhysRev.132.1092>.
- [26] Vieira RM, Eriksson O, Bergman A, et al. High-throughput compatible approach for entropy estimation in magnetocaloric materials: FeRh as a test case. *J Alloys Compd.* 2021 Mar;857:157811. <https://linkinghub.elsevier.com/retrieve/pii/S092583882034175X>.
- [27] Seyf HR, Yates L, Bougher TL, et al. Rethinking phonons: the issue of disorder. *npj Comput Materials.* 2017 Nov;3(1):1–8. <https://www.nature.com/articles/s41524-017-0052-9>.
- [28] Palmer SB, Lee EW, Islam MN. The elastic constants of gadolinium, terbium and erbium. *Proc R Soc London Ser A, Math Phys Sci.* 1974 Oct;338(1614):341–357. <http://www.jstor.org/stable/78445>.
- [29] Essajai R, Ennassiri N, Balli M, et al. Revisiting the magnetic and magnetocaloric properties of bulk gadolinium: a combined DFT and Monte Carlo simulations. *Phys Scripta.* 2020 Nov;96(1):015808. <https://iopscience.iop.org/article/10.1088/1402-4896/abc984>.
- [30] Gschneidner A, Pecharsky VK, Tsokol AO, et al. Recent developments in magnetocaloric materials. *Rep Progress Phys.* 2005 6;68(6):1479–1539. <https://iopscience.iop.org/article/10.1088/0034-4885/68/6/R04>.
- [31] Erchidi Elyacoubi AS, Masrouf R, Jabar A. Surface effects on the magnetocaloric properties of perovskites ferromagnetic thin films: a Monte Carlo study. *Appl Surf Sci.* 2018 Nov;459:537–543.

## SUPPLEMENTAL MATERIAL

### Realistic first-principles calculations of the magnetocaloric effect; applications to hcp Gd

R. Martinho Vieira<sup>a,b,\*</sup>, O. Eriksson<sup>a,c</sup>, T. Björkman<sup>b</sup>, A. Bergman<sup>a</sup>, H. C. Herper<sup>a</sup>

<sup>a</sup>Department of Physics and Astronomy, Uppsala University, Box 516, SE-75120 Uppsala, Sweden

<sup>b</sup>Physics, Faculty of Science and Engineering, Åbo Akademi University, FI-20500 Turku, Finland

<sup>c</sup>School of Science and Technology, Örebro University, SE-701 82 Örebro, Sweden

#### 1. Computational details

We performed structural relaxation for the PM and FM phases with VASP, using the hcp Gd conventional cell and an energy cutoff of 450 eV, and using supercells of  $2 \times 2 \times 2$  of the respective relaxed cells for the phonon calculations performed within the finite displacements approach. The calculations made use of GGA based (PBE, [1]) PAW potentials.

In these studies, the FM phase was described with  $f$ -electrons in the valence treated with Hubbard correction with  $U_{eff}=6$  eV ( $U=6.7$  and  $J=0.7$  eV), while for the PM phase we used the setup of non-spin-polarized  $f$ -core-states.

For this set of calculations, the Brillouin zone was sampled using a  $\Gamma$ -centered  $k$ -mesh  $48 \times 48 \times 24$  for the unit cell, and an accordingly smaller  $k$ -mesh  $24 \times 24 \times 12$  for the supercell.

The Heisenberg exchange parameters of the FM phase were computed in LDA (with Perdew-Wang parametrization [2]) calculations with RSPt using the Lichtenstein method [3] implemented in RSPt as described in Ref. [4]. In this set of calculations, we treated the  $f$ -electrons as spin-polarized core states, with a  $20 \times 20 \times 11$   $k$ -mesh. The resulting  $T_C$  in MC simulations using this spin-Hamiltonian, is  $\sim 315$  K in close agreement with the experimental value of 290 K (and previous calculations).

Electronic structure calculations were also performed in SPR-KKR within the LDA+U approach (with the von Barth - Hedin parametrization [5]) using a consistent  $U$  and  $J$  parameters with the VASP setup. SPK-KKR allows to describe the magnetic disorder using the DLM approach within the Coherent Potential Approximation [6,7], which enables a more realistic description of the PM phase to compare with the approximations used in previous setups (see Supplement) and also allowing for calculation of the electronic properties for different levels of magnetic disorder.

To compute the density of states within the disordered local moments approach, we used SPR-KKR code and performed using LDA+U with the same  $U$  and  $J$  parameters mentioned above and a mesh with 1500  $k$ -points.

The MC calculations were performed using the UppASD software, using the Metropolis method to sample the phase space. For each temperature step, 160000 MC steps were performed, with the initial 10000 steps being reserved for achieving

---

\* Corresponding Author. Email: rafael.vieira@physics.uu.se

thermalization of the magnetic configuration and therefore they were not included in the measurement of the thermodynamic quantities. For these computations, a simulation box with 36 repetitions of the unit cells along all lattice vectors, was considered with periodic conditions at the boundaries.

Following the results of benchmarking tests [8], we calculated the magnetic heat capacity ( $C_{mag}$ ) from the internal energy determined in the MC simulations according to the thermodynamic relation:

$$C_{mag} = \frac{\partial U_{mag}}{\partial T} = \frac{\partial \langle E_{mag} \rangle}{\partial T}, \quad (1)$$

where  $E_{mag}$  is the total energy of the atoms in the simulation cell.

The RSPt calculations for the Heisenberg exchange parameters we performed with the  $f$ -electrons as spin-polarized core states, on a  $20 \times 20 \times 11$  k-mesh. The resulting  $T_C$  in MC simulations using this spin-Hamiltonian, is  $\sim 315$  K in close agreement with the experimental value of 290 K (and previous calculations [9]).

## 2. DOS

In Figure 1, the computed Density of States (DOS) for the PM phase of Gd is compared for the considered setups: non-spin-polarized core  $f$ -states and disordered local moments within the Coherent Potential Approximation. The calculations were performed in RSPt and SPR-KKR, respectively, with the LDA parametrizations mentioned earlier, being for SPR-KKR being necessary of a Hubbard correction (LDA+U) on the  $f$  states.

We can see both approaches produce a reasonably similar DOS with the same features, justifying the use of the non-spin-polarized core  $f$ -states setup for describing the PM phase.

An interesting feature of the presented DOS would be the peak of  $p$ -states around the Fermi energy that seem to follow a higher peak of  $d$ -states, suggesting a hybridization of these orbitals.

## 3. Phonons and Elastic properties

The calculated phonon dispersions for both PM and FM phases is presented in Figure 2, alongside experimental results for Tb [10] and Gd [11] at room temperature. In general, the phonon dispersion displayed the same feature in both magnetic phases, with the FM showing modes with higher energy, and for lower energy modes (2.5 j THz), there is a good agreement between first-principles calculations and measurements. In contrast, there is a disagreement between calculations and measurement for optical modes of higher energies, particularly in the  $\Gamma$ - $M$  and  $\Gamma$ - $A$  directions of the Brillouin zone. However, the agreements generally seem reasonable and capable of reliable estimation of the lattice entropy contribution.

Unfortunately, the surprising lack of data in the literature about the phonon dispersion for Gd makes it challenging to understand the reason for the mentioned disagreements. Furthermore, experimentally, it seems challenging to investigate Gd phonon properties since the material has a substantial neutron absorption cross-section, preventing an efficient application of inelastic neutron scattering method [12]. Conse-

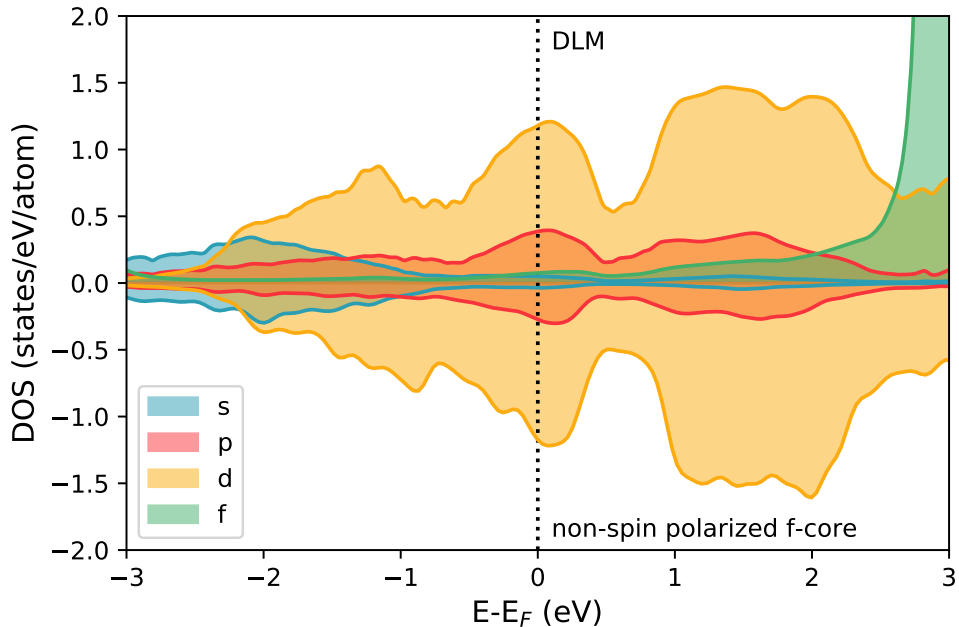


**Figure 1.** Orbital-projected DOS for the paramagnetic phase of Gd, according with different descriptions.

quently, previous studies of Gd phonon dispersion were based on the results of the neighbouring Tb, which also crystallizes in a hexagonal closed packed structure.

There are measurements of the elastic constant on a wide range of temperatures (0-360K) with and without application of a magnetic field (2.5T) which allow us to compare the experimental bulk modulus and lattice entropy (via Debye Model) with our first-principles predictions. To do so, we consider two sets of elastic constants while comparing the magnetic phases.

To do so, we consider two sets of elastic constants while comparing the magnetic phases that differ on the FM phase description, while for the PM phase, we keep the elastic constants at 300K ( $< T_C$ ) without an applied field. Firstly, we considered the elastic constants at  $T=0K$  (without magnetic field) to exclude finite temperatures effects, which is conceptually closer to our calculations. Then, to include temperature effects, we considered the elastic constants at 300K under a magnetic field, which should stabilize the ordered phase.

By comparing the  $\Delta S_{lat}$  estimated from these two sets, it becomes evident that finite temperature effects play a significant role in Gd structural properties, see Figure 3. While the case with the elastic constants of the FM phase at  $T=0K$  is quite close to our first-principles calculations supporting our calculations, including finite temperature effects, we obtain a significantly smaller and more reasonable estimation of the lattice entropy.

The experimental bulk modulus illustrates how significantly the elastic properties of the FM phase change with temperature, compared with variation between magnetic phases, see Table 1. Neglecting such thermal effects results in the overestimation of the lattice entropy we present in the main work.

Comparing the bulk modulus computed from the experimental data with the ones

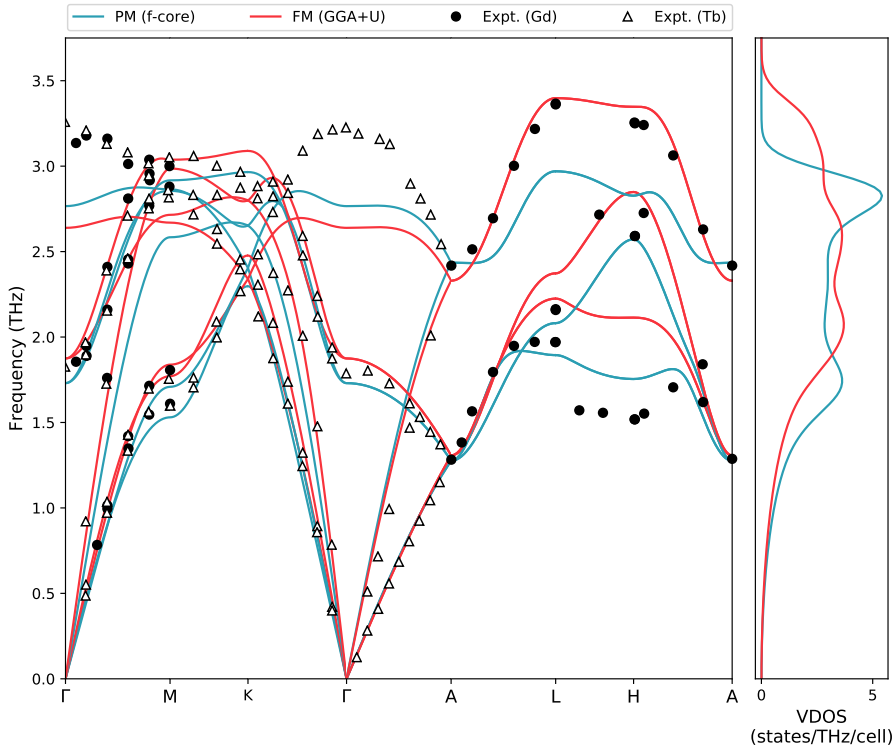


**Figure 2.** Phonon dispersion (left) and vibrational density of states (right) for the FM and PM phase of hcp Gd. Comparison with experimental data extracted from Refs.[10,11].

from first-principles, calculated from fitting the Murnaghan equation of state to energy-volume data, we find a good agreement. Although the correct relation between FM and PM phase is not captured, this difference is too small to be caught by the approach taken, which is efficient in estimating the order of magnitude.

#### 4. Electronic entropy

As shown in Figure 4 (bottom panel), calculation of  $\Delta S_{\text{lat}}$  from the raw gives rise to strange peaks close to the Curie temperature. Not existing any physical reason for their existence, we suspected that they had a numerical origin. By performing tests in our data, we identified the primary source as the linear interpolation for the density of states at the Fermi level ( $\text{DOS}(\epsilon_F)$ ) in function of the magnetization. Although the original data does not show any prominent features (see Figure 4, upper panel), any existing roughness is amplified by the fast drop of the magnetization as  $T \rightarrow T_C$  giving rise to the mentioned peaks.

Note that a slight roughness on our interpolated  $\text{DOS}(\epsilon_F)$  is not reflective of the quality of the calculations or even unexpected. We diligently calculated  $\text{DOS}(\epsilon_F)$  for a dense series of magnetization values and obtained a clear trend with the magnetization, but by working with so close DLM states, we approach the limit of CPA efficiency, and minor deviations of the trend are obtained.

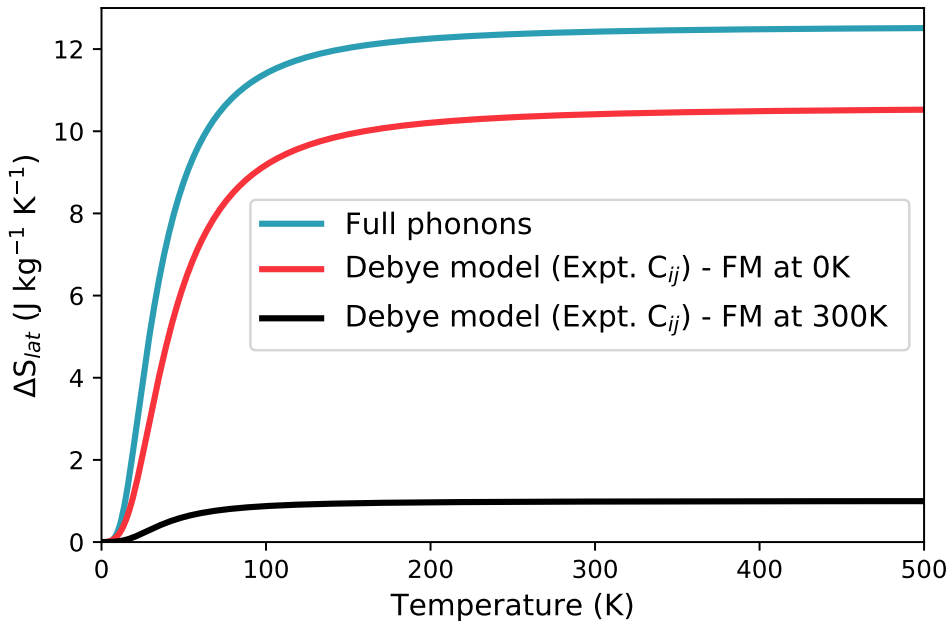


**Figure 3.** Lattice entropy variation  $\Delta S_{\text{lat}} = S_{\text{lat,PM}} - S_{\text{lat,FM}}$  from full phonon calculations and Debye model results from experimental elastic constants. Experimental data from Ref.[13].

Bulk modulus (GPa)				
Phase	Expt. [13]			Calculated
	$T=0K, H=0T$	$T=300K, H=2.5T$	$T=300K, H=0T$	
FM	41.261	37.899	-	36.897
PM	-	-	37.882	37.855

**Table 1.** Comparison of elastic bulk modulus in different experimental conditions and first-principles calculations.

To solve this issue without affecting the accuracy of the calculations, we applied a Savgol filter to the original data points and performed a cubic spline to obtain a smoother interpolation. Such treatment results in a smoother curve with vestigial deviations to the raw data, as shown in Figure 4 (upper panel).

Despite the minimal effect of this treatment on the data, the resultant electronic entropy is significantly improved, see Figure 4 (bottom panel), which supports our assumption of nature numerical for deviations initially calculated.



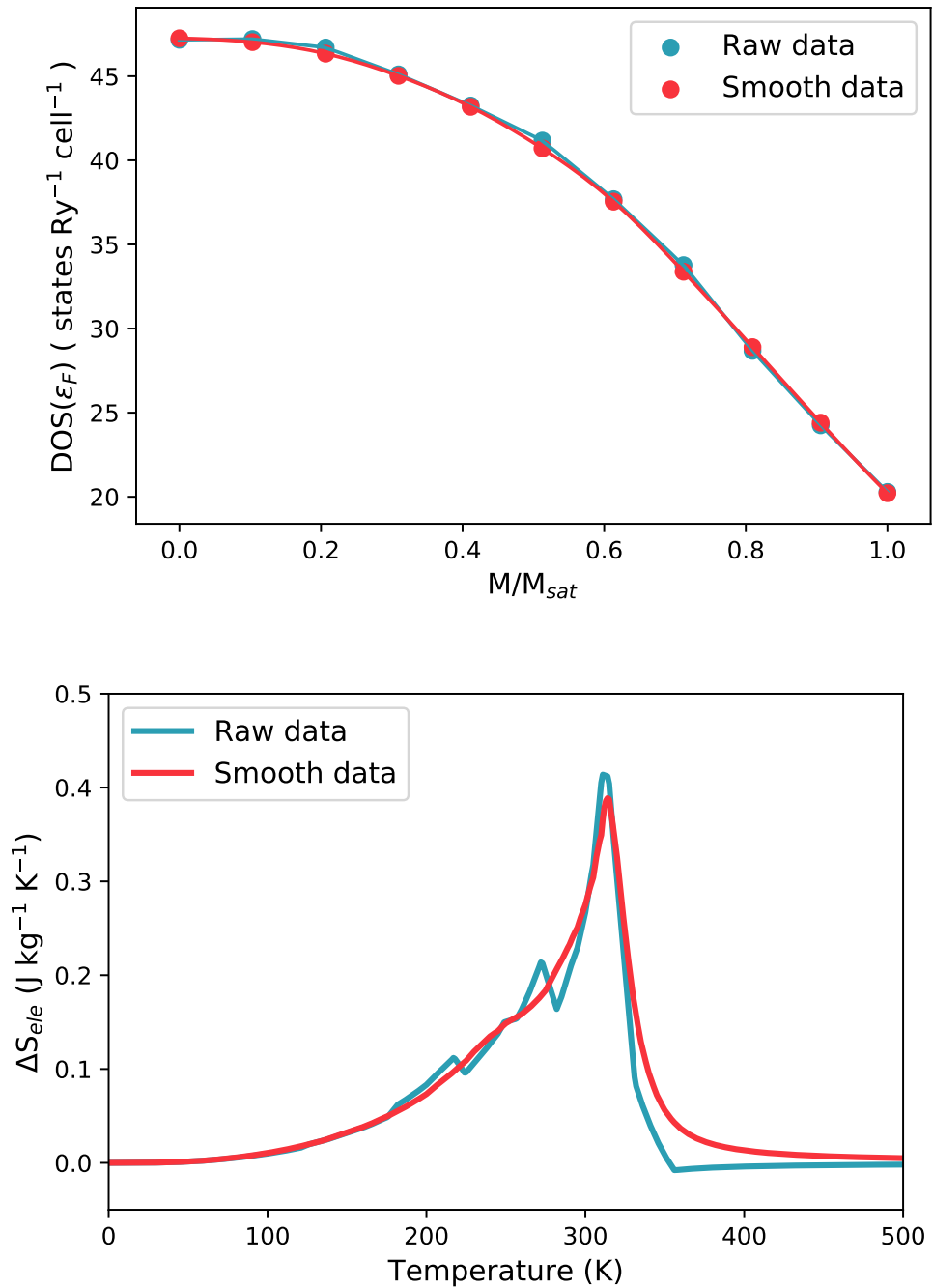


**Figure 4.** Comparison of the variation of the density of states at Fermi level for different magnetisation states (top) and temperature-dependent electronic entropy variation (bottom) for the original and treated data.

## References

- [1] J. P. Perdew, K. Burke, and M. Ernzerhof, “Generalized gradient approximation made simple,” *Physical Review Letters*, vol. 77, no. 18, pp. 3865–3868, 1996.

- [2] J. P. Perdew and Y. Wang, “Accurate and simple analytic representation of the electron-gas correlation energy,” *Physical Review B*, vol. 45, p. 13244, 6 1992.
- [3] A. Liechtenstein, M. Katsnelson, V. Antropov, and V. Gubanov, “Local spin density functional approach to the theory of exchange interactions in ferromagnetic metals and alloys,” *Journal of Magnetism and Magnetic Materials*, vol. 67, pp. 65–74, 5 1987.
- [4] Y. O. Kvashnin, R. Cardias, A. Szilva, I. Di Marco, M. I. Katsnelson, A. I. Lichtenstein, L. Nordström, A. B. Klautau, and O. Eriksson, “Microscopic origin of Heisenberg and non-Heisenberg exchange interactions in ferromagnetic bcc Fe,” *Physical Review Letters*, vol. 116, p. 217202, 10 2015.
- [5] U. v. Barth and L. Hedin, “A local exchange-correlation potential for the spin polarized case. i,” *Journal of Physics C: Solid State Physics*, vol. 5, p. 1629, 7 1972.
- [6] D. W. Taylor, “Vibrational Properties of Imperfect Crystals with Large Defect Concentrations,” *Physical Review*, vol. 156, p. 1017, 4 1967.
- [7] P. Soven, “Coherent-Potential Model of Substitutional Disordered Alloys,” *Physical Review*, vol. 156, p. 809, 4 1967.
- [8] J. Bylin, “Best practice of extracting magnetocaloric properties in magnetic simulations,” 2019.
- [9] I. L. Locht, Y. O. Kvashnin, D. C. Rodrigues, M. Pereiro, A. Bergman, L. Bergqvist, A. I. Lichtenstein, M. I. Katsnelson, A. Delin, A. B. Klautau, B. Johansson, I. Di Marco, and O. Eriksson, “Standard model of the rare earths analyzed from the Hubbard  $i$  approximation,” *Physical Review B*, vol. 94, p. 085137, 8 2016.
- [10] J. C. G. Houmann and R. M. Nicklow, “Lattice Dynamics of Terbium,” *Physical Review B*, vol. 1, p. 3943, 5 1970.
- [11] K. Schmalzl, D. Strauch, and M. Malorny, “Phonon dispersion in Lanthanides: Gd (and Sm, Eu, Dy),” tech. rep., 2006.
- [12] K. Schmalzl, J. Serrano, and D. Strauch, “Phonon Dispersion in Gd,” in *12th International Conference on Phonon Scattering in Condensed Matter*, (Paris), 2007.
- [13] S. B. Palmer, E. W. Lee, and M. N. Islam, “The Elastic Constants of Gadolinium, Terbium and Erbium,” *Proceedings of the Royal Society of London. Series A, Mathematical and Physical Sciences*, vol. 338, pp. 341–357, 10 1974.



ISBN 978-952-12-4377-6